The Design of Low-frequency, Low-g Piezoelectric Micro Energy Harvesters

by

Ruize Xu

Bachelor of Engineering, Mechanical and Automation Engineering
The Chinese University of Hong Kong (2010)

Submitted to the Department of Mechanical Engineering
in partial fulfillment of the requirements for the degree of
Master of Science in Mechanical Engineering
at the Massachusetts Institute of Technology
June 2012

Author _____
Department of Mechanical Engineering
May 11, 2012

Certified by _____
Sang-Gook Kim
Associate Professor of Mechanical Engineering
Thesis Supervisor

Accepted by _____
David E. Hardt
Chairman, Department Committee on Graduate Theses

The Design of Low-frequency, Low-g Piezoelectric Micro Energy Harvesters

by

Ruize Xu

Submitted to the Department of Mechanical Engineering
on May 11, 2012, in partial fulfillment of the
requirements for the degree of
Master of Science in Mechanical Engineering

Abstract

A low-frequency, low-g piezoelectric MEMS energy harvester has been designed. Theoretically, this new generation energy harvester will generate electric power from ambient vibrations in the frequency range of 200~300Hz at excitation amplitude of 0.5g. Our previous energy harvester successfully resolved the gain-bandwidth dilemma and increased the bandwidth two orders of magnitude. By utilizing a doubly clamed beam resonator, the stretching strain triggered at large deflection stiffens the beam and transforms the dynamics to nonlinear regime, and increases the bandwidth. However, the high resonance frequency (1.3kHz) and the high-g acceleration requirement (4~5g) shown in the testing experiments limited the applications of this technology. To improve the performance of the current energy harvesters by lowering the operating frequency and excitation level, different designs have been generated and investigated. Moreover, a design framework has been formulated to improve the design in a systematic way with higher accuracy. Based on this design framework, parameter optimization has been carried out, and a quantitative design with enhanced performance has been proposed. Preliminary work on fabrication and testing setup has been done to prepare for the future experimental verification of the new design.

Thesis Supervisor: Sang-Gook Kim
Title: Associate Professor of Mechanical Engineering

Acknowledgements

I would like to express my deep gratitude to Professor Sang-Gook Kim, my research supervisor, for his guidance, support, encouragement and useful critiques of this research work. He showed me the true meaning of engineering, reminded me of the big picture when I got lost in a detailed problem, gave me encouragement with tremendous patience when fabrication stuck, and shared with me his great insights on research, career and life. All of these will enormously benefit my future work and life, and I thank him very much.

My grateful thanks also go to Dr. Arman Hajati, my predecessor on this energy-harvesting project. Although we have not met each other, I am familiar with his excellent work, based on which, my research becomes possible. His useful advices and critiques through emails also helped me markedly.

I would like to thank my group mates Stephen Bathurst and Heonju Lee for their generous help. They introduced me the available facilities when I was new to the group, helped me on fabrication processing, especially the PZT deposition, discussed with me on my research and gave insightful advices, and answered any questions I had.

I would like to thank You C. Yoon (Richard), a UROP student in our group from 2011 to 2012 for his great contribution to the setup of testing devices, and Dr. Firas Sammoura, with whom I investigated the multiple coupled beam design.

I would like to extend my thanks to MTL staffs for their help on fabrication processing. I especially want to thank Dennis Ward, Bob Bicchieri, Paul Tierney, Bernard Alamariu, Dave Terry and Vicky Diadiuk. My special thanks go to Ray Hardin for his help and administrative support.

Finally, I wish to thank my parents for their love, sacrifices, support and encouragement.

Table of Contents

List of Figures

List of Tables

Chapter 1 Introduction

Harvesting energy from ambient environment in macro scale is common in the world. Solar cells, wind turbines, watermills, to name a few, play important roles in power supply. These technologies generate considerable amount of power at large scale, and are believed to be the solution of the environment issues such as pollution and global warming caused by the consumption of fossil fuel. In contrast, energy harvesting at micro scale generates power in microwatts to miliwatts, and it aims to address other problems.

The fast development of microelectronics stimulates the growth of portable and wireless devices. But their typical power source – battery has its limitations. Its limited lifespan necessitates periodic replacement, which can be expensive and even impossible. In case of wireless sensor network that is distributed in a large terrain, or monitoring sensors embedded in large civil structures or human bodies, the accessibility is extremely constrained. To extend the lifespan of these devices at low cost, an energy harvester, which perpetually generates energy, is a solution. Recent advances in microelectronics bring the power consumption down to very low level, which narrower the gap between the required power of the electronic devices and the power supply from micro energy harvesters. Micro energy harvesting becomes not only feasible but also desirable.

A number of ambient energy sources exist, such as vibration, waste heat, fluid flow, solar energy etc. Each of them has its unique characteristics and applications. For example, for vibrating embedded system, vibration energy harvesters may be preferred to solar cell since there is no sunlight but kinetic energy. For vibration energy harvesting, there are three main transduction mechanisms: electrostatic, electromagnetic and piezoelectric. Piezoelectric energy harvesting has received much attention due to its ability to directly convert strain energy into electric energy and the ease to be integrated into MEMS-scale systems. Our research focuses on piezoelectric vibration energy harvesting.

1.1 Thesis Objective and Contribution

A design framework of nonlinear resonance based piezoelectric energy harvesters has been devised and presented. The concept of utilizing stretching strain in a beam structure to attain nonlinear resonance and significantly increase the energy harvesting bandwidth was well proved by our previous work up to 2010. To further improve the performance of the energy harvesters to meet the requirements of real applications, a more systematic and deliberate design process is necessary. Therefore, a new design framework has been formulated with considerations of physical constraints and design parameter optimization.

Moreover, a new quantitative design based on our previously developed energy harvester has been proposed. This design was created by following the newly developed design framework, which guaranteed an optimal solution with the available materials and facilities, and physical constraints, within the design space. Simulations have been made to demonstrate the superiorities of the proposed design, including wide bandwidth, low operating frequencies and low-g excitations.

To verify the performance of the improved design, fabrication of the prototype is necessary in future research. Preliminary work on fabrication for the preparation has been done. An electromechanical testing setup has also been built up for future testing.

1.2 Thesis Organization

The thesis presented our recent progress on the piezoelectric energy harvesting research. A thorough review on the discrepancy between real applications and present energy harvesters, design considerations, modeling and theoretical analysis, and related experimental preparations has been made. The first chapter overviews energy harvesting, and introduces the objective and the organization of the thesis. Chapter 2 reviews the

basic theories behind energy harvesting, state of the art of this field and our previous work. Chapter 3 discusses the criteria for the design of piezoelectric vibration energy harvesters, defines the design goals, reviews the design ideas that have been investigated, formulates a design scheme and proposes a quantitative design following that scheme. Preliminary work on fabrication and testing are reported in Chapter 4 and Chapter 5 respectively. A summary of the thesis and future work are concluded in the last chapter.

Chapter 2 Background

Piezoelectric vibration energy harvesting is the intersection of vibration energy harvesting and piezoelectric energy harvesting. A review of both research areas may not only provide a clue on the superiorities of this unique energy harvesting method but also reveals novel ideas that may inspire new designs. A variety of peers' recent work are presented and compared in this comprehensive review to show the state of the art of this research field, the trend of the research development and where we are standing. Along with a brief review of our group's previous work from 2005, a much clearer view can be obtained.

2.1 Vibration Energy Harvesting

Vibration as a common ambient energy source can be found in household appliances (refrigerators, microwave ovens, washing machines etc.), large civil structures (buildings, bridges etc.), industrial plant, automobiles and many others. Kinetic energy in the vibrations can be converted into electrical energy via three main transduction mechanisms: electrostatic, electromagnetic and piezoelectric. The available kinetic energy depends on the frequency spectrum and the excitation level.

The general model of a vibration energy harvester is a typical mass-spring-damper system as shown in Fig. 2-1. The difference of the transduction mechanisms lies in the damping characteristic. Assume the inertial frame is excited by an external sinusoidal vibration of the form $z(t) = Z\sin(\omega t)$. Then the dynamic equation of the system is,

$$m\ddot{x}(t) + b\dot{x}(t) + kx(t) = -m\ddot{z}(t) \qquad \text{Eq. 2.1}$$

where m is the proof mass, b is the damping coefficient, k is the spring stiffness and t is the time. The damping coefficient include both the mechanical loss b_m and electrical damping b_e. The steady state solution of Eq. 2.1 can then be found,

$$x(t) = \frac{\omega^2}{\sqrt{\left(\omega_n^2 - \omega^2\right)^2 + \left(\frac{b\omega}{m}\right)^2}} Z\sin(\omega t - \phi) \qquad \text{Eq. 2.2}$$

where ϕ is the phase angle, expressed as

$$\phi = \tan^{-1}\left(\frac{b\omega}{k - \omega^2 m}\right). \qquad \text{Eq. 2.3}$$

The power dissipated in the damper is [1],

$$P = \frac{m\zeta Z^2 \left(\frac{\omega}{\omega_n}\right)^3 \omega^3}{\left[1 - \left(\frac{\omega}{\omega_n}\right)^2\right]^2 + \left[2\zeta\left(\frac{\omega}{\omega_n}\right)\right]^2} \qquad \text{Eq. 2.4}$$

Expressing Eq. 2.4 in terms of mechanical damping, electrical damping and excitation amplitude,

$$P = \frac{\zeta_e}{4\omega_n\left(\zeta_e + \zeta_m\right)^2} mA^2 \qquad \text{Eq. 2.5}$$

Several conclusions can be drawn from the observation of Eq. 2.5. The output power is inversely proportional to resonance frequency; therefore the energy harvester should be designed at lowest possible frequency to achieve highest power. The output power is also proportional to the excitation amplitude squared, which limits the energy available for

conversion with low-g vibrations whatever the specific design is. It can also be seen that power is proportional to the proof mass, so a large proof mass is always desirable for energy harvesting. Finally, the term composed of the mechanical and electrical damping ratios implies that the maximum power is achieved when the electrical damping matches the mechanical damping. This is actually a limiting factor for all linear resonator based energy harvesters. Nonlinear resonator based energy harvester does not have this limit and is able to generate more power, which will be analyzed at the end of this chapter.

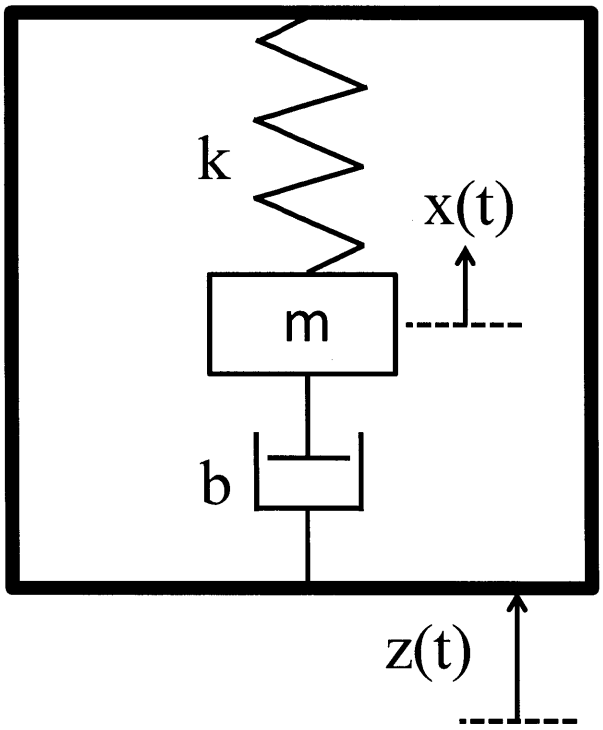

Figure 2-1 Mechanical lumped model of linear resonator based energy harvester.

Three energy transduction mechanisms are used for vibration energy harvesting: electrostatic, electromagnetic and piezoelectric. Electrostatic generators have the basic structure as a capacitor. Based on different modes, the charge on the capacitor or the voltage across the capacitor remains constant. The energy for transduction comes from the work done against the electrostatic force. It is easy to integrate electrostatic harvesters into microsystems, but input charge is needed for operation.

Electromagnetic generators generate electricity from the relative motion of a magnet to a coil. They do not require a voltage source to operate, but the output voltage is relatively low [2], it drops as the size of the generator decreases [3], and it reduced significantly at micro scale [4]. Moreover, it is still a challenge to implement the assembly of magnets in MEMS scale.

Piezoelectric materials produce charge when subjected to mechanical strain. The piezoelectric generators produce high voltages and low currents, and require no voltage source to operate. Some believe they are more difficult to integrate into microsystems [2], but [5, 6] showed successful implementation of MEMS scale piezoelectric energy harvesters.

2.2 Piezoelectric Energy Harvesting

Piezoelectric energy harvesters can be categorized by their power sources, such as ambient vibrations, impact induced, fluid driven and human powered. Regardless of the power sources, the basic working principle is the same – the environment applies a stress on piezoelectric material so that the mechanical energy in the environment is converted to electrical energy. Before introducing the various harvesting methods, the fundamentals of piezoelectricity are reviewed.

2.2.1 Fundamentals of Piezoelectricity

Piezoelectricity is the outcome of the lack of center of inversion symmetry in atomic structure [7]. Due to this asymmetry, an electric polarization is created in response to a mechanical stress, which changes the charge symmetry and forms electric dipoles in atomic level. The reverse effect, a mechanical strain is induced by an external electric field also exists. The first effect is typically used for sensing, and the latter is used for actuation. A piece of piezoelectric material can be connected to loads and form a loop.

Being subjected to alternating mechanical strains, the varying induced charge will form current and power the load, and this becomes a power generator.

Piezoelectric effect couples mechanical and electrical domains. Mathematically, it connects mechanical stress, which is a second-order tensor, to electrical polarization, which is a first-order tensor, so a third-order tensor is needed. With symmetry, this tensor can be reduced. The mechanical and electrical coupling of linear piezoelectricity can be described by the piezoelectric constitutive equations [8]:

$$S_{ij} = s^{E}_{ijkl} T_{kl} + d_{kij} E_k \qquad \text{Eq. 2.6}$$

$$D_i = d_{ikl} T_{kl} + \varepsilon^{T}_{ik} E_k \qquad \text{Eq. 2.7}$$

where S_{ij} is the strain component, T_{kl} is the stress component, E_k is the electric field component, D_i is the electric displacement component, s^{E}_{ijkl}, d_{kij} and ε^{T}_{ik} are the elastic, piezoelectric, and dielectric constants respectively. The subscripts *i, j, k, l* run over integers 1, 2, 3. The superscripts *E* and *T* means at constant electric field and at constant stress respectively.

Different piezoelectric materials used in micro-fabrication include quarts, zinc oxide, aluminum nitride, lead zirconate-titanate (PZT), $Pb(Mg_{1/3}Nb_{2/3})O_3$-$PbTiO_3$ (PMN-PT) and polymer piezoelectrics such as poly-vinylidene fluoride (PVDF). PZT is employed for our energy harvesters in that it has high piezoelectric coefficients and thus will have high output voltage and power. Sol-gel spin coating is used for depositing thin film PZT, which will be explained in more detail in fabrication chapter.

2.2.2 Piezoelectric Energy Harvesters Based on Different Energy Sources

Vibration Energy Harvesters

Vibration energy harvesters convert kinetic energy of vibrations into electrical energy through piezoelectricity. A typical design is based on a cantilever beam resonator as shown in Figure 2-2. The beam with a proof mass is bonded on a base which is vibrating, so the kinetic energy of the proof mass transfer to the strain energy of the beam in each cycle, and the strained piezoelectric material induces electricity which can power the loads or be stored.

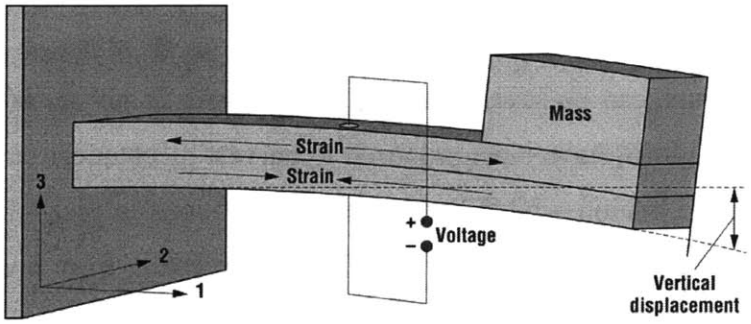

Figure 2-2 Schematic of a common cantilever based piezoelectric energy harvester [9].

Impact Energy Generators

Impact energy generators ([10-12]) convert mechanical energy which comes from high impact force to electricity through piezoelectric materials. In [10], 30-mm projectiles are launched with a high pressure helium gun to velocities of approximately 300 m/s, and 25 kW output pulse in the order of 1 μs is generated. Another impact generator (11, 12]) consists of a cantilever, which vibrates between two bimorphs (Figure 2-3) and causes deflections on the side bimorphs, so that piezoelectric layers in the bimorphs convert mechanical energy into electricity. The impact based energy generators are in relatively large size, and the applications remain unclear [13].

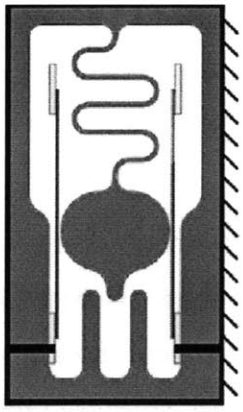

Figure 2-3 Schematic of a vibro-impacting power harvester [12].

Fluid Driven Generators

Piezoelectric materials can be stressed and generate power in air or water flow as well. Windmill designs [14-16] have been proposed to harvest mechanical energy of wind. In water, wakes formed behind a bluff body induce oscillations in piezoelectric structures, which then become power sources [17, 18]. Energy harvesting from unsteady, turbulent fluid flow using piezoelectric generators has been investigated in [19]. Figure 2-4 shows a cantilever bimorph in harvesting energy from flowing water [20]. [21] demonstrates "microwind" power generation using flow-induced self-excited oscillations of a piezoelectric beam embedded within a cavity. These structures are aimed to convert mechanical energy available in oceans and rivers to electrical energy in milli-watt and even watt power ranges [13].

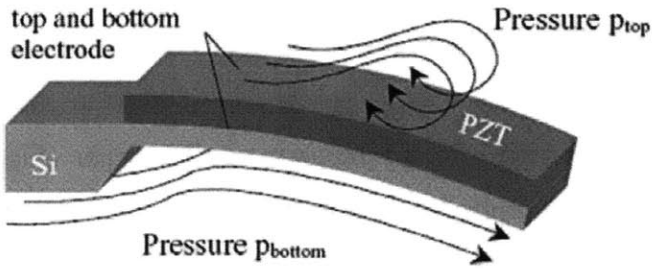

Figure 2-4 A cantilever bimorph in harvesting energy from flowing water [20].

Human Powered Generators

Human powered generators include Implantable energy generators and wearable power generators. Effort has been made to implant piezoelectric energy harvester into human bodies to power embedded systems such as sensors and other biomedical devices. One prototype powering orthopedic knee implants is demonstrated in [22]. Energy harvesting from human motion was also studied in [23, 24]. Gonz´alez et al. [25] presents an overview of various sources of mechanical energy available in human body. Shoe inserts also attracted a lot of interests, related research can be found in [26, 27]. [28] proposed a wearable piezoelectric shell structures which harvest energy from human motions at joints and elbow (Figure 2-5).

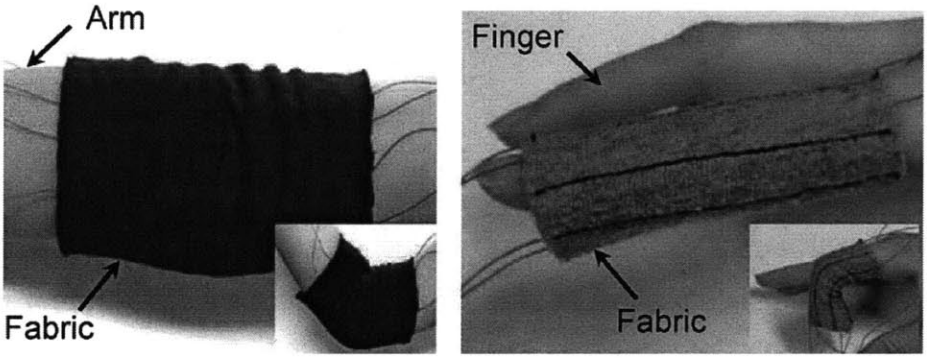

Figure 2-5 Photograph of fabrics worn on the elbow joint and the finger [28].

2.2.3 Recent Advances in Vibration Energy Harvesting

Increase Efficiency

Material Selection and Parameter Optimization

Piezoelectric ceramic is normally brittle, which limits the strain and the stored strain energy in it. Flexible piezoelectric materials thus have been developed and tested for power harvesting [29-32]. Larger strains provide more mechanical energy available for conversion into electrical energy. Utilizing a more efficient coupling mode such as d_{33}

also leads to higher output voltage and power [6, 33]. Parameters such as electrode size, properties of beams etc. have also been investigated [34, 35].

Circuitry

In addition to improving power harvesting efficiency and energy generation capabilities by redesigning the device, enhancing the power harvesting circuitry is also a means for improvement. More effective circuits [36-38] have been studied. New circuits such as the so-called 'synchronous switch harvesting on inductor' (SSHI) were proved theoretically and experimentally more efficient than conventional circuits [39, 40], and it was proved that SSHI circuit would significantly enhance the performance of nonlinear resonator based energy harvesters as well [5].

Wider Bandwidth

Tuning

The natural frequency of the resonator can be tuned by changing the axial tension of a beam through manipulating magnets [41, 42]. Beam dimensions [43], proof mass [44] have also been tuned mechanically to widen the bandwidth. However, frequency tuning inevitably consumes power, the tuning efficiency is low and the tuning range is limited [45].

Multiple Beams

Shahruz [46, 47] designed an energy harvesting device capable of resonating at various frequencies without adjustment. The device consists of multiple cantilever beams with various lengths and end masses. The combination of the cantilevers, which have different resonant frequencies, created a so-called 'mechanical bandpass filter.' By selecting the length and end mass of each beam, the device had a wide band of resonant frequencies. But this method increases both the size and the cost, a more complex electric circuit may be necessary, and the overall efficiency is reduced.

Nonlinear Resonance

In contrast to a linear resonator, which typically has a narrow bandwidth, nonlinear resonator changes the dynamic response and greatly increases the bandwidth. Nonlinearity may come from magnetic force and special mechanical structures.

Magnetic force has been introduced in linear resonators to provide nonlinear restoring force. The design in [48] had a center magnet placed between two magnets with the poles oriented to repel the center magnet — thus suspending the center magnet with a nonlinear restoring magnetic force (Fig. 2-6 (a)). Another possible design is to fix magnets at the tip of a cantilever (Fig. 2-6 (b)) to achieve *Duffing* mode resonance [49]. The magnetic forces between the magnets and the iron create a nonlinear spring, whose nonlinearity is determined by the strength of the magnets and the size of the air gap between the magnets and the iron stator. The energy harvesters in [48] and [49] are electromagnetic – the change of magnetic flux in the coils induce electricity. [50] showed a bi-stable *Duffing* oscillator based piezoelectric energy harvester. The device consists of a ferromagnetic cantilever; two permanent magnets are located symmetrically near the free end (Fig. 2-6 (c)). Due to the attractions, the ferromagnetic beam has three equilibrium positions (statically bi-stable configuration), and the vibration mode has the form of the bi-stable *Duffing* resonance. The magnetic force based nonlinear resonators typically require macro device size due to the assembly of magnets. The prototypes shown in [48-50] are in macro scale.

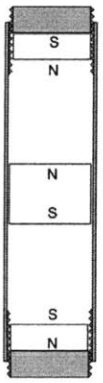

(a)

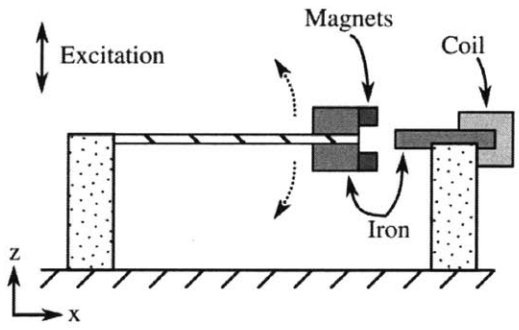

(b)

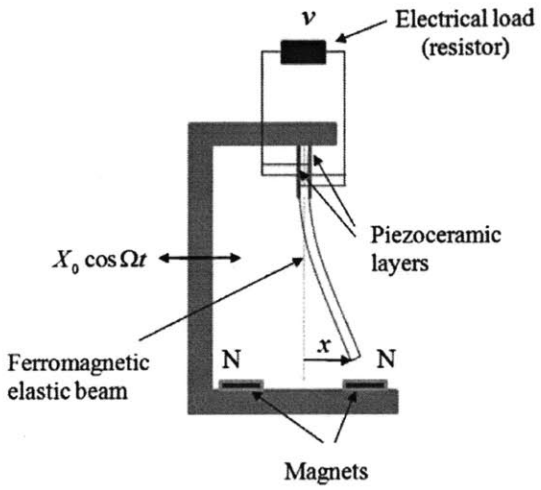

(c)

Figure 2-6 (a) A schematic diagram of the magnetic levitation system [48]. (b) A schematic diagram of cantilever – magnets energy harvester [49]. (c) A schematic of bi-stable oscillator based broadband energy harvester [50].

Nonlinear resonance may also be implemented by designing special mechanical structures. The wideband piezoelectric energy harvester in [51] was realized by exerting an axial compression and forming a buckled configuration, to make a bi-stable oscillator. A piezoelectric beam is clamped on both ends on a base excited vertically. One of the two clamps is free to move to compress and buckle the clamped beam as shown in Fig. 2-7 (a). [52] demonstrated an electrostatic energy harvester utilizing a mechanical softening spring to increase the bandwidth. The nonlinearity was achieved by using the suspension beam with an angle. When the spring deflects in the negative direction of the x-axis, a compressive axial force is first built up, and beyond a certain displacement, the axial force changes to tension. In positive direction along x-axis, axial force is always tensile. The asymmetric force–displacement in the suspension therefore has a nonlinear spring softening behavior.

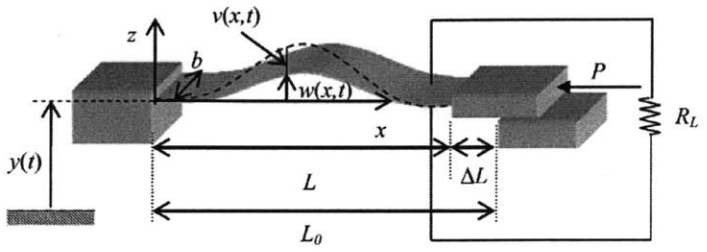

(a)

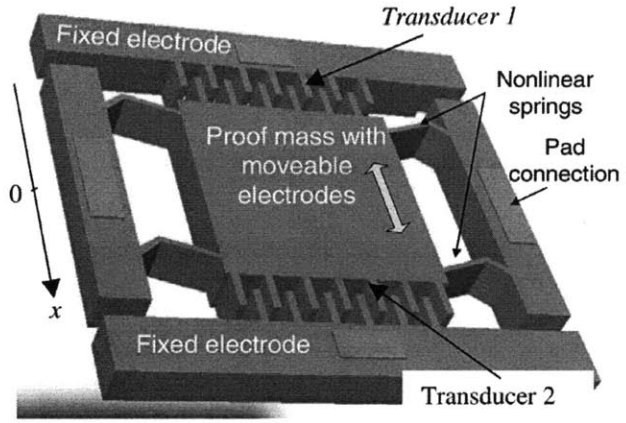

(b)

Figure 2-7 (a) Schematic diagram of piezoelectric buckled bridge [51]. (b) A schematic of MEMS electrostatic energy harvester with nonlinear suspension [52].

Lower Frequency

A conversion from low frequency to high frequency has been presented to lower the operating frequency of energy harvesters. Instead of harvesting energy from single resonator, the energy absorption from environment and energy conversion from mechanical domain to electrical domain has been divided to two steps. The ambient vibrations, excite a resonator at low frequencies in the first stage, and then the kinetic energy is transferred to a much higher frequency resonator for conversion at the second stage [53]. This method may enable power harvesting at low frequency. [54] demonstrated an electromagnetic energy harvester working at low acceleration (0.1–0.5

m/s^2), and low frequency (2–30 Hz) with an average power of 2.3 μW. The device absorbs ambient kinetic energy by using a large mass. The low-frequency motions of the suspended mass magnetically excite the magnets in coils, which then resonate at higher frequencies. [55] showed a piezoelectric version of energy harvester using the same up-converting method. To resonate with low-frequency ambient vibrations, the resonators in [54] used a large mass, which makes the whole device size increases; the volume of space where components can move is 43 cm^3 (68 cm^3 including the casing case).

Some piezoelectric energy harvesters are compared in Table 2-1.

Table 2-1 Comparison of piezoelectric energy harvesters.

Reference	Dimension	Power	Energy/power density	Voltage	Frequency	Load
White 2001 [56]	N/A	2μW	N/A	0.816V	80 Hz	333kΩ
Shenck 2001 [26]	5 × 5 × 0.038cm PZT	8.4mW	8.8mW/ cm^3	64.8 V	N/A	500kΩ
Roundy 2003 [2]	1 cm^3	~80μW	~80μW/ cm^3	~6V	100Hz	250kΩ
Jeon 2005 [6]	170 μm × 260 μm (PZT)	1μW	0.74mW h/cm^2	2.4 V	13.9kHz	5.2MΩ
Muralt 2009 [57]	0.8mm × 0.4mm × 2μm (piezo)	1.4μW	437μW/cm^2	1.6 V	870Hz	-
Liu 2011 [58]	-	85.5nW	33μW/cm^3	164 mV	30-47Hz	1 MΩ
Massaro 2011 [59]	Length ~ 500μm Thickness ~ 0.7μm	1.3nW	30.2mW/ cm^3	2.5 mV	64Hz	11 Ω
Miller 2011 [60]	-	1.7nW	-	-	31–232Hz	9 kΩ

2.2.4 Previous Work of Our Group

1st Generation Design

In 2005, a PZT based MEMS power-generating device was developed in our group [6]. The basic structure was a cantilever with a proof mass at the end (Figure 2-8 (b)). The top electrode was patterned into an interdigitated shape to employ the d_{33} mode of the piezoelectric transducer (Figure 2-8 (a), (b)). This new configuration made the device generate 20 times higher voltage than that of the d_{31} mode design. At the resonant frequency 13.9 kHz, generated 1μW of continuous electrical power at 2.4Vdc. The corresponding energy density is 0.74mWh/cm^2, which compares to the values of lithium ion batteries.

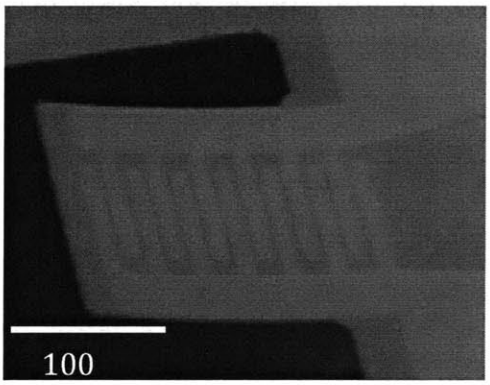

(a)

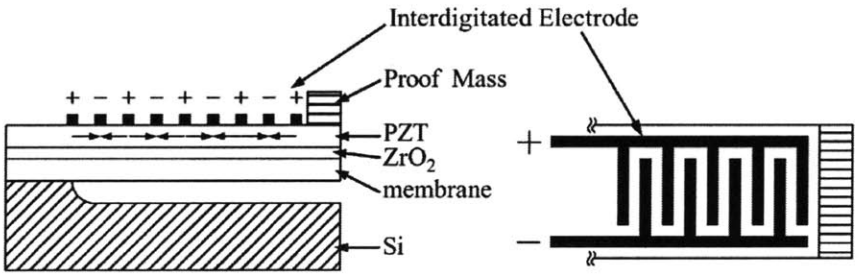

(b)

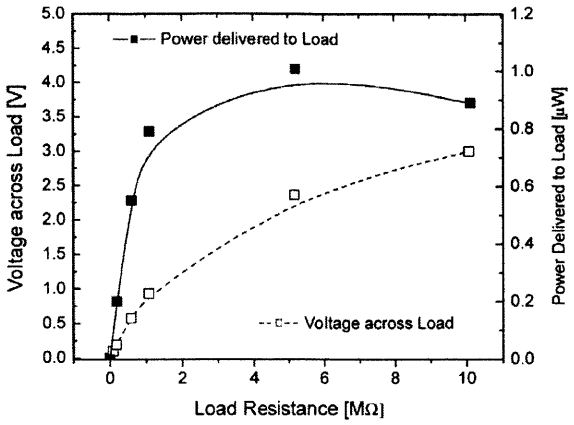

(c)

Figure 2-8 1st generation PMPG. (a) SEM image of cantilever beam. (b) Schematic of interdigitated electrodes. (c) The load voltage and power delivered to the load vs. load resistance at 13.9 kHz resonance respectively. [6]

3rd Generation Design

In 2010, Arman Hajati successfully developed a novel piezoelectric micro energy harvester, which achieved an ultra-wide bandwidth of >20%, a maximum peak-to-peak voltage of 1.5V (Figure 2-9 (c)), a maximum extractable power of 45μW (Figure 2-9 (d)), and high power density of $2W/cm^3$. More than one order of magnitude improvements in comparison to the devices previously reported in both bandwidth and power density convinced us that this is a promising way to harvest minute energy and to be employed for real-world applications.

The basic design is based on a doubly clamped beam resonator. Four of these resonators are arranged perpendicular to each other and form one energy harvester, which is about a US quarter coin size 6mm×6mm×5.5μm (L×W×H) (Figure 2-9 (a)). At large deflection, a net stretching besides bending is activated, resulting in non-linear resonance, which completely changes the dynamic response (Figure 2-9 (b)) and turned out to be desirable for energy harvesting, this will be explained in detail in the next chapter. Although the

new design manifests superiorities, the test results showed a resonance frequency of 1.3kHz and excitation amplitude was at 4~5g. This is a discrepancy from the real ambient environment, which usually have vibrations of ~100Hz and <0.5g. Therefore, new designs for closing the gaps are needed.

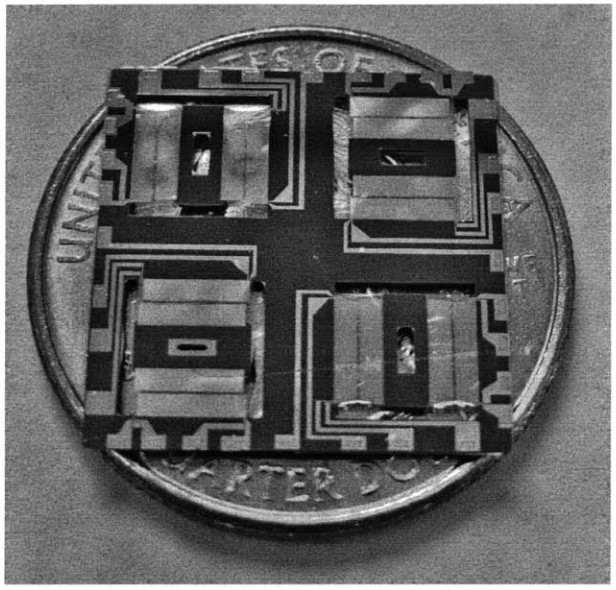

(a)

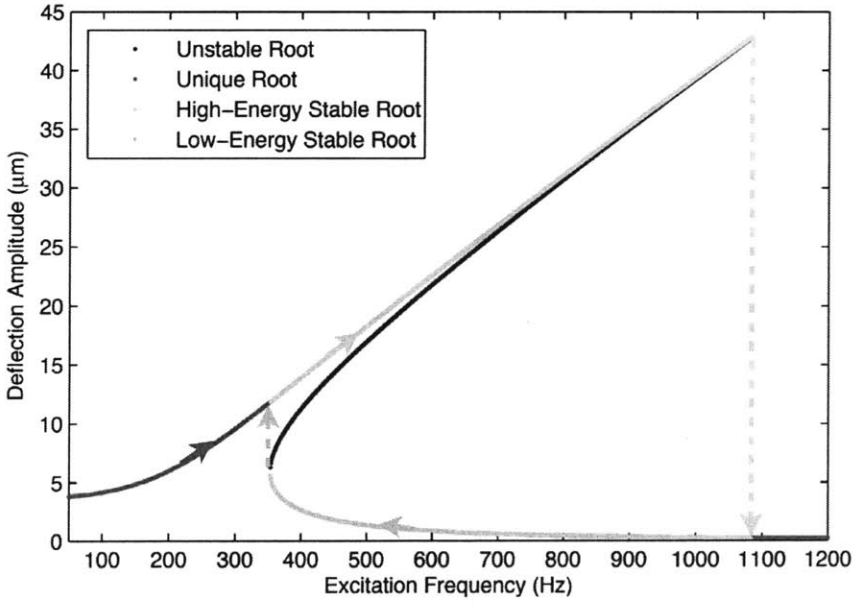

(b)

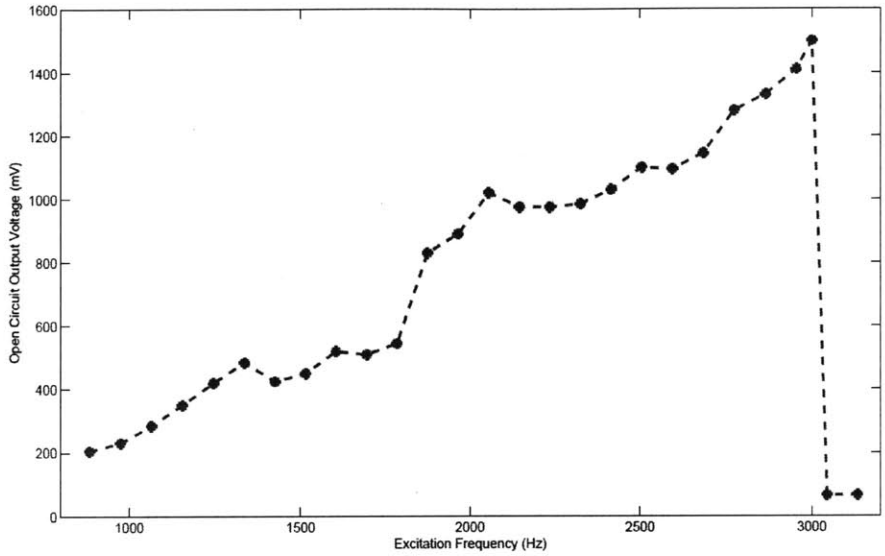

(c)

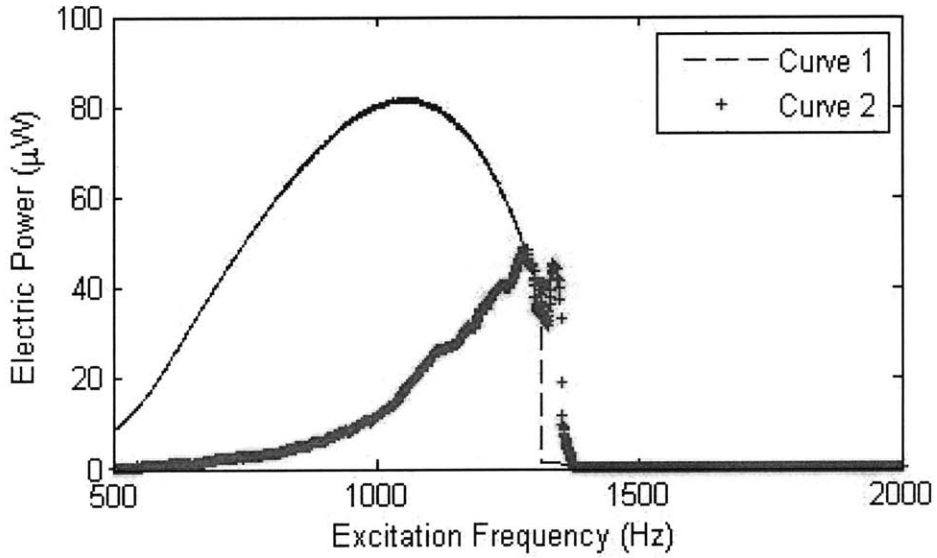

(d)

Figure 2-9 3rd generation PMPG. (a) Photo of fabricated device on a coin. (b) Dynamic response of nonlinear resonator. (c) Open circuit voltage versus frequency [5]. (d) Estimated power versus frequency [5].

2.2.5 Nonlinear Resonance Based Energy Harvesting

Statics

For designing a transversely vibrated beam resonator, statics is the starting point. At large deflection, which means the deflection is comparable the thickness of the beam, a doubly clamped beam not only bends but also be stretched and elongate so that the fixed boundary conditions are satisfied and the whole structure remain geometric compatibility. By using variational method, the load-deflection characteristic for a doubly clamped rectangular beam with a point load at center is,

$$F = \left\{\left(\frac{\pi^4}{6}\right)\left[\frac{EWH^3}{L^3}\right] + \left(\frac{\pi^2}{2}\right)\left[\frac{\sigma_0 WH}{L}\right]\right\}\delta + \left(\frac{\pi^4}{8}\right)\left[\frac{EWH}{L^3}\right]\delta^3 \qquad \text{Eq. 2.8}$$

The solution has two parts; the first part is a proportion to deflection and results from the small-amplitude bending, while the second nonlinear term comes from stretching and is proportional to deflection cubed. The nonlinear term implies that the equivalent stiffness of the beam is not constant but increases as the deflection get larger. A scrutiny on this equation provides insights on understanding the nonlinear spring and the design of it.

Dynamics

To model and analyze the doubly clamped beam-based nonlinear resonator, it is assumed that the base is fixed and a sinusoidal force is applied to the proof mass. Then a mechanical lumped model (Figure 2-10 (b)) and electrical lumped models (Figure 2-10 (c), (d)) are constructed, which consist of a proof mass, a linear spring due to bending, a nonlinear spring due to stretching, a mechanical damper and an electrical damper. The dynamic equation of the mass-spring-damper system is,

$$m\ddot{x} + b\dot{x} + k_L x + k_N x^3 = F\cos(\omega t) \qquad \text{Eq. 2.9}$$

where m is the proof mass, b is the total damping including structural damping, aerodynamic damping and electrical damping, k_L is the linear stiffness, k_N is the nonlinear stiffness, ω is the excitation frequency, and t is time.

Substituting linear and nonlinear stiffness's and damping coefficients into Eq. 3.2 and solving for the deflection, a cubic equation can be obtained [5]:

$$\frac{9k_N^2}{16}\left(1+\frac{b_s^2}{k_L^2}\omega^2\right)x^6+\frac{3k_N}{2}\left[k_N+\frac{(b_a+b_e+b_s)b_s}{k_L}\omega^2-m\omega^2\right]x^4 \\ +\left[(b_a+b_e+b_s)^2\omega^2+(k_L-m\omega^2)^2\right]x^2-m^2a^2=0 \qquad \text{Eq. 2.10}$$

where b_s, b_a, b_e are structural damping, aerodynamic damping and electrical damping respectively, and a is the excitation acceleration. The multiple solutions of Eq. (3.3) are illustrated in Figure 2-9 (b). The tilted peak resulting from the nonlinearity of *Duffing* mode resonance indicates a wider bandwidth, if the resonator can stay on the upper envelope (high-energy) of this curve. Depending on the initial conditions, a system may work at different regions denoting by different colors in Figure 2-9 (b). If sweeping frequency from low to high, the system will work in the unique solution region first at small deflection, then the deflection will increase along the high-energy stable region, until it jumps down to low energy stable region. If sweeping the frequency high to low, the response will go along the low-energy stable region until it jumps up to high-energy stable region again. The jump-down and jump-up frequencies are marked by blue and green arrows respectively in Figure 2-9 (b). It is obvious that working in high-energy stable region is desired, so the system should be designed to make the frequencies of ambient vibrations fall in this range.

The deflection of linear resonators drops dramatically when the system goes off-resonance, and a sharp peak that has a narrow bandwidth is formed. In contrast, it can be seen in Figure 2-9 (b) that for a nonlinear resonator, the deflection increases steadily in a wide frequency range before it jumps down to low level. By equating the stored energy

due to nonlinear stiffness and an equivalent linear stiffness, we can find the equivalent stiffness to be $\frac{3}{4}k_N x^2$. Then, the equivalent natural frequency of the undamped nonlinear resonator can be estimated as [5],

$$\omega = \sqrt{\frac{k_L + 0.75k_N x^2}{m}} \qquad \text{Eq. 2.11}$$

When the excitation frequency is lower than the jump-down frequency, the deflection tends to decrease from the peak value, but that decrease also lowers the resonant frequency of the nonlinear system, so that the system keeps working close to resonance. The nonlinear stiffness acts as a negative feedback which results in a much wider frequency range compared to a linear system.

Wide Bandwidth

In linear systems, the electrical impedance should match the mechanical impedance to achieve maximum power [61]. But for a nonlinear system, electrical damping can surpass the mechanical impedance to generate higher output power. By combining the mechanical elements in Figure 2-10(c) except for nonlinear spring, a simplified electrical circuit with impedances is generated in Figure 2-10 (d). Z_M, Z_N, Z_E are mechanical impedance, impedance of nonlinear spring and electrical impedance respectively. It is obvious that when electrical impedance increases, the total impedance tends to increase, which will make the deflection drop, but the variable nonlinear impedance $\frac{0.75k_N x^2}{s}$ also tends to decrease because of the smaller x, and that tends to decrease the total impedance and increase the deflection. Consequently, this nonlinear impedance serves as a negative feedback and stabilizes the deflection when electrical damping changes. This effect can be clearly seen in Figure 2-11 (a) which compares the normalized deflections of a linear system and a nonlinear system with various total damping. Figure 2-11 (b) shows that for either fixed or varying electrical damping, the bandwidth of nonlinear system is much wider than that of linear systems.

Since extractable electrical power is proportional to electrical damping, we can increase the output power by increasing electrical damping until it pushes the resonator into instability, resulting in jump-down to low energy state. A smart electronic interface such as adaptive SSHI will be ideal to implement this. Figure 2-11 (b) compares the maximum extractable power of linear and nonlinear systems.

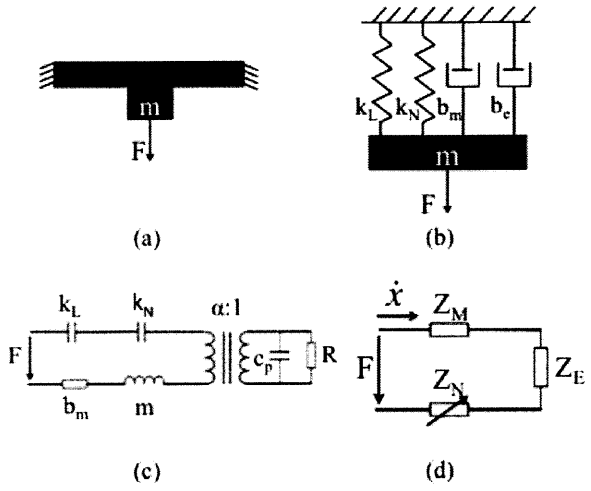

Figure 2-10 Lumped models of nonlinear resonator based energy harvester. (a) Simplified dynamic model. (b) Mechanical lumped model. (c) Electrical lumped model. (d) Electrical lumped model with impedances.

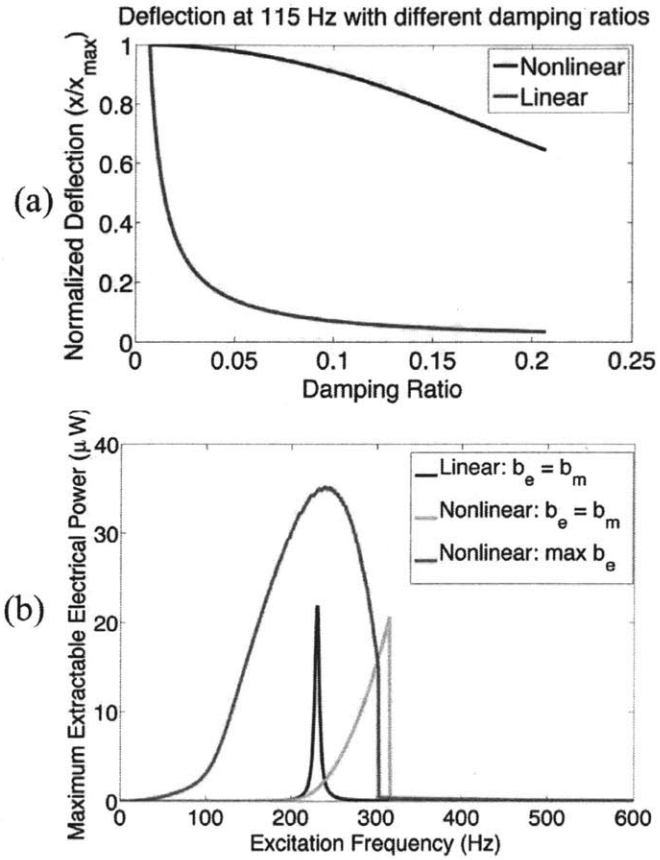

Figure 2-11 Comparison between linear and nonlinear systems behavior (simulation). (a) Deflection of linear and nonlinear systems versus damping ratio. (b) Maximum extractable electrical power comparison.

Chapter 3 Design

3.1 Criteria on the Design of Piezoelectric Vibration Energy Harvesters

From a comprehensive review on the history of energy harvester development and the state-of-the-art progress made in this area, the author would like to make a discussion on the criteria of a good piezoelectric vibration energy harvester design and the design guidelines.

The criterion of a good design for ambient vibration energy harvester may be summarized as follows:

- **Compactness**
- **Output Voltage**
- **Output Power (Density)**
- **Bandwidth**
- **Operating frequency**
- **Vibration Level**
- **Lifetime**

A compact design guarantees good compatibility when embedding into larger systems. A great portion of vibrational energy harvesters are aimed at powering wireless sensor networks, embedded systems in automobile and civil structures, and implantable devices in human body. In these applications, a compact size is almost necessary to make energy harvester a feasible power source. Moreover, MEMS scale energy harvester is able to make full advantage of micro-fabricaion, which makes it possible to manufacture low-

cost energy harvesters in large scale. Miniaturized designs also tend to increase the energy density of the device.

Like all power sources, voltage is one of the most important parameters characterizing the performance. The voltage should be high enough to power the target devices, which may vary according to the applications. Theoretical analysis shows that piezoelectric energy harvesters are able to provide high voltages. From the review, the demonstrated devices which provide from millivolts to several volts also proved this experimentally. Using d_{33} modes, high voltage is not a challenge any more, and it enables the piezoelectric energy harvesters to power a great variety of devices.

Output power or power density is another key parameter in that it directly relates to what kind of load devices can be powered. Power density is more important than output power when comparing different devices, since the size of piezoelectric energy harvesters varies much, and output power is proportional to the volume of the piezoelectric materials. Thus, power density provides a more accurate measure on the efficiency of the whole device. A smaller device with a high power density may be easily stacked to provide high power needed at a high total efficiency.

Bandwidth was not fully recognized as a key parameter at the beginning of the development of piezoelectric energy harvesters, but it has attracted enough attention from researchers in the past several years. The importance of bandwidth arises from the inherent nature of ambient vibrations, which is that the frequency of the vibration varies with time. The conventional linear resonance based energy harvesters suffers from the gain-bandwidth dilemma, which means for a high gain design, which is desirable for efficient energy conversion, the bandwidth is inevitably narrow. For example, the design in [7] has a 2% bandwidth. Such a narrow bandwidth implies a significant decrease in generated power in real applications, as the frequency varies. Hence, knowing the frequency spectrum of the vibration in target applications is important, and the energy

harvester should have a wide enough bandwidth to generate power in that specific spectrum.

Roundy et al. [2] and duToit et al. [61] have examined the vibrations from some common ambient vibration sources, their acceleration amplitudes and excitation frequencies are listed in Table 3-1. It can be concluded that typical ambient vibrations have accelerations below 1g and excitation frequencies below 200 Hz.

Table 3-1 Acceleration amplitudes and frequencies of common ambient vibration sources [2, 61].

Vibration Sources	Accl. [m/s^2]	Freq. [Hz]
Car engine compartment	12	200
Base of 3-axis machine tool	10	70
Blender casting	6.4	121
Microwave oven side	4.2	148
Clothes dryer	3.5	121
Car instrument panel	3	13
Door frame just after door closes	3	125
HVAC vents in office building	0.2-1.5	60
Windows next to a busy road	0.7	100
Car hood—3000 rpm	0.26	148
Second story floor of busy office	0.2	100
A/C duct side (high setting)	0.1	54
Office desk	0.09	120
Computer side panel	0.04	276
Bridge railing	0.02	171
Small tree	0.003	30

To resonate the energy harvester and generate maximum amount of power, the natural frequency should match that of the ambient vibrations. Many energy harvesters, especially those in MEMS scale have a resonant frequency in the order of kHz or even higher, which may render them useless in real applications. A challenge is to lower the resonant frequency of the MEMS scale energy harvester to 10^2 Hz range.

Similarly, the excitation level of ambient vibrations is typically small compared to the usual setting of experiment testing. To demonstrate a practical design, energy harvesters

should be tested with low-g vibrations. Since the available energy is proportional to g-level, design considerations should be made to compensate this weaker excitation to generate a considerable amount of power.

Lastly, the lifetime of the piezoelectric energy harvester should be taken into account. The original purpose to adopt generative power sources such as piezoelectric energy harvesters and replace non-generative power supplies such as batteries is that the lifetime of batteries is limited, while theoretically energy harvesters generates power perpetually as long as there is a ambient energy source such as vibrations, thermal gradient, fluid flow and so on. However, the real device may suffer from material fatigue, cruel environment and other unexpected conditions. To make sure energy harvesters have a much longer lifetime than non-generative power sources is necessary. Not much research has been done to investigate the lifetime of piezoelectric energy harvesters, in the future, research on material, packaging and some other aspects may carry out when commercializing these devices.

3.2 Design Goals

As reviewed in background chapter, our group has developed an ultra wide-bandwidth micro-energy harvester by exploiting the non-linear resonance of a doubly clamped MEMS-scale resonator. Two orders of magnitude improvements in both the bandwidth (>50% of the peak frequency) and the power density (up to $2W/cm^3$) in comparison to the devices ever reported, a maximum peak-to-peak voltage of 1.5V, plus a compact size as a US quarter manifest the superiorities of the new design. However, the high resonant frequency (1.3kHz) and the high-g acceleration requirement (4.5g) prevent this technology from being applicable to real applications. Therefore, the design goals for a new generation of design are clearly defined: to lower the working frequency to under 200 Hz and the excitation force level to below 0.5g while keeping the good features of the previous design. Toward this goal, theoretical modeling and analysis, numerical

simulations, explorations of different design ideas and parameter optimization have been done to generate a new improved design. The following sections in this chapter present these work in detail.

3.3 Design Ideas

At the beginning stage of design, different new design ideas were generated. Each one of them was brought about for some considerations. Investigations on them in different depth were made. To avoid research on the similar ideas in the future and to keep a record of the design ideas and related thoughts on them for later design use, it might be beneficial to briefly explain these ideas before diving into details on the proposed designs.

3.3.1 Multiple Doubly Clamped Beams

The idea of employing multiple beams rather than a single doubly clamped beam is to increase the stability of the resonant structure. As shown in Figure 3-1, with more beams, the clamped ends are in more directions, the vibration in these directions are prohibited, and only out of plane motion dominates. Moreover, it has been proved that multiple clamped beams resonator is equivalent to a single clamped beam, and shows a nonlinear response.

The change of geometry from a single beam to multiple beams changes the width to length ratio, which is related to resonant frequency, and the effective area, which is related to output power. The relationship between the number of beams and w/l ratio and effective area has been investigated. Assume the length of the outer rectangle remains the same, which limit the device size, and the apothem of the inner polygon remains the same, which fixed the size of the proof mass, then we have the formula of w/l ratio for different number of beams:

$$\frac{w}{l} = N \cdot \frac{r \cdot \tan\left(\frac{\pi}{2N}\right)}{R} \qquad \text{Eq. 3.1}$$

and the formula of the effective area is,

$$A = 4Nr(R-r) \cdot \tan\left(\frac{\pi}{2N}\right) \qquad \text{Eq. 3.2}$$

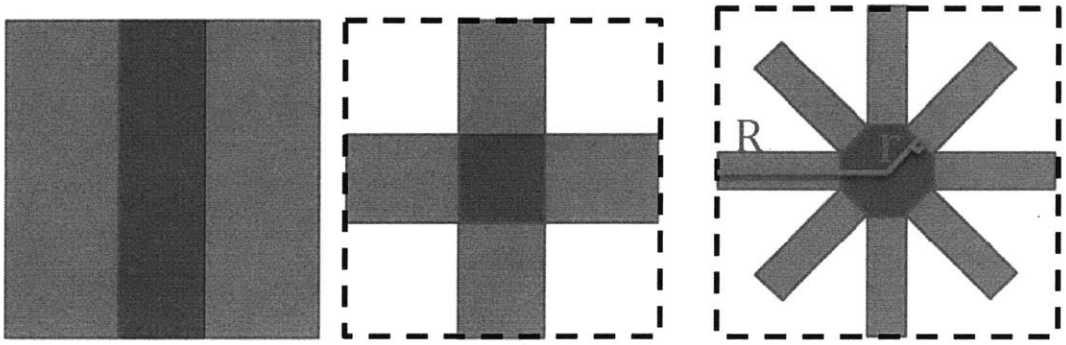

Figure 3-1 Schematic of multiple doubly clamped beam designs.

To see how w/l ratio and effective area change with number of beams, we may choose *R* to be 2.5mm and r to be 0.5mm, then Figure 3-2 (a) shows the trends. As can be seen, *w/l* ratio decreases with number of beams but is bounded to ~0.31, which limited the lowering the frequency. Effective area also decreases with increasing number of beams (Figure 3-2 (b)), which means lower power since the output power is proportional to the effective area. Hence, this design has been abandoned.

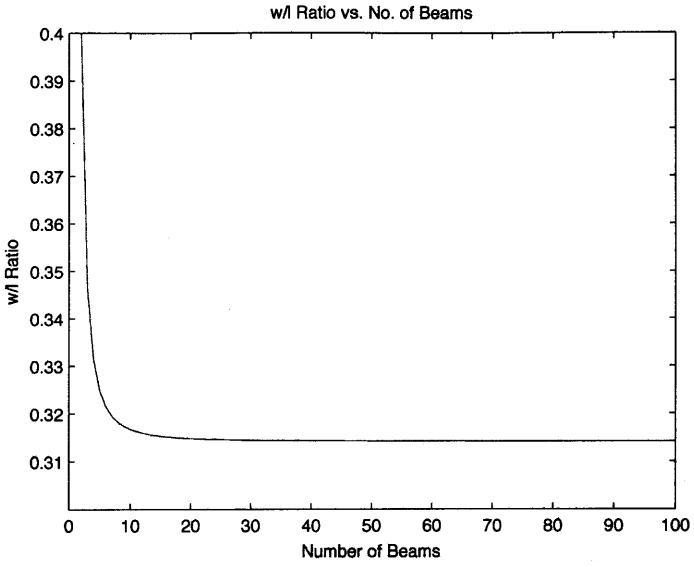

(a)

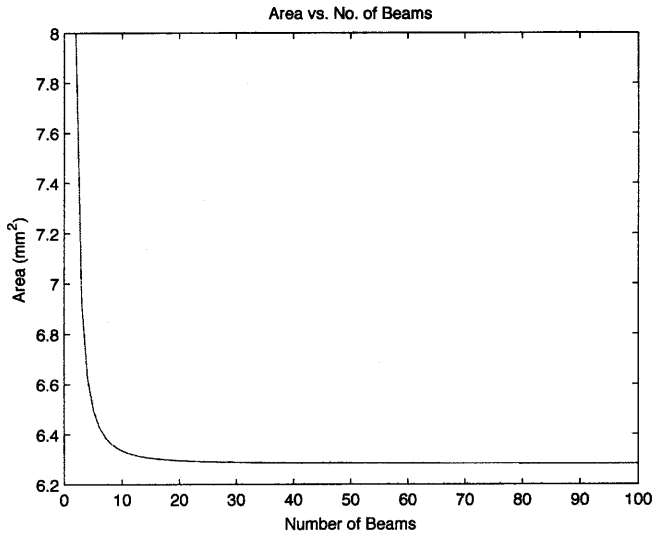

(b)

Figure 3-2 (a) Width to length ratio versus number of beams. (b) Area versus number of beams.

3.3.2 Circular Plate

When searching for mechanically stable designs, a circular plate emerges. Circular plate is a natural extension of multiple doubly clamped beam designs discussed above, we may imagine a circular plate is composed of an infinite number of doubly clamped beams.

When clamped the edge of a circular plate and loading at the center, there will only be out of plane deflection and no hoop deflection or rotation as may happened in a single doubly clamped beam, which would take part of the strain energy away. Therefore, a circular plate is a stable structure, and a possible design was made as shown by the schematic in Figure 3-3. A circular plate is clamped at the edge and a cylindrical proof mass is at the center of the circular plate. PZT would cover the full top surface and a curved d_{33} electrode was specially designed for the circular geometry.

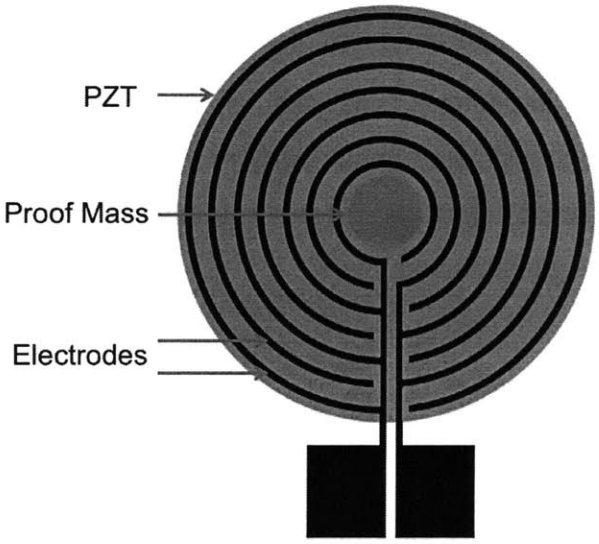

(a)

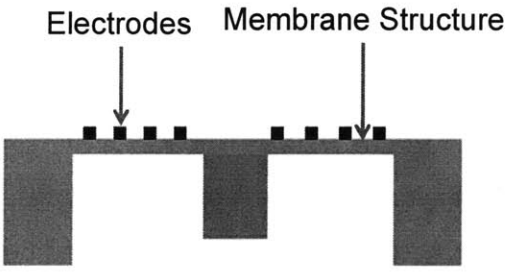

(b)

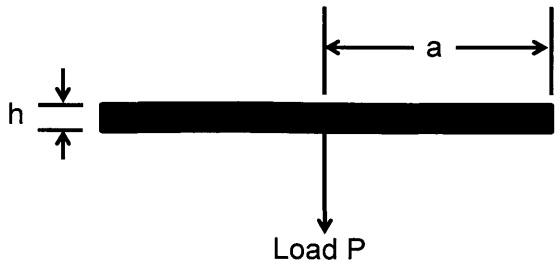

(c)

Figure 3-3 Schematics of circular plate design. (a) Top view. (b) Side view. (c) Dimensions of circular plate.

Although circular plate has unparalleled stability, one important concern is that if the circular plate structure still possess nonlinearity as a single doubly clamped beam does. According to [62], at small deflection, the vertical deflection on a clamped circular plate with a center point load can be found by:

$$w = \frac{\mathrm{Pr}^2}{8\pi D}\log\frac{r}{a} + \frac{P}{16\pi D}\left(a^2 - r^2\right) \qquad \text{Eq. 3.3}$$

where P is the center point load, w is the vertical deflection at r, a is the radius of the circular plate, D is the flexural rigidity of the plate and is:

$$D = \frac{Eh^3}{12\left(1-v^2\right)} \qquad \text{Eq. 3.4}$$

where h is the thickness of the plate, E is the Young's modulus, v is the Poisson's ratio. If Poisson's ratio is 0.3, the center load and the center vertical deflection can be calculated as,

$$P \approx 4.60 \cdot \frac{Eh^3}{a^2} w \qquad \text{Eq. 3.5}$$

which shows a linear relationship. However, we should expect something different would happen just as a straight doubly clamped beam. At large deflection, the center vertical deflection and center point load has the relationship [62]:

$$\frac{w_0}{h} + A\left(\frac{w_0}{h}\right)^3 = B\frac{Pa^2}{Eh^4} \qquad \text{Eq. 3.6}$$

where w_0 is the vertical deflection of the center, h is the thickness of the plate, a is the radius of the circular plate, E is the Young's modulus, A and B are coefficients. For immovable edge circular plate, A is 0.443 and B is 0.217 [62]. Plug in these constants and rearrange Eq. 3.6 yields this load-deflection characteristic:

$$P = \frac{Eh^3}{Ba^2}w_0 + \frac{AEh}{Ba^2}w_0^3 \approx 4.61\frac{Eh^3}{a^2}w_0 + 2.04\frac{Eh}{a^2}w_0^3 \qquad \text{Eq. 3.7}$$

Eq. 3.7 is similar to the load-deflection of a doubly clamped beam. The solution has two parts, the first part is linear and the second has the deflection cubed. It is obvious that at large deflection, a circular plate behaves like a stiffening spring which is similar to a clamped beam. However, circular plates have larger stiffness, which makes it harder to bring the resonant frequency down.

3.3.3 Large In-plane Proof Mass

To lower the resonant frequency while keeping mechanical stability, large in-plane proof mass with new beam arrangements were designed. Figure 3-4 (a) shows a crossing beam with four ends fixed and a large proof mass sits in the center. The structure is equivalent to a doubly clamped beam and with enhanced stability by restraining two perpendicular directions. Figure 3-4 (b) shows another scheme, which consists four doubly clamped beams and one big proof mass in the center. Although these designs have their merits, they have smaller effective areas, and for the second design, the vibrating proof mass will twist the beams because of the asymmetry.

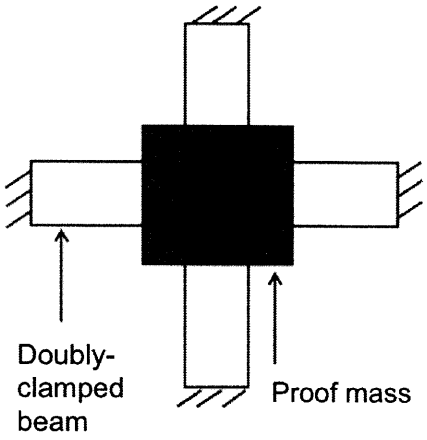
Doubly-
clamped
beam
Proof mass

(a)

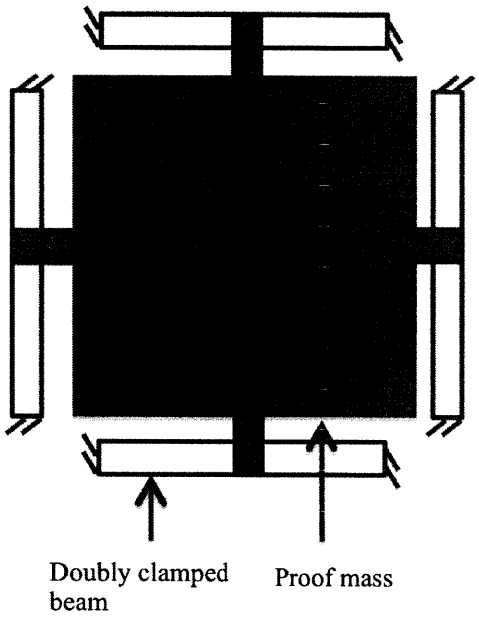
Doubly clamped
beam
Proof mass

(b)

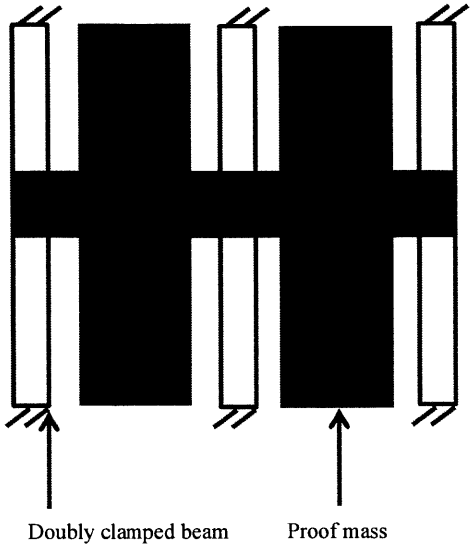

(c)

Figure 3-4 Schematics of large in-plane proof mass designs.

3.3.4 Coupled Beams Design

Prof. Firas Sammoura and I have investigated coupled beams design, since it is based on a different working principle might have a wide bandwidth. The basic idea is to make a multiple mass-spring-damper systems with different resonance frequency (different stiffness and masses which can be designed), and couple them (Figure 3-5 (a)) so that when excitation frequency is close to the natural frequency of one of the system, it increase the vibration of other non-resonating systems, and this interference can make the whole system have a wider bandwidth.

Mechanical modeling with two mass-spring-damper systems with one coupling has been made (Figure 3-5 (b)). The transfer functions are,

$$\frac{X_1}{F} = -\frac{BM_1 + CM_2}{(AB - C^2)M} \qquad \text{Eq. 3.8}$$

$$\frac{X_2}{F} = -\frac{CM_1 + AM_2}{(AB - C^2)M} \qquad \text{Eq. 3.9}$$

where A, B, C are

$$A = M_1 s^2 + (b_1 + b_2)s + (K_1 + K_2) \qquad \text{Eq. 3.10}$$

$$B = M_2 s^2 + (b_2 + b_3)s + (K_2 + K_3) \qquad \text{Eq. 3.11}$$

$$C = b_2 s + K_2$$

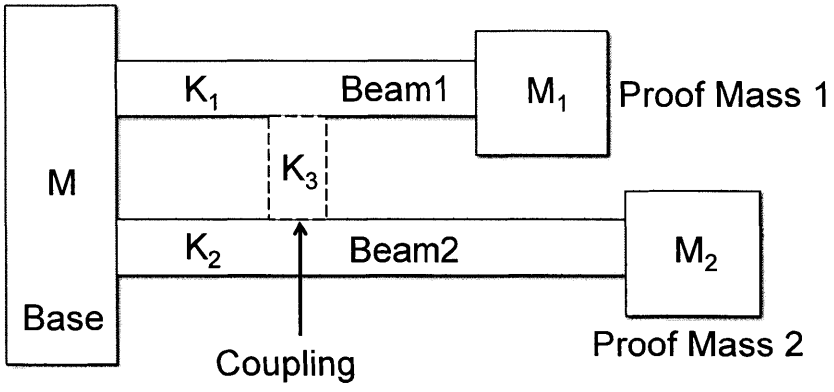

(a)

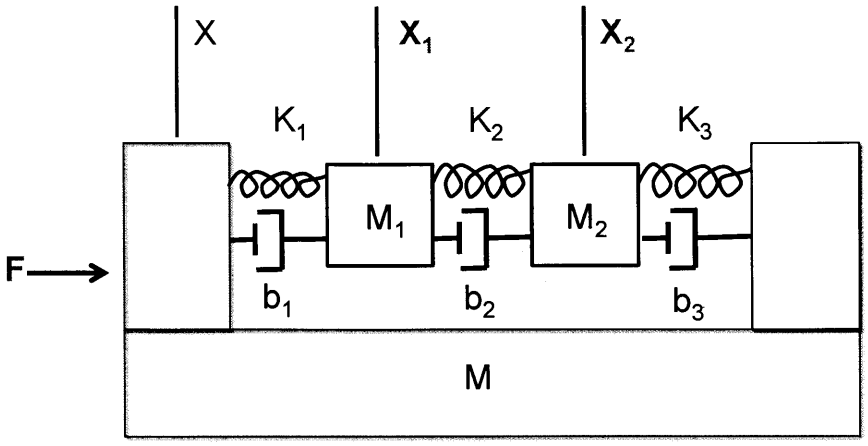

(b)

Figure 3-5 Models of coupled beam design. (a) Schematic of coupled beam design. (b) Mechanical lumped model.

Choosing all the parameters so that the two mass-spring-damper systems have slightly different natural frequencies, and plugging in those numbers, we can obtain the Bode plots for X_1 and X_2 before and after coupling (Figure 3-6). The results show that the bandwidth is widened, but at the same time, the magnitudes drop, which means less power can be generated. This trade-off made us give up this design.

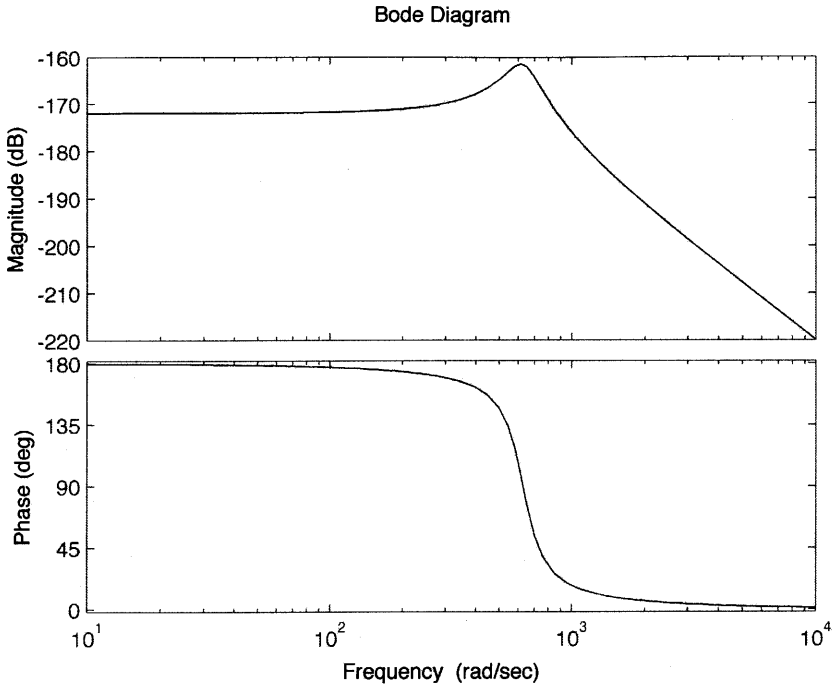
Bode Diagram
Magnitude (dB)
-160
-170
-180
-190
-200
-210
-220
Phase (deg)
180
135
90
45
0
10^1
10^2
10^3
10^4
Frequency (rad/sec)

(a)

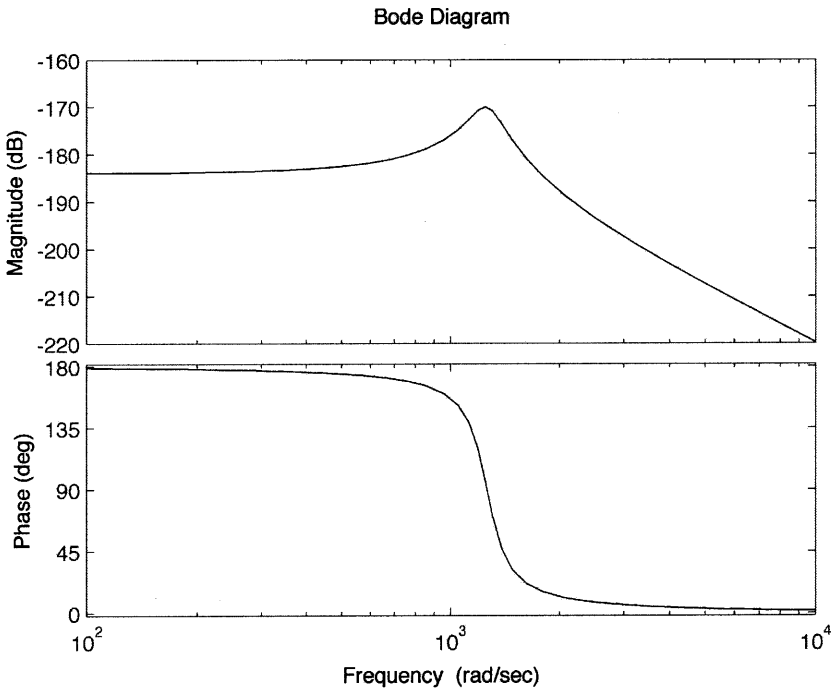
Bode Diagram
Magnitude (dB)
-160
-170
-180
-190
-200
-210
-220
Phase (deg)
180
135
90
45
0
10^2
10^3
10^4
Frequency (rad/sec)

(b)

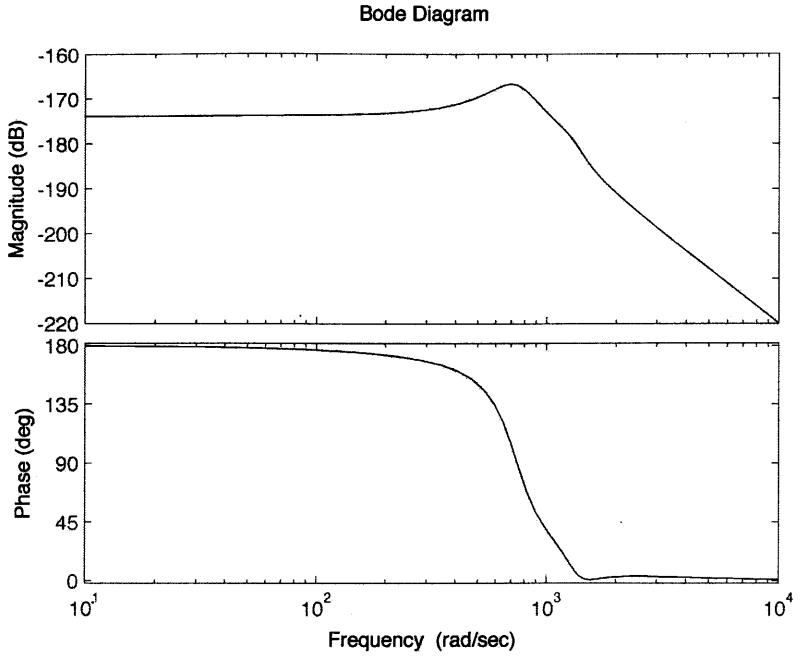

(c)

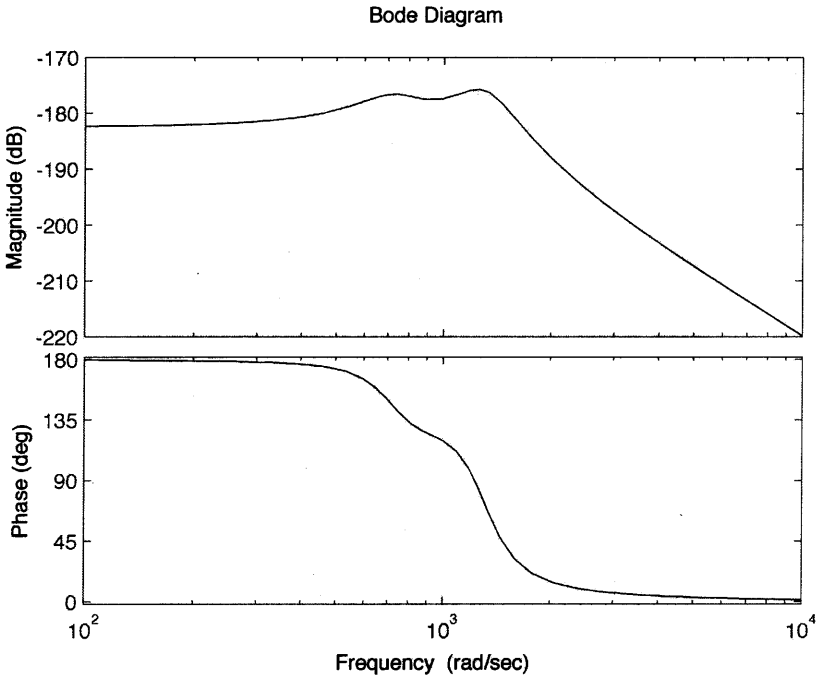

(d)

Figure 3-6 Bode plots of one coupled beam design example. (a) X_1 before coupling. (b) X_2 before coupling. (c) X_1 after coupling. (d) X_2 after coupling.

3.3.5 Doubly Clamped Serpentine Beam Design

To lower the resonance frequency of the energy harvester, except using a heavier proof mass, we can also reduce the stiffness of the beam. Both linear and nonlinear stiffness' are inversely proportional to the length cubed, which means an increase in bean length will lead to a significant decrease in resonance frequencies. But a slender straight beam may not be a good idea, since the length of it is constrained by the device dimension, say a coin size (~16mm), and it may also be challenging to maintain good stability to support a heavy proof mass by a lender beam structure. A serpentine beam structure was then come up to increase the beam length in compact size and retain mechanical stability. As illustrated by the schematic in Figure 3-7 (a), four serpentine beams are arranged perpendicular to each other, and both ends are fixed to form a similar structure as fixed-fixed beams, so that there might be nonlinear stiffness at large deflection. But one of the obvious problems of this design is that the strain or strain energy will be concentrated at the 90^{o} corners in a non-uniform distribution, which is not desirable for piezoelectric energy harvesting. Moreover, when the structure deforms, much of the deformation is torsion rather than stretching, which reduces the nonlinearity. The concentrated non-uniform strain can be seen in the FEA model in Figure 3-7 (b).

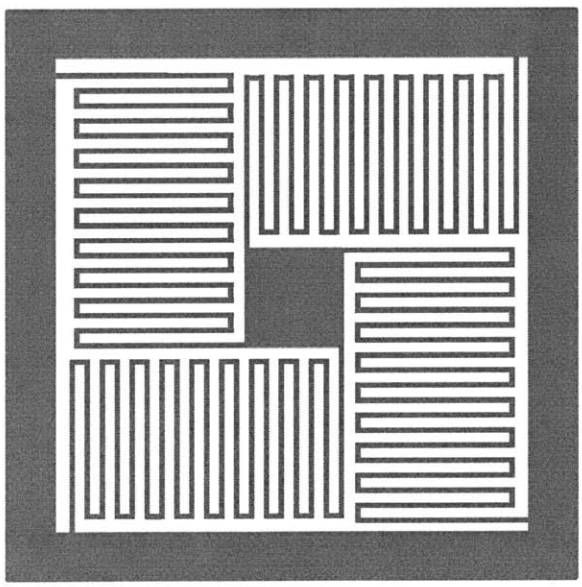

(a)

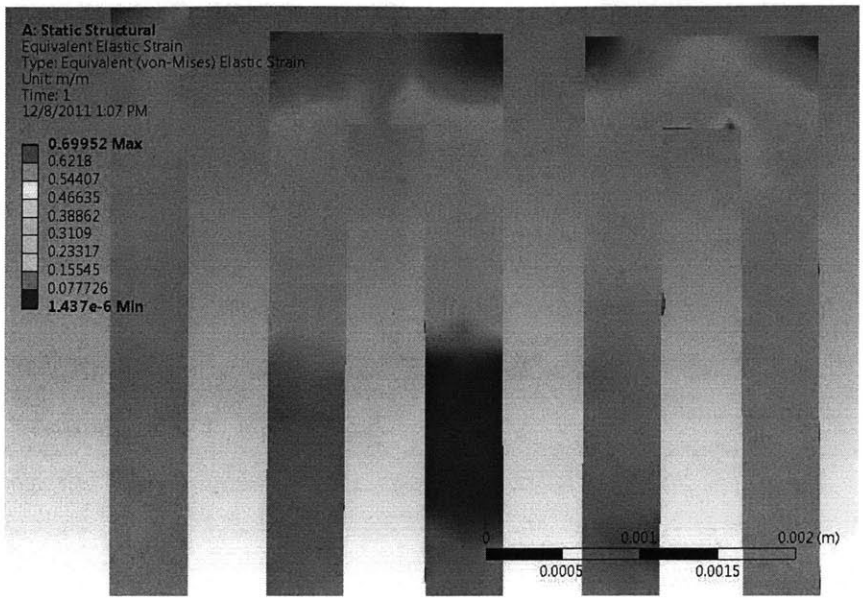

(b)

Figure 3-7 (a) Schematic of serpentine beam design. (b) Numerical simulation of strain distribution of serpentine beam.

3.3.6 Doubly Clamped Spiral Beam Design

Although the serpentine beam design seems not feasible, the special geometry that increases the length of the beam significantly is still interesting and may inspire other similar designs. The strain concentration is mainly due to the sharp corners of the beam structure; the elimination of them may solve the problem. Therefore different curved beams and their strain distribution have been explored, among which are single spiral beam, curved corner, O-ring beam, S shaped beam and doubly clamped spiral beam as shown in Figure 3-8.

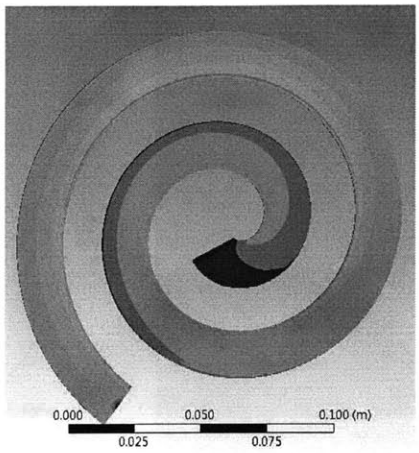
0.000
0.050
0.100 (m)
0.025
0.075

(a)

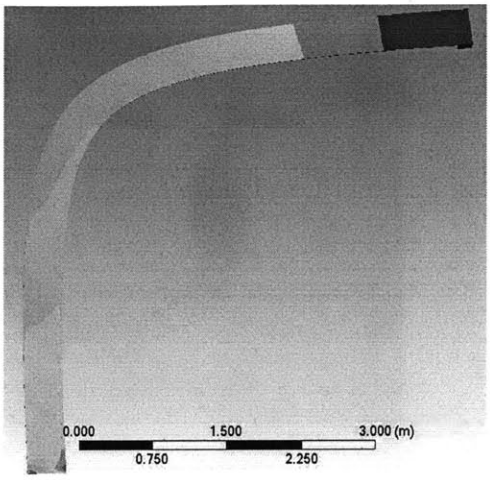
0.000
1.500
3.000 (m)
0.750
2.250

(b)

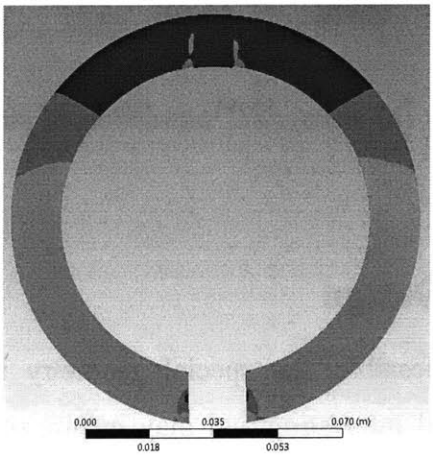
0.000
0.035
0.070 (m)
0.018
0.053

(c)

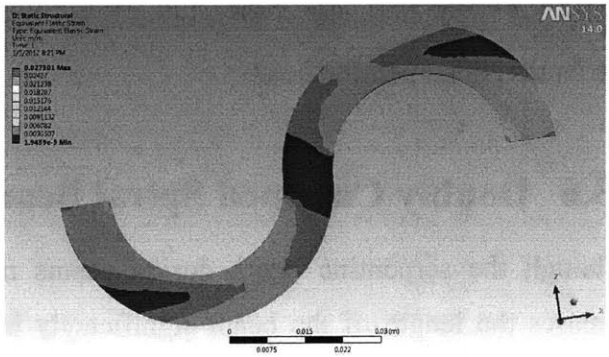
ANSYS

(d)

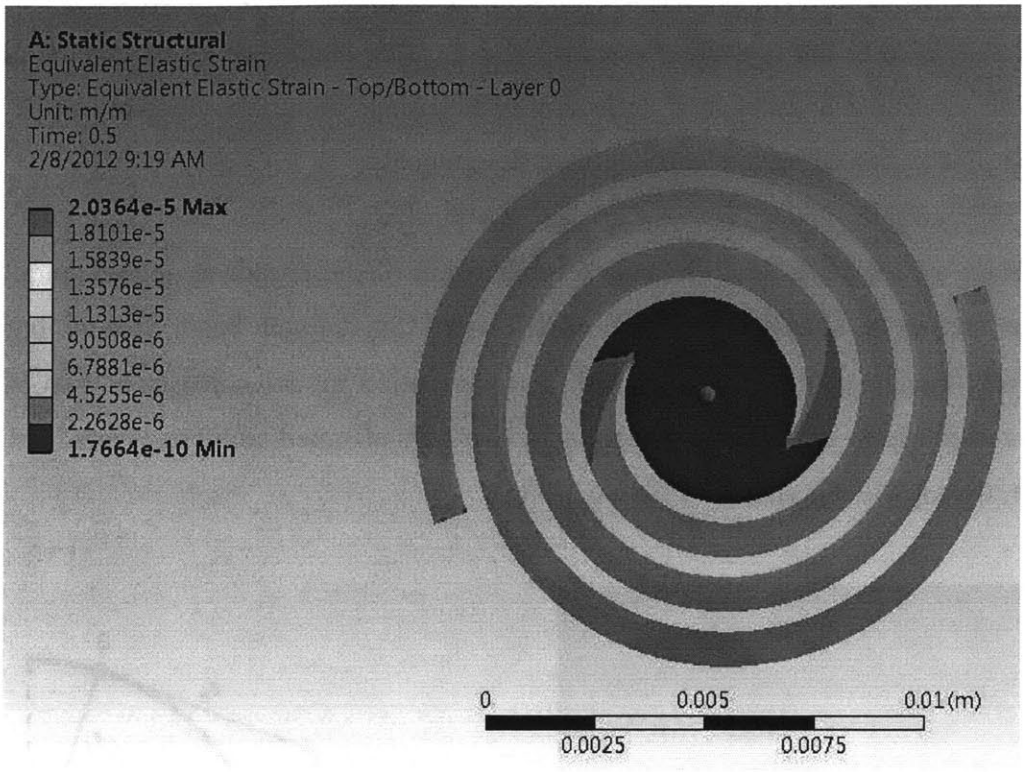

(e)

Figure 3-8 Strain distribution of curved beams. (a) Single spiral beam. (b) Curved corner. (c) O-ring beam. (d) S-beam. (e) Doubly clamped spiral beam.

The doubly clamped spiral beam has a reasonably uniform strain distribution, and the two fixed ends may introduce nonlinear stretching at large deflection. This structure allows the beam to be extremely slender while keeping the device size compact, so that the operating frequency can achieve very low level. One central issue is if the resonance of this structure possesses enough nonlinearity so that the bandwidth of the energy harvester is wide. Analytical and numerical analysis has been carried out.

Load-Deflection Characteristic of S-Beam

The load-deflection relationship is of great importance for the design of a nonlinear resonator. It not only shows if there is nonlinearity in the system and how strong it is, but also reveals the relationship between the design parameters and the design goals. For example, the dimensions in load-deflection equation determine the stiffness of the beam,

which is related to the resonant frequency and the nonlinearity of its dynamic behavior. With an analytical form of load-deflection relationship, design parameters can be tuned and optimized according to clearly defined design goals.

To obtain an analytical load-deflection relationship of the proposed double spiral beam design shown, a simplified model which keeps the curved beam feature but with relatively simple geometry is adopted. The simplified model consists of two 90° arc beams which form one S shaped beam with two ends clamped and a transvers load at the center, the top view is shown in Figure 3-9 (a).

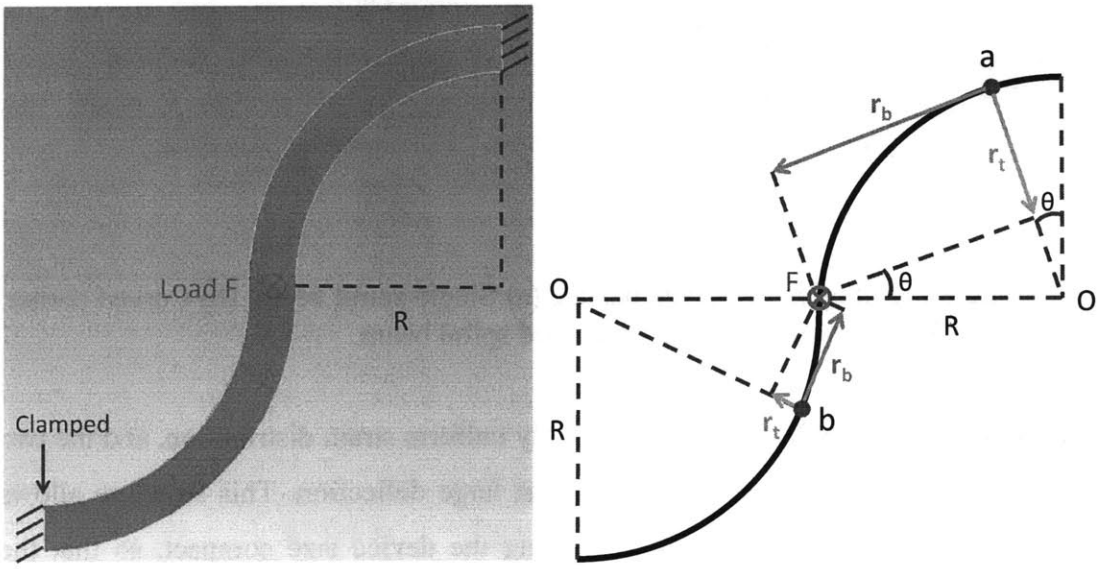

(a) (b)

Figure 3-9 S-beam. (a) Schematic of doubly clamped S-beam. (b) Geometries for the calculation of load-deflection characteristic.

From Figure 3-9 (b), it is obvious that the center transvers load generates varying moment and torque at each point on the beam, as illustrated by two different points *a* and *b*. Furthermore, the moments and torques reveal that the beam is bent and twisted, and strains due to bending and torsion exist simultaneously. Similar to the doubly clamped rectangle beam case, the two ends of this structure are also clamped; at large deflection,

we would also expect longitudinal stretching in the beam due to geometry compatibility requirement. Therefore, as analyzed above, the curved beam structure deforms with bending, torsion and stretching, which can be analyzed by using variational methods with the Principle of Virtual Work.

To proceed with variational method, we will use the superposition of linear elasticity – thinking of the total deformation consists of three virtual steps. The first step is bending of an uncurving beam that has the same length as the S-beam with one end free, so that there is no axial stress in the neutral plane. The second step is to fix the free end to the original position, so that a stretching is induced. The final step is to curve the beam and to twist it to the final shape. In the third step, we only consider the centerline of the neutral plane, which is not affected by the stretching introduced by torsion. By calculating the energy of bending, stretching and torsion separately and adding them together, we know the total stored energy in the structure. Minimizing the difference between stored energy and the work done by the load, we will find out the load-deflection relationship.

First, let us assume a trial function for the deflection field. If w is the vertical deflection, s is the position along the beam, and $s=0$ at the center of the S-beam, R is the radius of the arc beam, and n is the portion of the arc in a whole circle, then for a doubly clamped beam, the boundary conditions are:

$w(s)=0$ at $s=-2n\pi R$ and $s=2n\pi R$,

We may use a cosine which satisfies the boundary conditions as the trial function of the vertical deflection:

$$\hat{w}=\frac{\delta}{2}\left(1+\cos\frac{s}{2nR}\right) \qquad \text{Eq. 3.12}$$

With this vertical deflection field, we cannot find the energy of the uniform stretching strain by calculating the change in length, since torsion also contributes to the vertical deflection, and that portion of deflection does not result in a change in length of the centerline of the beam (neglecting the non-uniform stretching due to torsion). Therefore, we may assume another trial function for the vertical deflection due to torsion. Since the deflection due to torsion has the similar shape as the total deflection – zero at both ends and maximum at the center, we may assume the trial function is,

$$\hat{w}_t = \frac{\delta_t}{2}\left(1+\cos\frac{s}{2nR}\right) \qquad \text{Eq. 3.13}$$

So the deflection due to bending and stretching is,

$$\hat{w}_{bs} = \hat{w} - \hat{w}_t = \frac{\delta - \delta_t}{2}\left(1+\cos\frac{s}{2nR}\right) \qquad \text{Eq. 3.14}$$

Clearly, under these assumptions, the deflection due to bending and stretching and deflection due to torsion are proportions of the total deflection, for computation simplicity, we may rewrite Eq. 3.13 and Eq. 3.14 as a ratio multiply the total deflection,

$$\hat{w}_{bs} = \frac{x\delta}{2}\left(1+\cos\frac{s}{2nR}\right) \qquad \text{Eq. 3.15}$$

$$\hat{w}_t = \frac{(1-x)\delta}{2}\left(1+\cos\frac{s}{2nR}\right) \qquad \text{Eq. 3.16}$$

where $0 < x < 1$, so that the sum of the above two deflections is the total deflection.

The strain due to bending and stretching can be obtained from the deflection field,

$$\varepsilon_b = -z\frac{d^2\hat{w}_{bs}}{ds^2} \qquad \text{Eq. 3.17}$$

$$\varepsilon_s = \frac{1}{4n\pi R}\int_{-2n\pi R}^{2n\pi R}\frac{1}{2}\left(\frac{d\hat{w}_{bs}}{ds}\right)^2 ds \qquad \text{Eq. 3.18}$$

Hence, the bending strain energy and stretching strain energy are,

$$U_b = \frac{EW}{2}\int_{-H/2}^{H/2}\int_{-2n\pi R}^{2n\pi R}\varepsilon_b^2 ds dz = \frac{EWH^3\pi}{768n^3R^3}x^2\delta^2 \qquad \text{Eq. 3.19}$$

$$U_s = \frac{EW}{2}\int_{-H/2}^{H/2}\int_{-2n\pi R}^{2n\pi R}\varepsilon_s^2 ds dz = \frac{EWH\pi}{2048n^3R^3}x^4\delta^4 \qquad \text{Eq. 3.20}$$

where E is the Young's modulus, W and H are the width and thickness of the beam respectively, z is the vertical axis.

The strain energy in one arc beam (half of the S-beam) created by torsion is,

$$\frac{1}{2}U_t = \int_0^{2n\pi}\frac{T^2}{2GI_p}Rd\theta \qquad \text{Eq. 3.21}$$

where T is the torque generated by the load force, G is the shear modulus, I_p is the polar moment of inertia. From Figure 3-9 (b), the lever arm $r_t = R(1-\cos\theta)$. To calculate the torque, we view the S-beam as two parallel arc beams, so that the force on one arc beam is half the total force. Therefore, the torque is

$$T = \frac{1}{2}FR(1-\cos\theta) \qquad \text{Eq. 3.22}$$

Substituting the torque and evaluating the integral, we then obtain half of the torsion energy,

$$\frac{1}{2}U_t = \frac{F^2R^3}{32GI_p}\left[6n\pi - 8\sin(n\pi) + \sin(2n\pi)\right] \qquad \text{Eq. 3.23}$$

By Castigliano's theorem, the deflection due to torsion is,

$$\delta_t = \frac{\partial(1/2U_t)}{\partial(1/2F)} = \frac{FR^3}{8GI_p}\left[6n\pi - 8\sin(n\pi) + \sin(2n\pi)\right] \qquad \text{Eq. 3.24}$$

Substituting Eq. 3.24 into Eq. 3.23 to get the energy as a function of deflection,

$$U_t = \frac{4GI_p}{\left[6n\pi - 8\sin(n\pi) + \sin(2n\pi)\right]R^3}(1-x)^2\delta^2 \qquad \text{Eq. 3.25}$$

The total strain energy is,

$$U_{total} = U_b + U_s + U_t = \frac{EWH^3\pi}{768n^3R^3}x^2\delta^2 + \frac{EWH\pi}{2048n^3R^3}x^4\delta^4 + \frac{4GI_p}{\left[6n\pi - 8\sin(n\pi) + \sin(2n\pi)\right]R^3}(1-x)^2\delta^2$$

Eq. 3.26

The total potential energy is,

$$U = U_{total} - F\delta \qquad \text{Eq. 3.27}$$

Taking the derivative with respect to δ and setting the result to zero,

$$\frac{\partial U}{\partial \delta} = 0 \qquad \text{Eq. 3.28}$$

yields the load-deflection characteristic for the S-beam:

$$F = \left[\left(\frac{\pi}{384}\right)\frac{EWH^3}{n^3R^3}x^2 + \frac{8GI_p}{\left[6n\pi - 8\sin(n\pi) + \sin(2n\pi)\right]R^3}(1-x)^2\right]\delta + \left[\left(\frac{\pi}{512}\right)\frac{EWH}{n^3R^3}x^4\right]\delta^3 \qquad \text{Eq. 3.29}$$

To determine the only unknown variable x in the load-deflection equation, we still need to insert one pair of force and deflection of the structure, which can be obtained from numerical solution, to solve the equation.

A comparison of the analytical and numerical solution can be illustrated by the following example. For a S-beam with the dimensions and material properties shown in Table 3-2,

Table 3-2 Parameters of S-beam for comparison of analytical and numerical results.

Parameters	R (m)	W (m)	H(m)	n	E (Pa)	ν
Values	0.02	0.001	0.0001	1/4	2e11	0.3

The shear modulus, polar moment of inertia and moment of inertia can then be obtained. By plugging in one pair of force deflection of the beam, the ratio x is found to be 0.337769 for this structure. Plotting the analytical load-deflection function known x, and 10 points of numerical solutions from ANSYS, the comparison is shown in Figure 3-10.

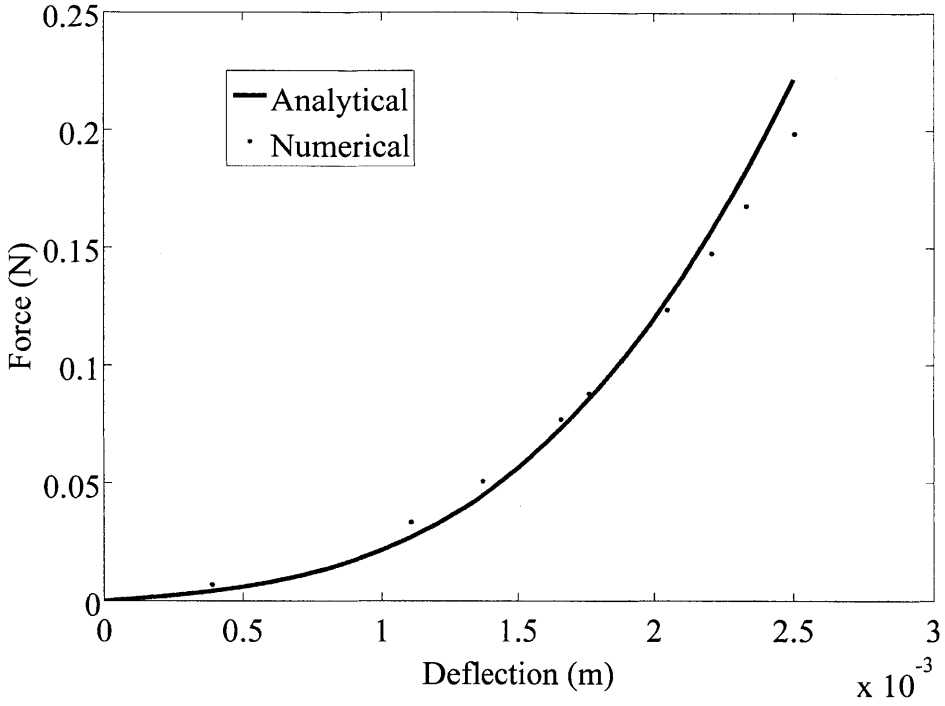

Figure 3-10 Comparison of analytical and numerical results of load-deflection relationship of S-beam.

Although the S-beam shows some degree of nonlinearity, as the number of revolutions increase, the total length of the spiral beam increases significantly. Numerical simulations were made for spiral beams to investigate the relationship between design parameters and nonlinearity of the system. Four spiral beams (Fig. 3-11) with different design parameters were used for making simulations. The parameters are shown in Table 3-3. The force-deflection relationship of the four spiral beams were normalized for comparison, the results are displayed in Fig. 3-12. The results show little nonlinearity for all of these beams, which means the bandwidth is limited. Therefore, this design was not adopted either.

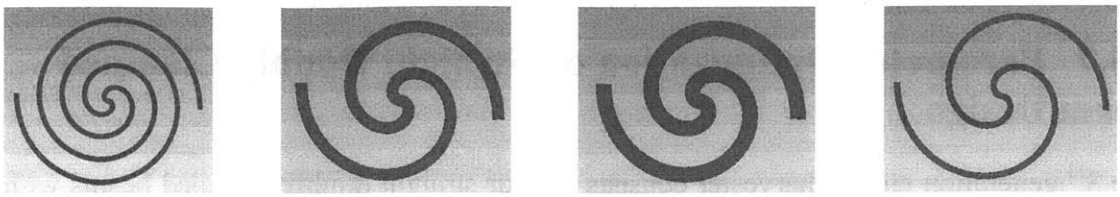

Figure 3-11 Four spiral beams with different design parameters.

Table 3-3 Parameters of four spiral beams.

Spiral #	Pitch	Revolution	Width	Thickness
1	0.0005	2	0.00006	3.00E-06
2	0.0005	1	0.00006	3.00E-06
3	0.0005	1	0.00008	3.00E-06
4	0.001	1	0.00006	3.00E-06

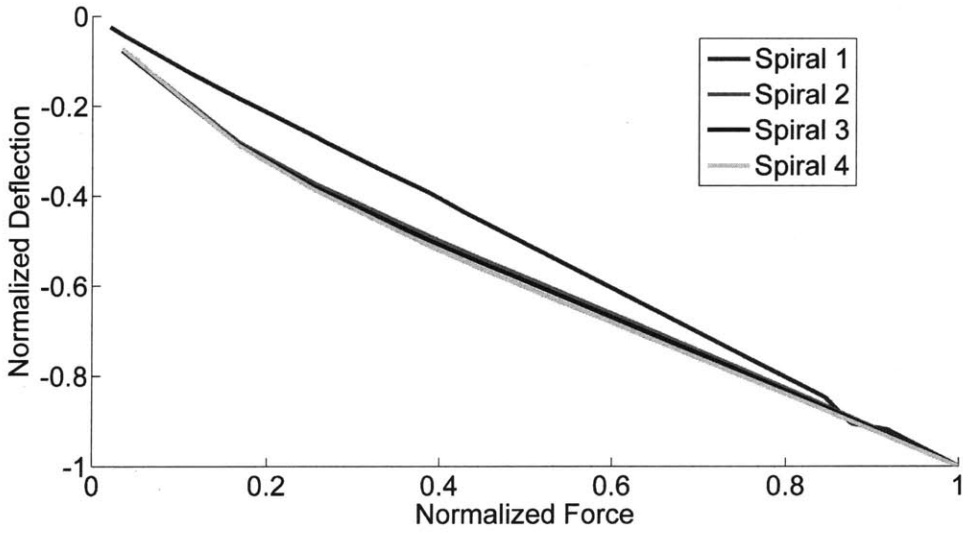

Figure 3-12 Normalized force-deflection for four different spiral beams.

3.3.7 Parameter Optimization on Straight Doubly Clamped Beam Design

The 3rd generation energy harvester consists of four straight doubly clamped beams with an external proof mass. The experiments showed the resonance frequency to be higher ($\sim 10^3$ Hz) than designed value ($\sim 10^2$ Hz). However, from the earlier statics and dynamics analysis, the resonance frequency depends on stiffness and proof mass, and the stiffness of a doubly clamped beam is a function of material properties and beam dimensions. An optimization on these design parameters may bring down the resonance frequency and enhance the bandwidth at the same time. Detailed analysis and results are presented in next section.

3.4 Proposed Design: Optimized Doubly Clamped Beam Resonator

3.4.1 Design Parameters

For a straight doubly clamped beam resonator as the 3rd generation PMPG, the design parameters include:

- **Elastic modulus**
- **Residual stress**
- **Length**
- **Width**
- **Thickness**
- **Proof Mass**

among which, material of the beam determines the elastic modulus and residual stress, length, width and thickness are the dimensions of the beam. So the design parameters can be categorized in 3 groups:

- **Material**
- **Dimensions**
- **Proof mass**

It should be noted that the excitation amplitude and frequency also affect the performance of the energy harvester, but they are input parameters and not design parameters. Our design should be made at fixed desirable input parameters, which are 0.5g excitation at ~100 Hz.

The design parameter optimization can be one way to realize the design goals, which are,

- **Compact design**
- **High output voltage**
- **High power density**
- **Low operating frequency**
- **Wide bandwidth**
- **Low excitation amplitude**

The dimensions can be constrained at the beginning so that the compactness can be guaranteed. High output voltage and power density are related to the piezoelectric material, electrode configuration and strain level. Both of the goals have been achieved by 3rd generation design. The new design will inherit these properties without much difficulty. Low operating frequency and low excitation level are new design goals and can be challenging at MEMS scale. Together with wide bandwidth, which is coupled with resonance frequency, last three design goals will be the focus of the parameter optimization.

The knowledge on the relations between design parameters and outputs is necessary for optimization. Although it seems straightforward how the parameters affect the statics by

analyzing the load-deflection characteristic, the it is not intuitive to know the effects of the design parameters on dynamics. Part of the reason is due to jump phenomenon. Jump phenomenon arise from the multi-valuedness of the response curves due to the nonlinearity [63]. To characterize the dynamic response of a nonlinear *Duffing* mode resonator, we will use the jump-down and jump up frequencies. These frequencies have been estimated in [64] by using harmonic balance method (HBM). The jump-up frequency is estimated as,

$$\Omega_{up} \approx \left(1 \pm \left(\frac{3}{2}\right)^{4/3} |\alpha|^{1/3}\right)^{1/2} \qquad \text{Eq. 3.30}$$

and the jump-down frequency is estimated as,

$$\Omega_{down} \approx \frac{1}{2^{1/2}}\left(1+\left(1+\frac{3\alpha}{4\zeta^2}\right)^{1/2}\right)^{1/2} \qquad \text{Eq. 3.31}$$

where

$$\alpha = \frac{k_n x_0^2}{k_l} \qquad \text{Eq. 3.32}$$

$$x_0 = F / k_l \,|_{k_3=0,\omega=0} \qquad \text{Eq. 3.33}$$

$$\zeta = \frac{c}{2m\omega_n} \qquad \text{Eq. 3.34}$$

c is the total damping coefficient, ω_n is the resonance frequency of the system in linear regime ($k_n = 0$).

Since for a nonlinear resonator, the resonance frequency is not a fixed value as a linear resonator has, but varying depending on the deflection, we cannot use a single resonance frequency to characterize its operating frequency. The varying resonance frequency

together with jump down makes it not straightforward to get the bandwidth either. To characterize the dynamic response of the *Duffing* mode nonlinear resonator, we may define a bandwidth indicator, which is the difference between the jump-down frequency and jump-up frequency:

$$\Delta f = f_d - f_u \qquad \text{Eq. 3.35}$$

and an average of the jump-up and jump-down frequencies frequency to be an operating frequency indicator:

$$f_{mid} = (f_d + f_u)/2 \qquad \text{Eq. 3.36}$$

The relations between each design parameter and design goals – bandwidth and operating frequency can then obtained, and used as the guidelines for parameter design. For analysis simplicity, we will consider a monolayer beam here. One design parameter varies while holding other parameters fixed for all the design parameters has been used to find the effects of design parameters on performance. Reasonable beam dimensions and other parameters are chosen for illustration purpose. The chosen fixed value and design range are shown in Table 3-4.

Table 3-4 Values of design parameters for illustrating the relationships of design parameters and design goals.

	Thickness (μm)	Width (mm)	Length (mm)	Young's modulus (GPa)	Residual stress (MPa)	Proof mass (g)
Fixed value	5	5	6	185	10	1
Range	2 ~ 10	1 ~ 10	5 ~ 15	100 ~ 200	0 ~ 100	0.1 ~ 1

Thickness

From Figure 3-13, when thickness of the beam increases, the difference between jump-up and jump-down frequencies decreases, which indicates the bandwidth gets narrower. This is also consistent with the observation of load-deflection characteristic. We may define the nonlinearity of the static response by the ratio of nonlinear stiffness and linear stiffness. If assuming zero residual stress and divide the nonlinear stiffness by linear stiffness, we have thickness squared in the denominator. The increase in thickness decreases that ratio and the nonlinearity is weaker. Figure 3-13 also shows that the operating frequency increases with larger thickness. That may be concluded from the load-deflection equation that the thickness is in the numerators of both linear and nonlinear stiffness', the increase in thickness makes the beam stiffer and resonates at higher frequency. Both results suggest that a smaller thickness is better for the design, since our design goals are a wide bandwidth and low operating frequency. However, thickness cannot be minimized limitlessly but is bounded by the value of zero, the enhancement of bandwidth and operating frequency by tuning thickness is finite and must be subjected to physical constraints.

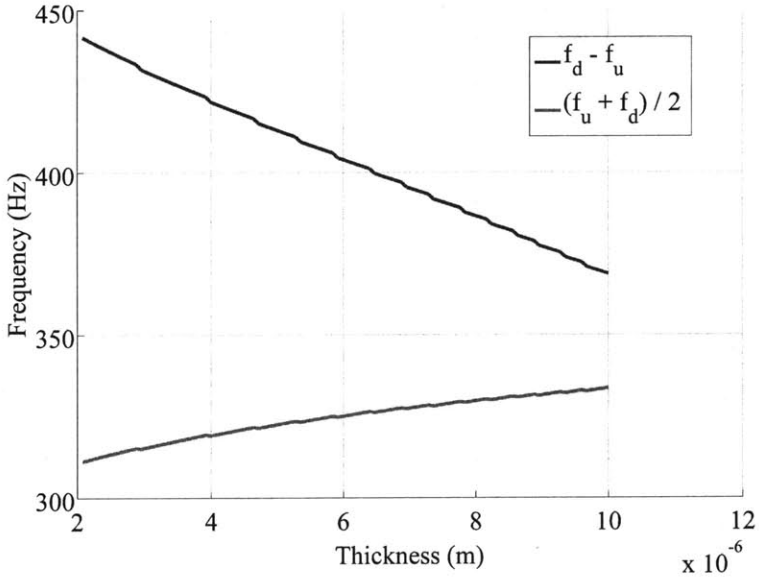

Figure 3-13 Bandwidth indicator and operating frequency indicator change with the thickness of the beam.

Width

Just as thickness, a larger width results in a narrower bandwidth and higher operating frequency (Figure 3-14). Hence, a narrower beam is more desirable to meet the design goals. Although small width is beneficial, it is also bounded by zero and must satisfy constraints, such as it must be much larger than the thickness to maintain stiffness in in-plane directions and also prevent twisting.

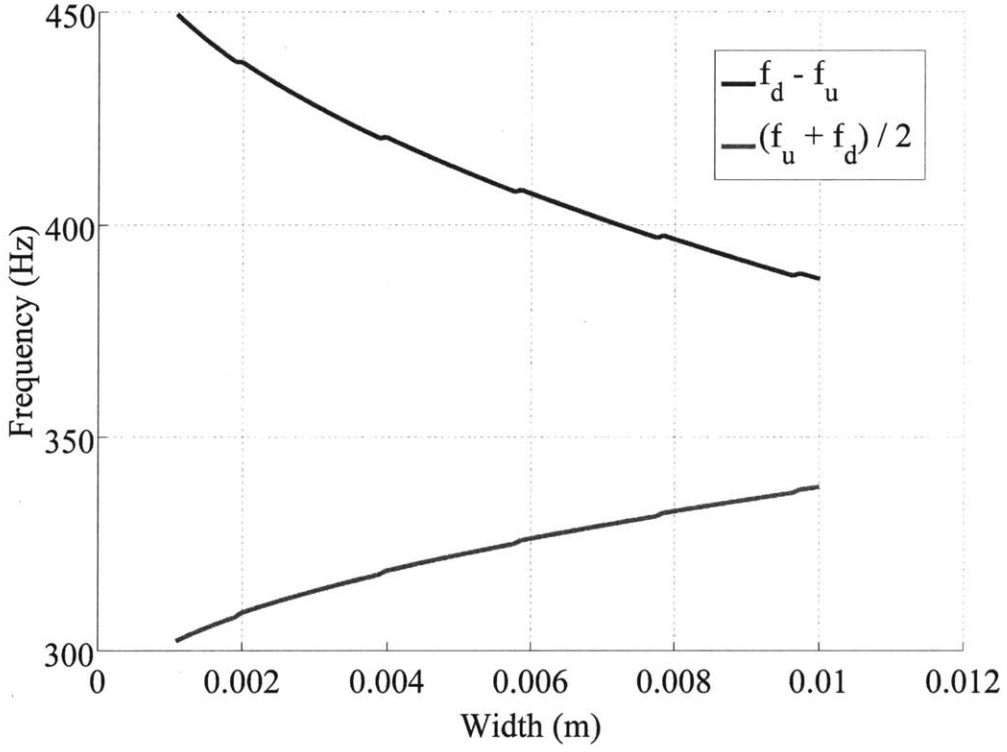

Figure 3-14 Bandwidth indicator and operating frequency indicator change with the width of the beam.

Length

How to choose the length is not obvious. Increasing length leads to lower operating frequency which is desirable but the bandwidth also decreases significantly. This trade-off requires careful design to balance the bandwidth and frequency. Moreover, the compactness requirement on the design limit the length of the straight doubly clamped beam to ~15 mm.

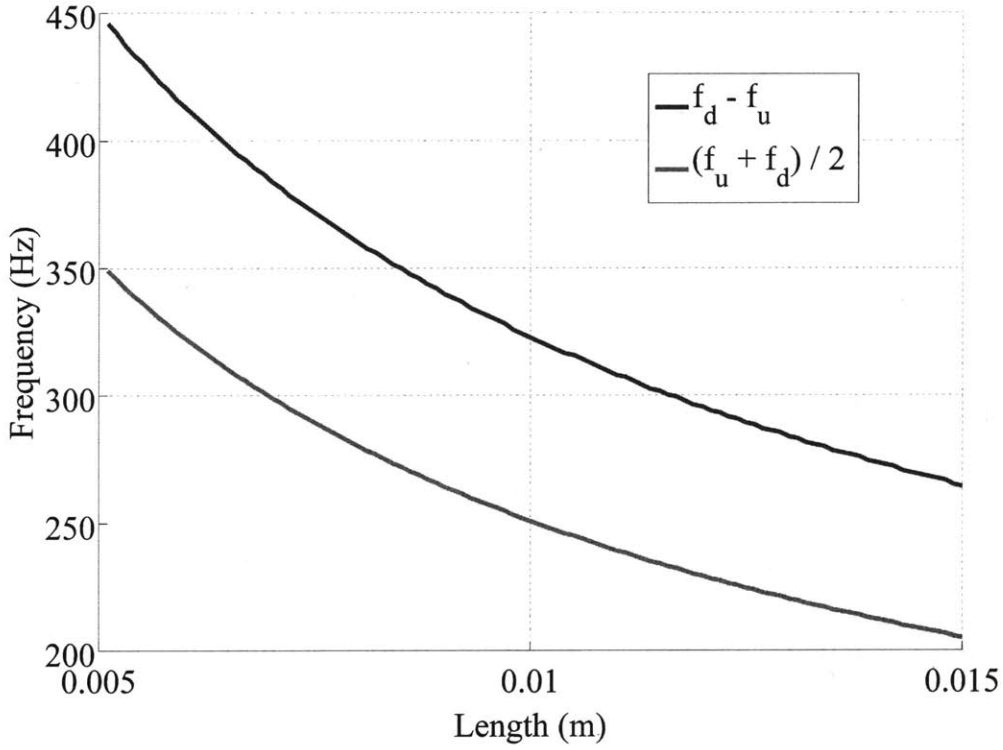

Figure 3-15 Bandwidth indicator and operating frequency indicator change with the length of the beam.

Young's Modulus

On contrast to length, a larger Young's modulus results in a wider bandwidth and higher operating frequencies. Balancing between bandwidth and operating frequency is needed to design Young's modulus and choose the right materials, but as what will be analyzed later, material selection may be constrained by other factors and the optimization of Young's modulus may not be a feasible way for design.

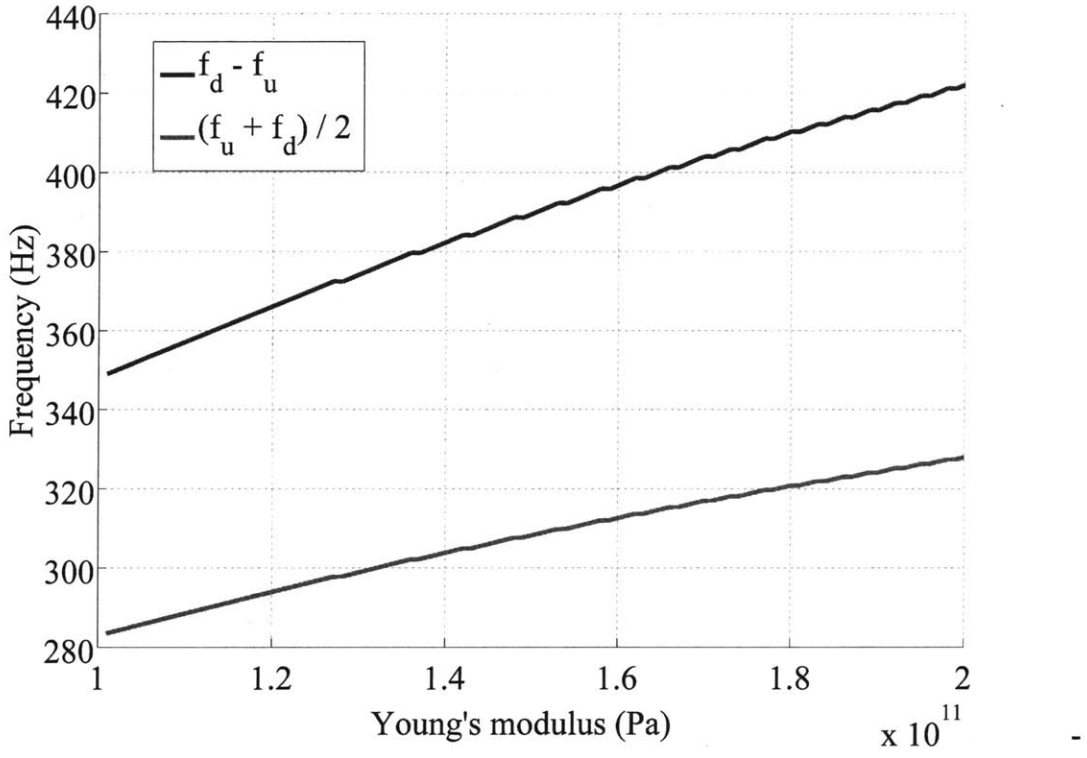

Figure 3-16 Bandwidth indicator and operating frequency indicator change with the Young's modulus of the beam.

Residual Stress

Figure 3-17 shows that higher residual stress dramatically decreases the bandwidth. It seems a little residual stress decreases the operating frequency, but the examination of jump frequencies versus residual stress (Figure 3-18) reveals that it is the drastic drop of jump down frequency makes the average of jump frequencies decline a little. The actual operating frequency is not really lower but just confined by lower upper bound. Residual stress is inevitable and has no positive effects on the performance of the device, and may even cause potential problems such as buckling. Therefore, it is obvious that residual stress should be minimized. In practice, this is normally done by good stress control – layers with opposite residual stress with carefully designed thickness' to compensate other active layers' residual stress.

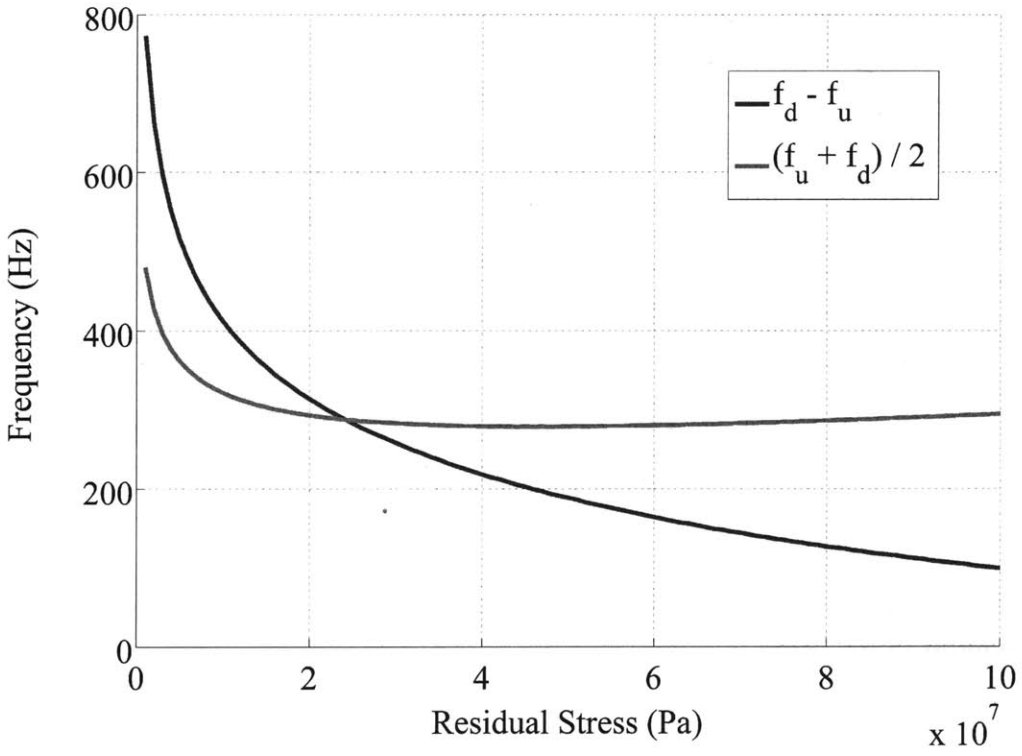

Figure 3-17 Bandwidth indicator and operating frequency indicator change with the residual stress in the beam.

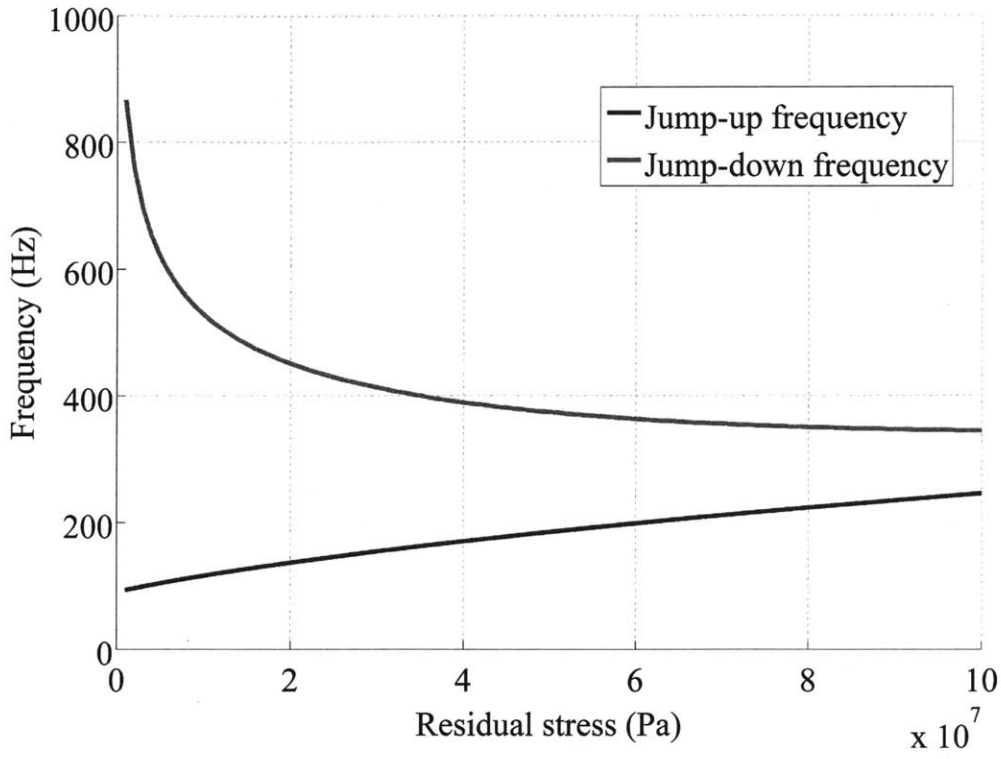

Figure 3-18 Jump-up and jump-down frequencies change with the residual stress in the beam.

Proof Mass

A heavier proof mass enhances the nonlinearity and lower the operating frequency as proved by Figure 3-19. External proof mass may be adopted to decouple the design of beam dimensions and proof mass and increase the ability to using a larger mass. But it also should be noted that the increase in bandwidth and decrease in operating frequency are asymptotic, further increasing mass would not have a big effect.

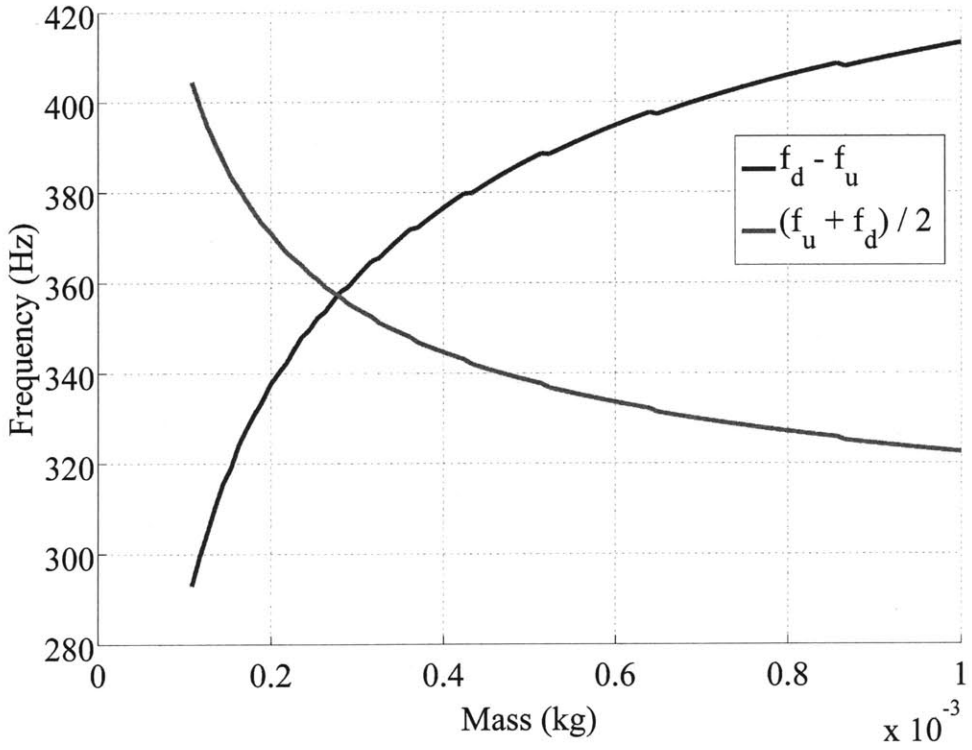

Figure 3-19 Bandwidth indicator and operating frequency indicator change with the proof mass.

Summary on Relations Between Design Parameters and Design Goals

The relations between design parameters and design goals presented above give a designer more insights and can be useful when design. The real situations will be more complicated and will be discussed in following sections, but a qualitative guideline obtained will help to make strategies to design. Table 3-5 summarizes the effects of these design parameters on bandwidth and operating frequency as investigated and discussed before. The black arrows in the last row denote increasing (pointing right) or decreasing (pointing left) the corresponding design parameter in the first row and same column. The other arrows show the corresponding change in bandwidth and operating frequency. Pointing up means increase and down means decrease. The color green and red of the arrows denote the change better meet the design goals or contradict them respectively.

Table 3-5 Summary of relationships between design parameters and design goals.

	Thickness	Width	Length		Young's modulus		Residual stress	Proof mass
Bandwidth	↑	↑	↑	↓	↓	↑	↑	↑
Operating frequency	↓	↓	↑	↓	↓	↑	↓	↓
Design	←	←	←	→	←	→	←	→

3.4.2 Design Framework

The previous section reports six different design parameters and their relations to design goals. Determining these design parameters simultaneously can be difficult. More importantly, some design parameters may be subjected to physical constraints so that they cannot be freely designed. More analysis will reveal insights that would simplify the design process and help to make design decisions.

In spite of the design parameter optimization, constraints are crucial to realize a design in physical world. For the implementation of an MEMS energy harvester, the constraints may come from the functional requirements, such as PZT as the active layer must be used, despite that it has a high tensile stress that is not desirable, or a layer of ZrO_2 must be deposited under PZT as the diffusion barrier for d_{33} mode. Constraints may also be the limitation of material selection. There are materials that are compatible to micro fabrication, and design should be made based on these available materials, such as silicon, silicon oxide, silicon nitride, some metals etc. Another important constraint is the residual stress balancing discussed before. The total residual stress should be minimized and the stress distribution with respect to neutral axis should be symmetrical. All these constraints should be considered first so that the design is feasible and can be

implemented. It is not hard to find that these constraints are all about the beam composition, therefore, it will be discussed in detail in the following section.

Beam composition design will include the thickness, Young's modulus, residual stress, and one more design parameter that we did not discussed before but exists for composite beams, which is the sequence of the layers. Three design parameters left are the width, length and proof mass. We may imagine a wide beam can be split into narrower beams, each one of them has the same proportion of proof mass, then the response of all these narrow beams should be the same to the original beam. This is proved by Figure 3-20, where when the width of the beam increases, the mass also increases proportionally, then the bandwidth and operating frequency remain constants. Therefore, we can define mass per unit width as one design parameter, and the parameters that we can actively designed are only two: length and mass per width.

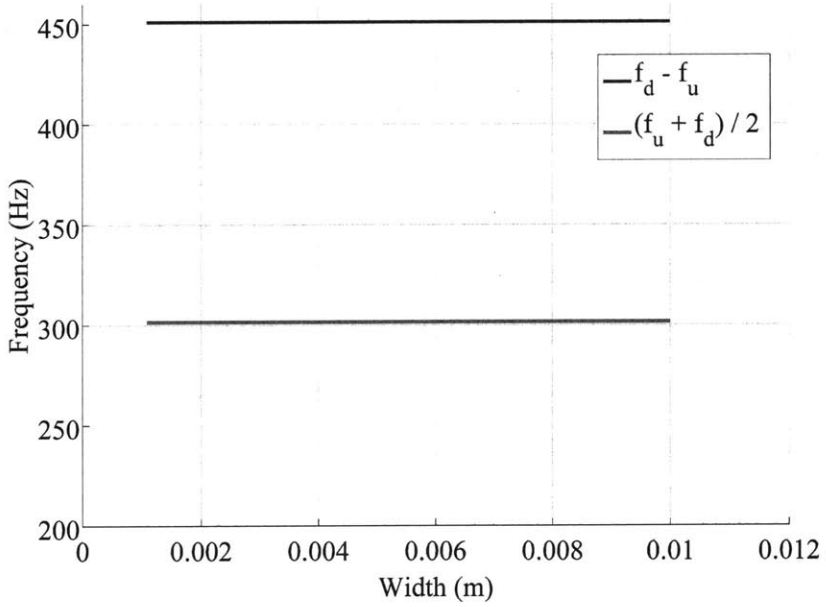

Figure 3-20 Bandwidth indicator and operating frequency indicator remain constant with varying width and mass compensation.

As analyzed in previous section, the design of length can be tricky, a balance between bandwidth and operating frequency must be made, while a larger mass is always good for both the design goals. These two parameters may be design at the final stage to fine tuning the performance of the energy harvester. A systematic and practical way to design a doubly clamped straight beam based energy harvester can be devised now, and is presented by the diagram in Figure 3-21.

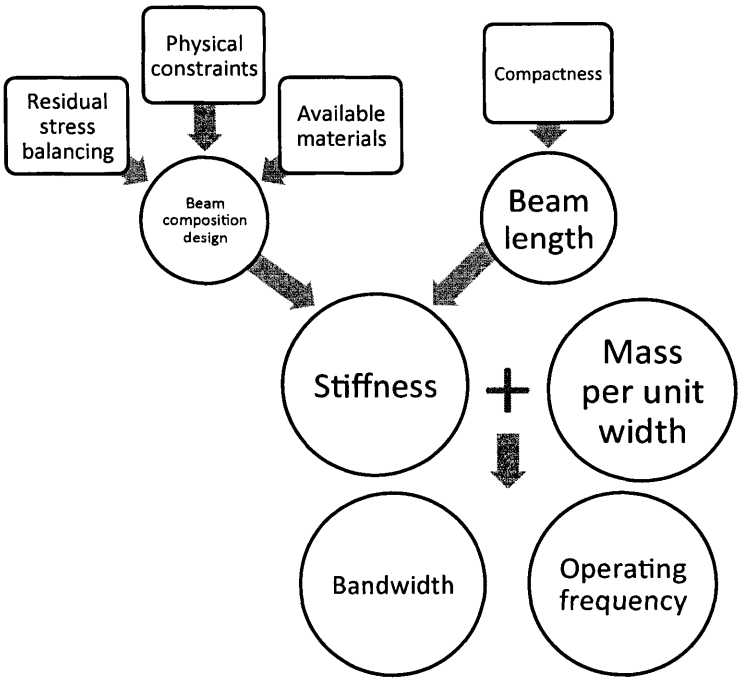

Figure 3-21 Diagram illustrating the design framework.

3.4.3 Beam Composition

Not as straightforward as designing a beam with one material, the design of a composite beam – material selection, thickness of each layer and the sequence of different layers, altogether determines the stored mechanical energy in the structure for conversion, the dynamic behavior and mechanical robustness. This section describes the effects of beam

composition on device performance, and presents the analysis and design of beam composition for low-frequency, low-g energy harvester.

The Effects of Beam Composition on Device Performance

The mechanical energy stored in the PZT layer due to the deformation is the energy available for converting to electrical energy through piezoelectric effect, and should be maximized to increase the output electrical power under the condition that the strain is within the strain limits 0.1% ~ 0.2%. At a specific ambient vibration level, the total stiffness of the composite beam determines the deformation, hence the strain energy in PZT layer. For example, if the structural layer in the composite beam has a high Young's modulus and a large thickness compared to other layers, it will dominate the beam stiffness and lead to small deformation, so that the strain of PZT layer is far less than its strain limit, and produce limited output power.

The resonance frequency of a doubly clamped beam resonator is proportional to the square root of its stiffness and is inversely proportional to proof mass. Jump frequencies also depend on the linear and nonlinear stiffness'; parameters such as the Young's modulus, thickness and residual stress and their effects on bandwidth and operating frequencies have been explored.

Residual stress is another factor which is closely related to beam composition and has a significant impact on device performance, and should be dealt with great care in design phase and through out the whole fabrication process. As the experiments for making the 3rd generation devices showed, a high residual stress increased the stiffness of the composite beam so that the resonance frequency is much higher than designed. Analytical analysis also shows it decreases the bandwidth significantly. Residual stress not only tremendously affects the dynamics, but may also cause mechanical failures. A large compressive residual stress bends a doubly clamped beam and makes its

equilibrium position not straight, which is called buckling. Serious mechanical failures due to buckling appeared in previous experiments.

Considerations on the Design of Composite Beams

From a design perspective, we integrated our design goals with the above insights, and developed a strategy to realize an optimal design of beam composition. One of the design goals is to make the strain in PZT layer to reach 0.1% to 0.2%, which is the strain limit of PZT, so that the maximum energy conversion is possible. The stiffness of the beam should then be small enough so the beam deforms a considerable amount. Another important goal is that the beam resonates at frequencies as low as possible to be close to the frequencies of ambient vibrations to absorb maximum mechanical energy from environment. This requires stiffness to be as small as possible and proof mass to be as large as possible. Nonzero residual stress increases the stiffness which is undesirable, and even unsymmetrical residual stress distribution cause curl, buckling and even mechanical failures, and therefore residual stress should be carefully balanced out.

From the analysis of design goals, it becomes clear that the beam composition should be designed such that its stiffness is small and residual stress is minimized and symmetric with respect to neutral axis. The stiffness of a beam is a function of the elastic properties and dimensions of the composites, therefore it depends on material selection and thickness assignment. Due to the intrinsic high tensile stress in the seed layer ZrO2 and active layer PZT, residual stress must be balanced with other layers with compressive stress. The composition is also subjected to functional constraints, such as the specific thickness and material for diffusion barrier, active layer and strength of structural layer. To make a sound beam design, we use the strategy to meet the functionality requirements first by choosing the right materials and thicknesses, and then adding additional layers to balance the residual stress and optimize the design parameters. An algorithm and MATLAB program for calculating the optimal thicknesses of the balancing layers to get

a minimized residual stress and symmetric distribution has been developed and is presented in section and Appendix respectively.

Load-Deflection Characteristic of Doubly Clamped Composite Beam

The load-deflection equation gives the stiffness of a doubly clamped beam and can be used for characterization and design. Eq. 2.8 is the load-deflection characteristic of a single layer beam, but a real fabricated energy harvester consists of several different layers. A more general load-deflection expression for a composite beam is necessary to make accurate prediction on beam stiffness and dynamic response. Variational methods will be used to find the load-deflection expression for a composite beam at large deflection. Assume the vertical deflection field can be described by a trial function:

$$\hat{w} = \frac{\delta}{2}\left(1+\cos\frac{2\pi x}{L}\right) \qquad \text{Eq. 3.37}$$

The bending strain is,

$$\varepsilon_b = -z\frac{d^2\hat{w}}{dx^2} \qquad \text{Eq. 3.38}$$

and the stretching strain is

$$\varepsilon_s = \frac{1}{L}\int_{-L/2}^{L/2}\frac{1}{2}\left(\frac{d\hat{w}}{ds}\right)^2 ds \qquad \text{Eq. 3.39}$$

Then the sum of the strain energy of each layer is,

$$U_{strain}=\frac{W}{2}\left[E_1\int_{h}^{h+h_1}\int_{-L/2}^{L/2}\left(\varepsilon_b^2+\varepsilon_s^2\right)dx\,dz+E_2\int_{h+h_1}^{h+h_1+h_2}\int_{-L/2}^{L/2}\left(\varepsilon_b^2+\varepsilon_s^2\right)dx\,dz+\cdots+E_n\int_{h+\cdots+h_{n-1}}^{h+\cdots+h_n}\int_{-L/2}^{L/2}\left(\varepsilon_b^2+\varepsilon_s^2\right)dx\,dz\right]$$

Eq. 3.40

Or in a more compact form,

$$U_{strain}=\frac{W}{2}\sum_{i=1}^{n}E_i\int_{h+\sum_{j=1}^{i-1}h_j}^{h+\sum_{j=1}^{i}h_j}\int_{-L/2}^{L/2}\left(\varepsilon_b^2+\varepsilon_s^2\right)dx\,dz \qquad \text{Eq. 3.41}$$

Substituting Eq. 3.38 and Eq. 3.39, and evaluating the integral yields the total strain energy due to bending and stretching,

$$U_{strain}=\frac{W\pi^4\delta^2}{3L^3}\sum_{i=1}^{n}E_i\left(z^3\right)_{h+\sum_{j=1}^{i-1}h_j}^{h+\sum_{j=1}^{i}h_j}+\frac{W\pi^4\delta^4}{32L^3}\sum_{i=1}^{n}E_i\left(z\right)_{h+\sum_{j=1}^{i-1}h_j}^{h+\sum_{j=1}^{i}h_j} \qquad \text{Eq. 3.42}$$

Then the total potential energy is obtained,

$$U=\frac{W\pi^4\delta^2}{3L^3}\sum_{i=1}^{n}E_i\left(z^3\right)_{h+\sum_{j=1}^{i-1}h_j}^{h+\sum_{j=1}^{i}h_j}+\frac{W\pi^4\delta^4}{32L^3}\sum_{i=1}^{n}E_i\left(z\right)_{h+\sum_{j=1}^{i-1}h_j}^{h+\sum_{j=1}^{i}h_j}-F\delta \qquad \text{Eq. 3.43}$$

Taking derivative with respect to δ and setting the result to zero yields the *load-deflection characteristic* for a general composite beam

$$F=\left(\frac{2\pi^4}{3}\right)\left[\frac{W}{L^3}\sum_{i=1}^{n}E_i\left(z^3\right)_{h+\sum_{j=1}^{i-1}h_j}^{h+\sum_{j=1}^{i}h_j}\right]\delta+\left(\frac{\pi^4}{8}\right)\left[\frac{W}{L^3}\sum_{i=1}^{n}E_i\left(z\right)_{h+\sum_{j=1}^{i-1}h_j}^{h+\sum_{j=1}^{i}h_j}\right]\delta^3 \qquad \text{Eq. 3.44}$$

With the consideration of residual stress in each layer, the load-deflection can be changed, by adding the residual stress to the total strain energy of the composite beam as a starting point, the contribution of residual stress to the total strain energy

$$\left(\frac{\pi^2}{4}\right)\left[\frac{W}{L}\sum_{i=1}^{n}\sigma_i(z)_{h+\sum_{j=1}^{i-1}h_j}^{h+\sum_{j=1}^{i}h_j}\right]\delta^2 \qquad \text{Eq. 3.45}$$

The modified load-deflection equation then becomes:

$$F=\left\{\left(\frac{2\pi^4}{3}\right)\left[\frac{W}{L^3}\sum_{i=1}^{n}E_i\left(z^3\right)_{h+\sum_{j=1}^{i-1}h_j}^{h+\sum_{j=1}^{i}h_j}\right]+\left(\frac{\pi^2}{2}\right)\left[\frac{W}{L}\sum_{i=1}^{n}\sigma_i(z)_{h+\sum_{j=1}^{i-1}h_j}^{h+\sum_{j=1}^{i}h_j}\right]\right\}\delta+\left(\frac{\pi^4}{8}\right)\left[\frac{W}{L^3}\sum_{i=1}^{n}E_i(z)_{h+\sum_{j=1}^{i-1}h_j}^{h+\sum_{j=1}^{i}h_j}\right]\delta^3$$

Eq. 3.46

Residual Stress Balancing

Assuming a general n-layer beam with each layer having specific material properties and residual stress as shown in Figure 3-22,

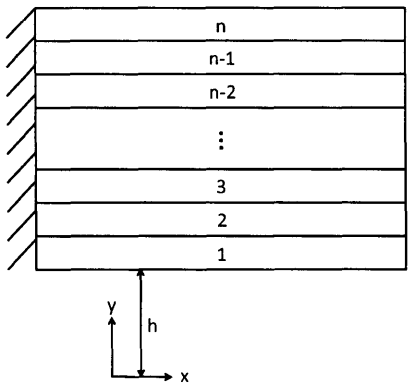

Figure 3-22 Schematic of multilayer beam structure.

We index each layer from bottom to top by *1* to *n*, the material properties of *i-th* layer are: Young's modulus E_i, Poisson's ratio v_i, thickness T_i, residual stress σ_i. We need to

find out the neutral axis of the composite beam first. By setting the first moment of the cross section about its neutral axis to zero (assuming the distance from the x-axis to the bottom of the structure is h):

$$E_1\left(h+h_1-\frac{1}{2}h_1\right)(w\cdot h_1)+E_2\left(h+h_1+h_2-\frac{1}{2}h_2\right)(w\cdot h_2)+\cdots+E_n\left(h+h_1+\cdots h_n-\frac{1}{2}h_n\right)(w\cdot h_n)=0$$

Eq. 3.47

Or in a more compact form,

$$\sum_{i=1}^{n}E_i\left(h+\sum_{j=1}^{i}h_j-\frac{1}{2}h_i\right)=0 \qquad \text{Eq. 3.48}$$

There is only one unknown h in Eq. 3.48, and it can be solved.

For a composite structure, Young's modulus cannot be separated from geometry when considering bending, an effective EI product is to be used.

$$\tilde{E}I=\tilde{E}_1w\int_h^{h+h_1}z^2\,dz+\tilde{E}_2w\int_{h+h_1}^{h+h_1+h_2}z^2\,dz+\cdots+\tilde{E}_nw\int_{h+\cdots+h_{n-1}}^{h+\cdots+h_n}z^2\,dz$$

$$\tilde{E}I=\sum_{i=1}^{n}\tilde{E}_iw\int_{h+\sum_{j=1}^{i-1}h_j}^{h+\sum_{j=1}^{i}h_j}z^2\,dz \qquad \text{Eq. 3.49}$$

$$\tilde{E}I=\sum_{i=1}^{n}\tilde{E}_iw\left(\frac{z^3}{3}\right)_{h+\sum_{j=1}^{i-1}h_j}^{h+\sum_{j=1}^{i}h_j}$$

The total strain of the composite beam is,

$$\varepsilon=\frac{\sum_{i=1}^{n}\sigma_ih_i}{\sum_{i=1}^{n}E_ih_i} \qquad \text{Eq. 3.50}$$

Then, the residual stress after release but before bending in each layer can be calculated as,

$$\sigma_{k,release} = \sigma_k - \tilde{E}_k \varepsilon$$

$$\sigma_{k,release} = \frac{\sigma_k \sum_{i=1}^{n} \tilde{E}_i h_i - \tilde{E}_k \sum_{i=1}^{n} \sigma_i h_i}{\sum_{i=1}^{n} E_i h_i} \qquad \text{Eq. 3.51}$$

Total moment due to residual stress is,

$$M = \sum_{i=1}^{n} \sigma_{i,release} \left(\frac{z^2}{2} \right)_{h+\sum_{j=1}^{i-1} h_j}^{h+\sum_{j=1}^{i} h_j} \qquad \text{Eq. 3.52}$$

The radius of curvature is,

$$\rho = \frac{\tilde{E}I}{M} \qquad \text{Eq. 3.53}$$

3.4.4 Quantitative design

To make an optimized quantitative design, the design parameters should be determined according to the design framework that has been developed. The first step is to design the beam composition, which includes the material of each layer and their sequence. The composition of the 3rd generation design is illustrated in Fig. 3-23. It can be seen that each layer has its unique functionality and their sequence is almost fixed.

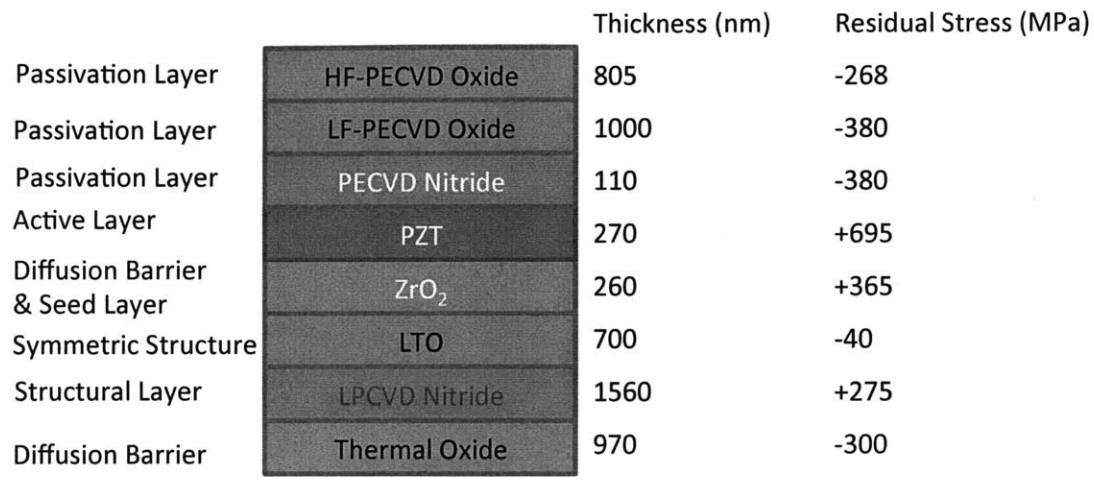

Figure 3-23 The beam composition of 3rd generation device.

In 3rd generation design, the structural material was selected to be silicon nitride, which has large fracture strain (3%). It was also proposed that silicon could be a good material for structural layer because of the perfection of the crystal, high structural strength and zero residual stress. Therefore, two different beam compositions are proposed for the new design, and their main difference is the structural materials.

The first proposed composition is similar to that of the 3rd generation design as shown in Fig. 3-24. Two main changes are the elimination of the LTO and the HF-PECVD oxide. LTO in 3rd generation design serves no important functions, and from residual stress balancing perspective, it has a low compressive stress and hence not as effective as thermal oxide to compensate the tensile stress in active layers. HF-PECVD oxide and LF-PECVD oxide both serve as the passivation layer, but the HF-PECVD oxide has a lower compressive residual stress than LF-PECVD oxide, therefore the two PECVD oxide layers can be replaced by a single LF-LPCVD oxide layer to reduce the total stiffness of the beam.

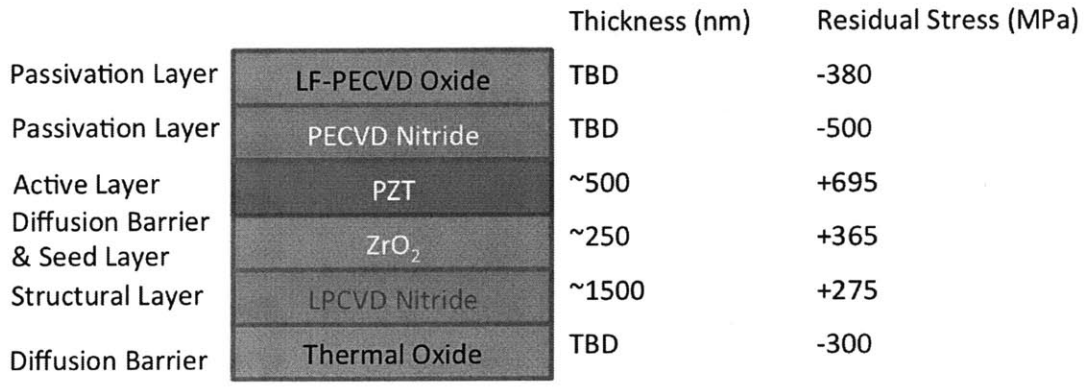

Figure 3-24 The proposed beam composition using silicon nitride as the structural layer.

Silicon is adopted as the structural layer in the second beam composition design. This design can be fabricated using SOI wafer. Fig. 3-25 shows the schematic of the beam composition. The difference lies in the bottom two layers, using SOI wafer the structural layer would be silicon oxide and single crystal silicon.

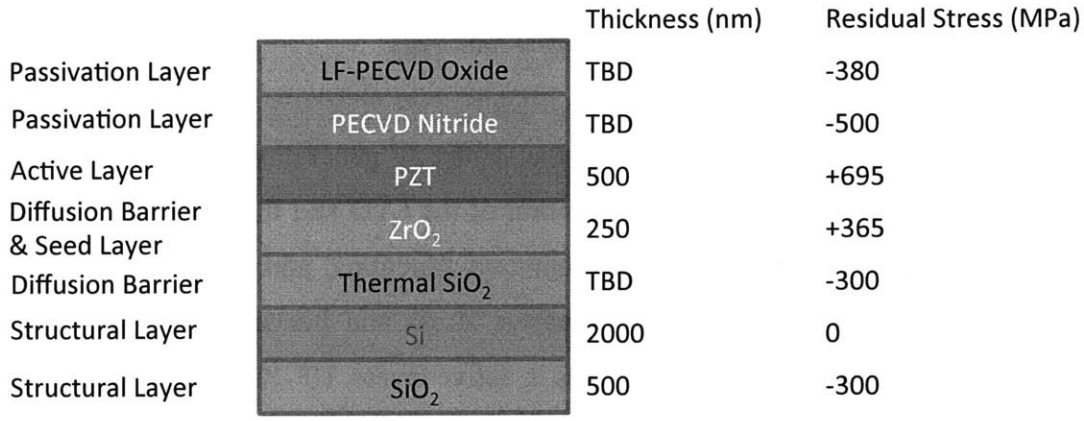

Figure 3-25 The proposed beam composition using silicon as the structural layer.

To further design the beam composition, the thicknesses should be specified. The thicknesses of some layers can be pre-determined, such as the thickness of structural layer and active layers. These thicknesses are mainly governed by their functionality and

deposition limitations, and cannot be optimized. Three thicknesses in both proposed compositions can then ready to be determined.

The process of finding the optimized thicknesses of the rest layers can be explained as follows: the unknown thicknesses as variables are first set a range, which is mainly determined by the fabrication limitation. Then the total residual stress of the beam can be found for each variable thickness, the moment generated in the beam due to the unsymmetrical residual stress distribution can also be determined. The thicknesses set that leads to minimized total residual stress and moment are the optimized solution. A Matlab program (Appendix) based on this algorithm was developed for looking for the design space numerically and find out the best thicknesses for the two proposed compositions. The material properties used in this estimation are inherited from our previous research and are listed in Table 3-6.

Table 3-6 Material properties used for the design optimization.

	Si	SiO_2	Si_3N_4	PZT	ZrO_2
Young's modulus (GPa)	180	70	300	63	244
Poisson's ratio	0.27	0.17	0.2	0.3	0.27

The optimized thicknesses for both beam compositions are listed in Table 3-7. It should be noted that it is not easy to know if the moment generated by the residual stress is small enough, therefore, the ratio of the tip deflection of a cantilever structure (L: 4mm, W: 6mm) to the total thickness of the beam is used to compare the moment and determine how symmetrical the residual stress distribution is.

Table 3-7 The optimized thicknesses and related characterization for the two proposed beam composition designs.

	Si_3N_4 based composition	Si based composition
Thermal oxide thickness	460 nm	580 nm
PECVD nitride thickness	60 nm	40 nm
PECVD oxide thickness	180 nm	700 nm
Total thickness	2450 nm	4570 nm
Total residual stress	0	0
Ratio of tip deflection to beam thickness	0.11%	8.4%

Once the thicknesses are determined, length and proof mass can be optimized in the similar way by finding the solutions that have the lowest operating frequency and widest bandwidth. To verify the concept, fabrication may be based on the 3rd generation device masks, plug in the beam length of 4mm and 1g proof mass, the frequency response of the two composition designs can be found (Fig. 3-26 and Fig. 3-27).

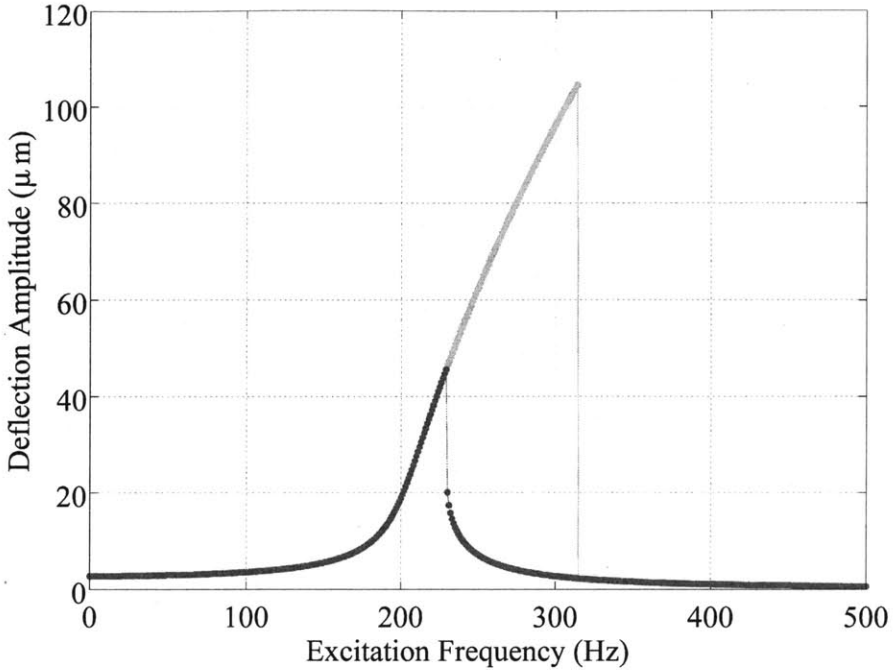

Figure 3-26 Frequency response of the design based on the first beam composition design and 3rd generation masks.

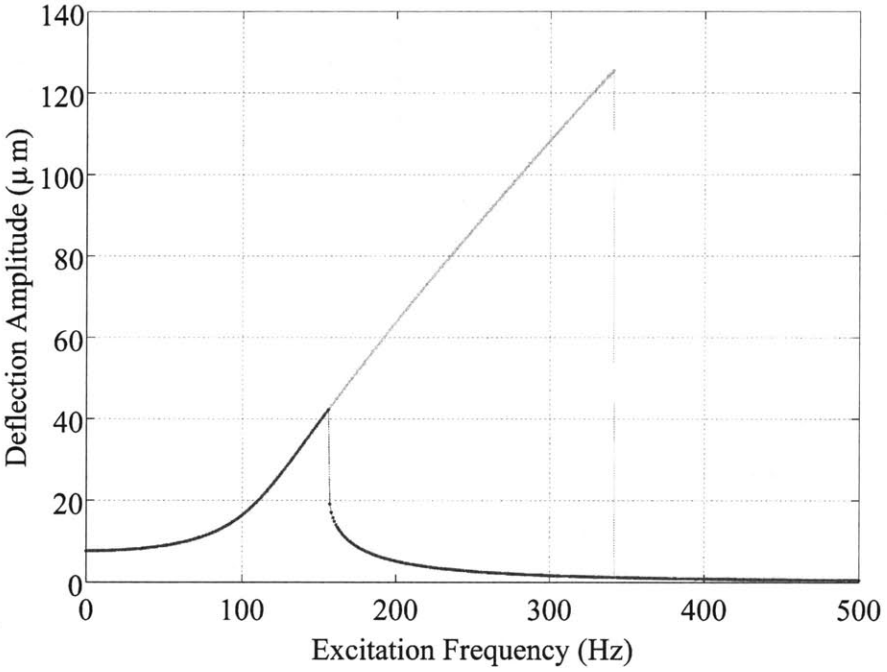

Figure 3-27 Frequency response of the design based on the second beam composition design and 3rd generation masks.

Chapter 4 Fabrication

Micro fabrication of an energy harvester can be tricky and time consuming. The 3rd generation device fabrication process consists of thermal oxidation, low-pressure chemical vapor deposition (LPCVD) to deposit structural layers, spin coating, pyrolyzing and annealing ZrO_2 and PZT to build active layer, lifting-off to pattern electrodes, plasma-enhanced chemical vapor deposition (PECVD) to coat passivation layers, 7 photolithography steps (5 masks) to define beam structure and proof mass, and wet and dry etching to release the beam and proof mass to make a final device.

To successfully fabricate a new generation device, mastering all these fabrication techniques and verifying the effectiveness of the recipes are necessary. To make these preparations, a repetition of the whole 3rd generation device process (Figure 4-1) has been made. Although the process is almost the same to the original one, problems emerged when repeating the process. Efforts have been made to solve them, and modifications on the original recipe have made. This chapter is intended to briefly report what have been done in the preliminary fabrication preparation, and more importantly to present the problems and related analysis, updated recipes and possible improvements for future fabrication.

Structural Layer

The structural layer consists of one layer of thermal oxide (~970 nm), one layer of LPCVD silicon nitride (~1560 nm) and one layer of low temperature oxide (LTO) of ~700 nm. All these depositions are made in Integrated Circuits Laboratory (ICL) by using standard recipes, so the yield rates are high compared to other steps. There are two things should be noticed, the first is the three deposition steps must be done seamlessly, coordination with staff who is in charge of the nitride deposition must be made before start. The other important step is to use monitor wafers in each procedure. The monitor

wafers will be used for characterization such as the deposition thickness and bow measurement for residual stress calculation.

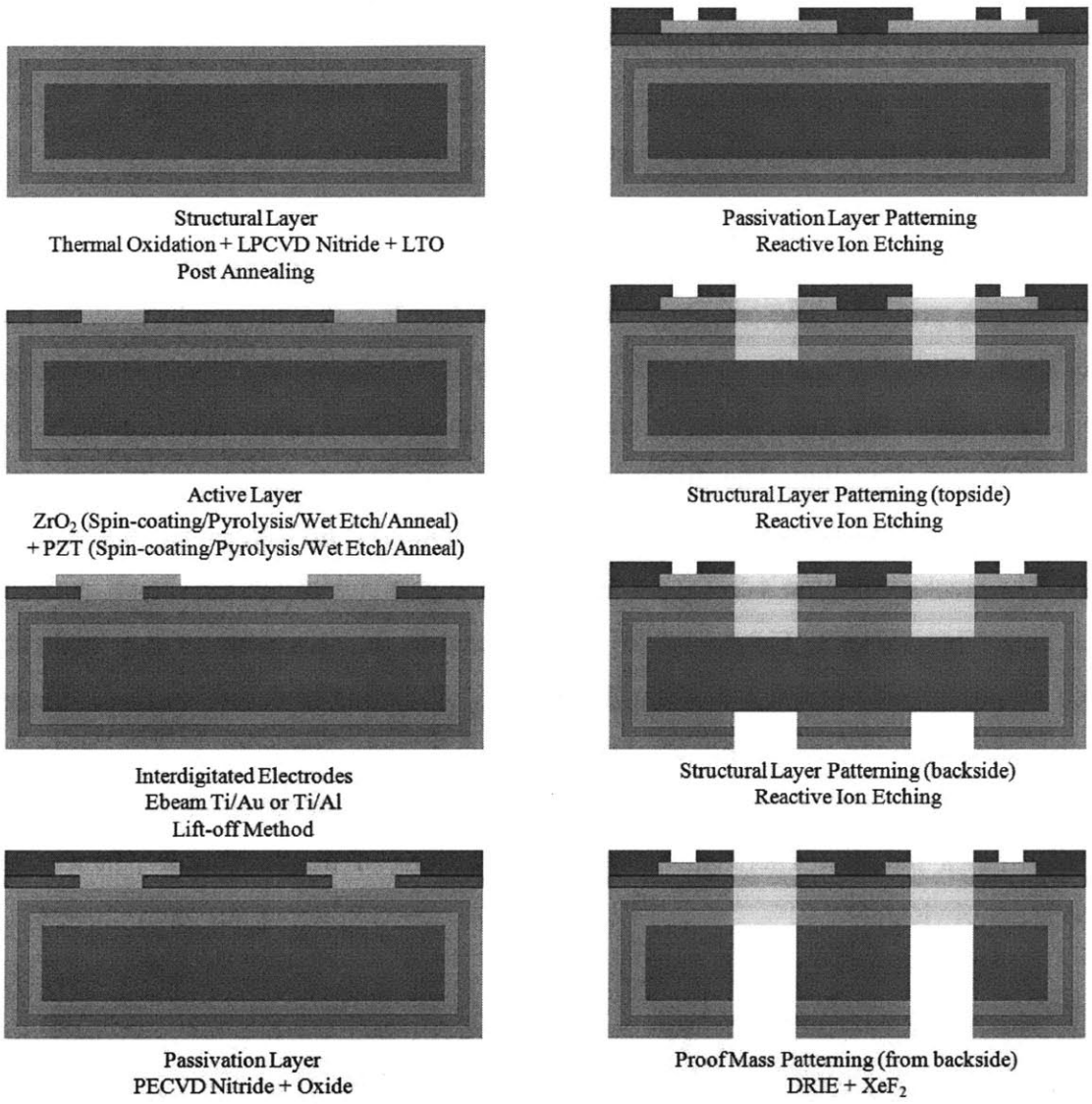

Figure 4-1 Fabrication process of 3rd generation design [5].

ZrO_2

ZrO_2 as a diffusion barrier is necessary for d_{33} mode configuration. Around 260 nm of ZrO_2 has been deposited under PZT in the 3rd generation device. The recipe was [5],

Solution: 9%wt ZrO_2 solution by Mitsubishi Materials

Spin-coat: 500 rpm (5secs) – 2500 rpm (25secs)

Drying/Pyrolysis: 200 °C (60secs) / 390 °C (300secs) on hotplates

Target thickness: 80nm – 100nm per coat

Etch: Diluted (1:20) BHF solution (10secs)

Anneal: 700 °C (60secs), RTA AG Associates Heatpulse 410

This recipe has been followed exactly, but it was found that the pyrolyzed ZrO_2 suffered from cracking problem. The cracking happens after first layer coating and pyrolysis, for every wafer. Since the quality of PZT will be affected by this, making crack-free coating is crucial. Figure 4-2 (a)-(d) shows the typical cracks have been seen during after pyrolysis before annealing. The different cracking patterns have been investigated, and here are some possible reasons: the dense cracks in Figure 4-2 (a) suggest serious thermal shock. The cracks in Figure 4-2 (b) are mainly due to particles which are shown as those black dots. The cracks in Figure 4-2 (c) concentrated in the area with a color gradient, which is normally due to non-uniform distribution of coating material, so these cracks may be caused by non-uniformity of coating. Figure 4-2 (d) shows the most commonly seen cracks during the trial process. The cracks are not dense but cover all over the wafer and distributed radially. There are no particles or signs of non-uniformity, hence the cause is not obvious.

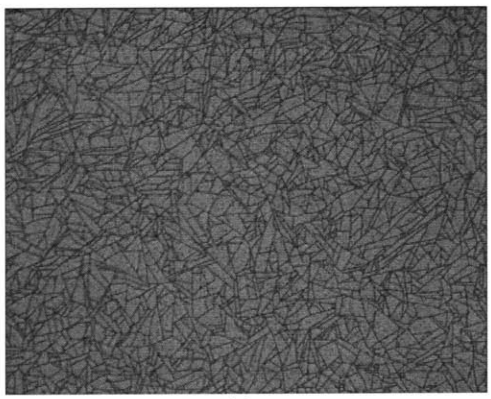

(a)

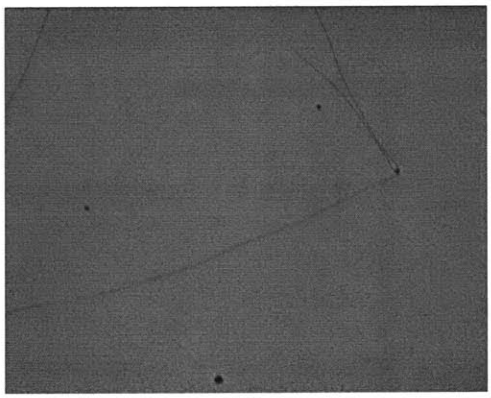

(b)

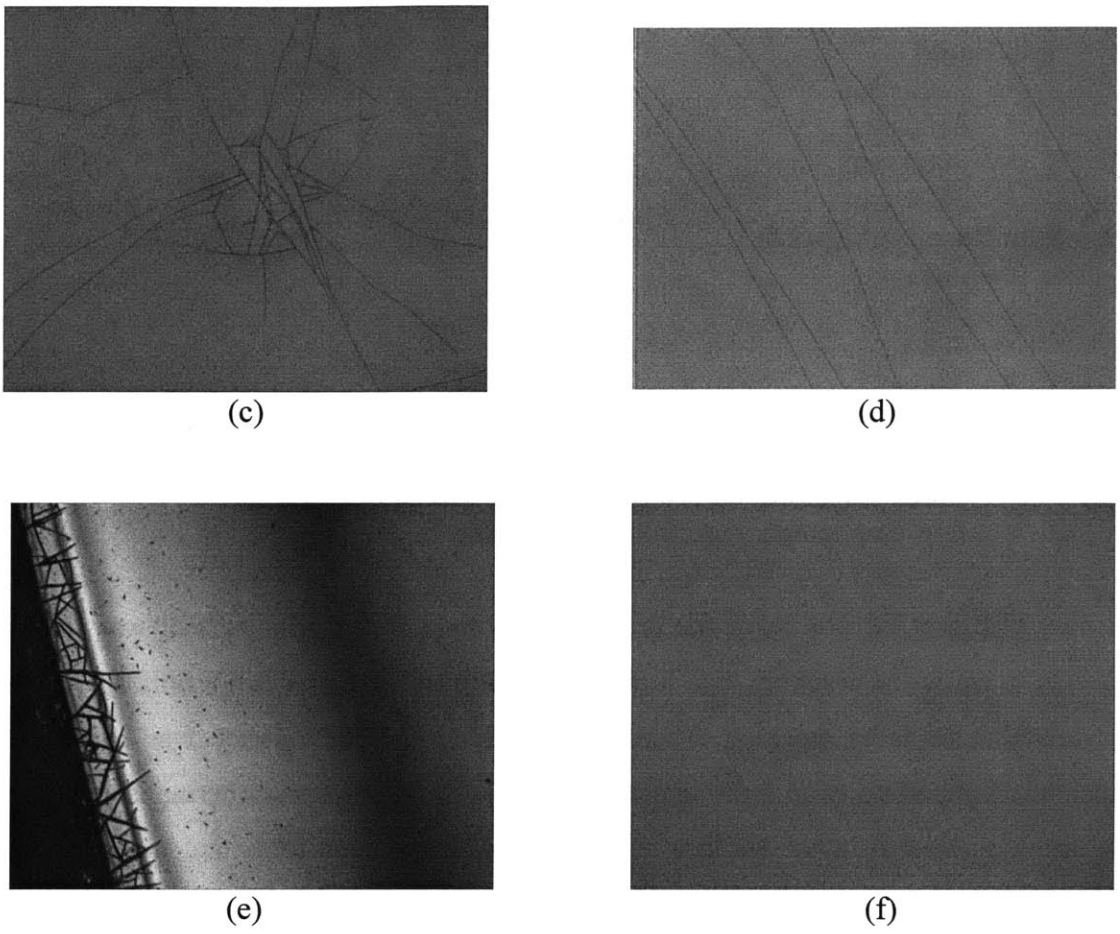

Figure 4-2 Microscopic pictures of pyrolyzed ZrO_2. (a) – (d) cracking after pyrolysis. (e) Edge of the wafer with good quality ZrO_2 after pyrolysis. (f) Crack-free ZrO_2.

To find out what causes the cracks in Figure 4-2 (d), different process parameters have been tuned, such as the solution itself, the volume of solution per coating, spin speed and time, and different pyrolysis conditions:

- **Solution**
  - Old sol-gel (July 2010)
  - New sol-gel (Nov 2011)
- **Volume**
  - 1 ml / coating
  - 2 ml / coating
  - 3 ml / coating
  - 4 ml / coating

- **Spin Speed**
  - 2000 rpm
  - 2500 rpm
  - 3000 rpm
  - 3500 rpm
- **Spin time (high speed)**
  - 20s
  - 25s
  - 30s
  - 35s
- **Pyrolysis (using hotplates)**
  - Two-stage heat-up (190 °C, 390 °C)
  - Three-stage heat-up (100 °C, 245 °C, 390 °C)
  - Ramp up temperature from room temperature to 390 °C

All these changes did not solve the cracking problem. But thermal effect was highly suspected to cause the cracking, and it may be the heat distribution is not uniform across the wafer that leads to cracking. Therefore, pyrolysis in PZT furnace was tried. The temperature ramped up from room temperature to 390°C to eliminate thermal shock, and since the temperature in the furnace should be much more uniform that that near the hotplate, the heat across the wafer can be thought uniform. After 5 min at 390°C, the temperature ramped down to ~100°C and the wafer was taken out. Cracking did not happen. The succeeding annealing did not produce cracks either. The wafer after annealing is shown in Figure 4-2 (e) and (f). There are some minor cracks at the edge of the wafer as shown in Figure 4-2 (e), which is normal, but they are not propagating further, so most of the wafer area suffers no cracking (Figure 4-2 (f)). The new recipe has been tried multiple times and all resulted in crack-free ZrO_2 coating, so the cracking problem has been solved. The new pyrolysis process takes much longer time, instead of ~10min for each coating when using hotplates, the new pyrolysis takes more than two hours for pyrolyzing one layer, however, the yield rates were proved to be high.

PZT

After getting crack-free ZrO_2 coating, PZT coating was done following the recipe from 2^{nd} generation device [5], since for practice purpose, E1 solution is cheaper than G3 type solution:

Solution: 1%wt PT/15% PZT E1 solution, Mitsubishi Materials
Spin-coat: 500 rpm (5secs) – 2500 rpm (25secs)
Drying/Pyrolysis: 380 °C (300 secs)
Target thickness: 80nm per coat
Repeat: 1 coat PT + 2 coats PZT

Crack-free PZT has been made and shown in Figure 4-3.

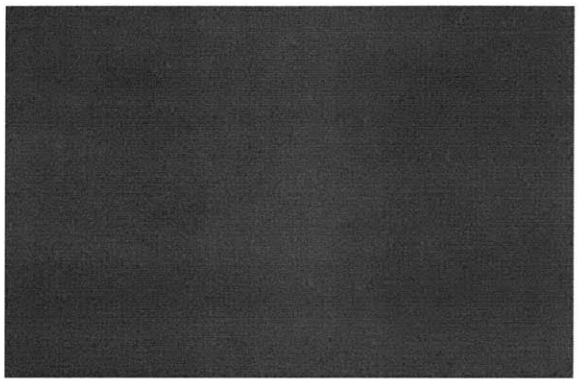

Figure 4-3 Crack-free PZT after annealing.

Electrodes

Interdigitated electrodes were made following 3rd generation recipe:

Lithography: AZ-5214 coat (2000rpm) / Exposure 1.4 secs / Flood Exposure 48secs
Electrodes: Ti/Al (200 Å / 1000 Å)
Ebeam: EBeamFP Temescal Model FC2000
Lift-off: acetone bath + ultrasound shaking

One point should be noticed is that an ashing step (6 min at 1000W) after lithography and before ebeam should be done, to remove any residual resist in clear region. Figure 4-4 shows the electrodes after lift-off.

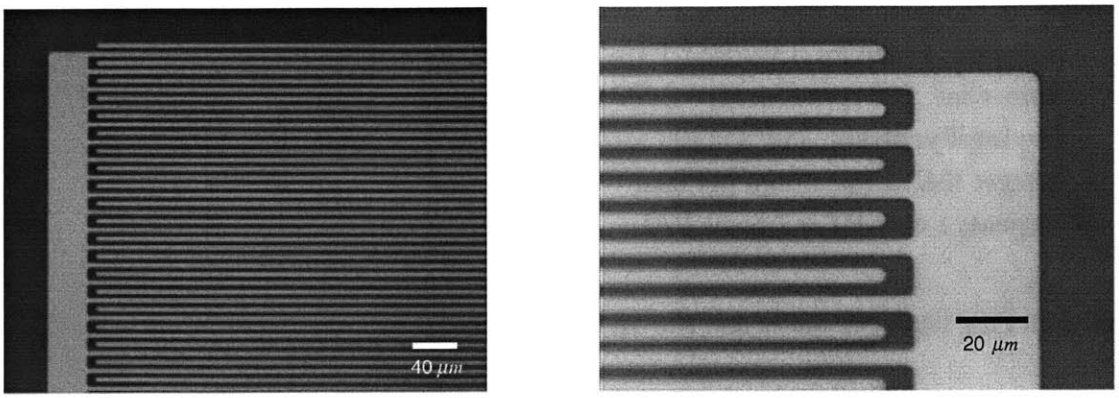

(a) (b)

Figure 4-4 Microscopic pictures of interdigitated electrodes.

Chapter 5 Testing

5.1 Electromechanical Testing Measurement

5.1.1 Testing Setup

The electromechanical testing on previous devices used to be performed at the Gas Turbine Laboratory, but it is anticipated that intense testing on our new devices will be done later. Therefore, new testing equipment was purchased to build a new electromechanical testing setup designated for energy harvester testing. An UROP student, You C. Yoon (Richard) and I worked together to build this setup and did testing. The author would like to thank him for his contribution.

The testing setup consists of five modules:

- Test device
- Electromagnetic shaker
- Monitoring devices
- Data acquisition
- Computer interface

Test Device

The test device is a purchase linear piezoelectric energy harvester Volture V21bl, which consists of 1 stack of 2 piezoelectric layers, has a frequency range of 45-155Hz and a dimension of 91×17×0.8 mm. A Volture tungsten tuning mass, which weighs 1g, can be attached to the end of the harvester to lower the resonance frequency. The harvester is bonded on a testing board and can then be mounted on shaker.

Electromagnetic Shaker

The test device is mounted on and excited by ET-126 electrodynamic shaker (Labworks Inc). An input signal is amplified by PA-138 linear power amplifier (Labworks Inc) and then fed into the shaker. Therefore, the vibration frequency is controlled by the signal generator, and the vibration intensity is controlled by the power amplifier.

Monitoring Devices

The signal fed into the shaker is monitored by an oscilloscope. The vibration of the shaker is sampled by accelerometer ACH-01 (Application Specification) which is mounted on the shaker.

Data Acquisition

The energy harvester is connected to a charge amplifier (VIP Sensors Model 5000), which converts the charge generated in the piezoelectric layer to an output voltage at a constant gain 100 mV/pC, then the amount of charge generated can be measured by the DAQ in form of voltage. The input and output signals are processed through a National Instrument PCI data acquisition card NI USB-6210, which is a multifunction DAQ with four 16-bit analog outputs, 32 analog inputs (250kS/s), and 48 digital I/O.

Computer Interface

Labview is used as the interface to collect data on computer, and Matlab is used for data processing.

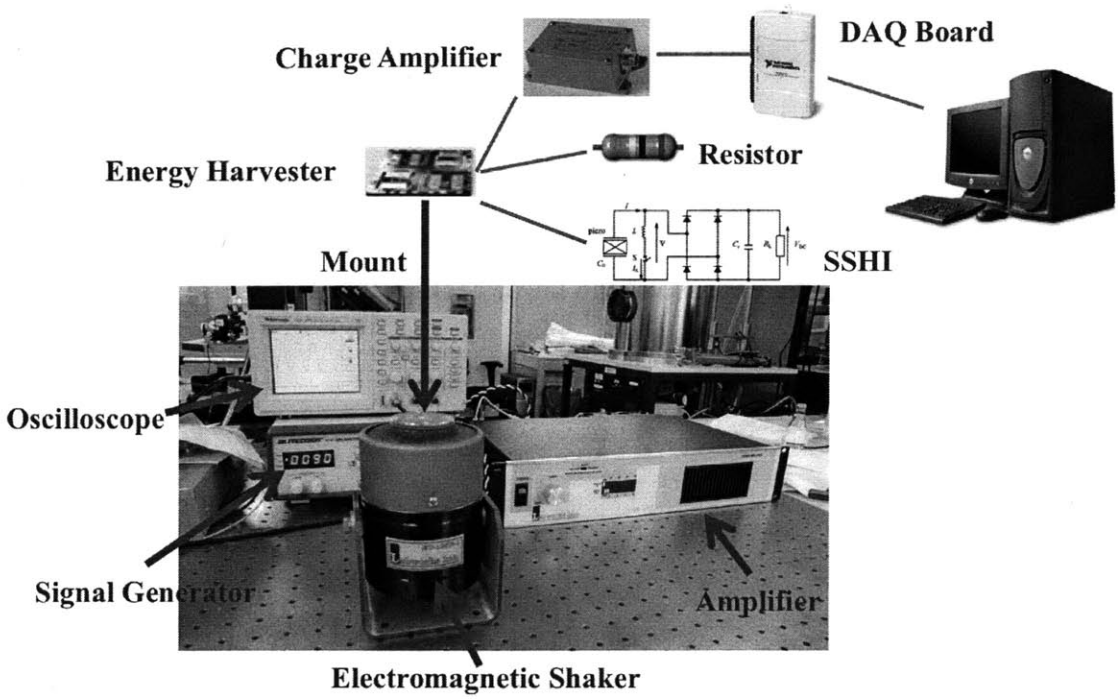

Figure 5-1 Overview of electromechanical testing setup.

5.1.2 Vibration Testing Results

To test the whole setup and get familiar with the characterization of energy harvester, the purchased test device was used to do the open circuit voltage measurement and output power measurement. Figure 5-2 shows the open circuit voltage versus the excitation frequency, as expected, the response of the linear cantilever based energy harvester has a sharp peak and bandwidth is narrow.

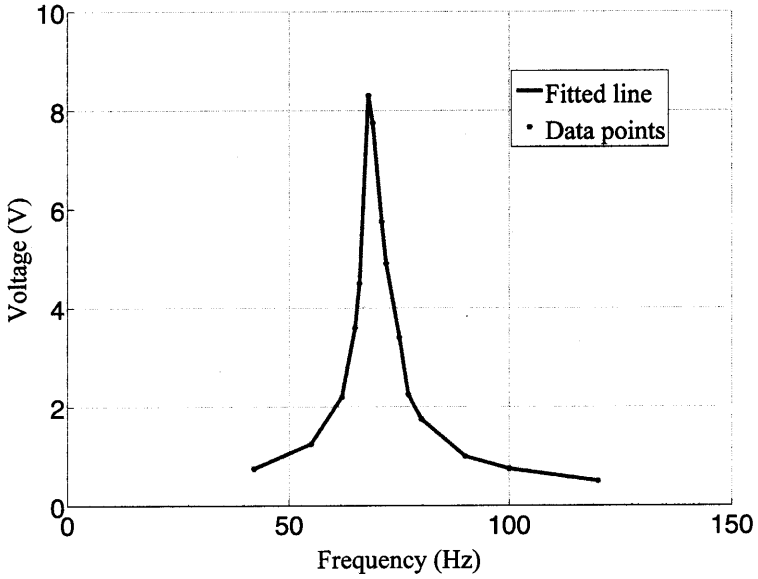

Figure 5-2 Open circuit voltage versus frequency of test device.

The output power of the energy harvester has also been measured. By shunting its output to various loads and measuring the voltage across the load, we can calculate the power consumed by the load. Figure 5-3 shows the power versus resistance. The response agrees with theoretical prediction, that is the maximum power is achieved when the load impedance matches the internal impedance.

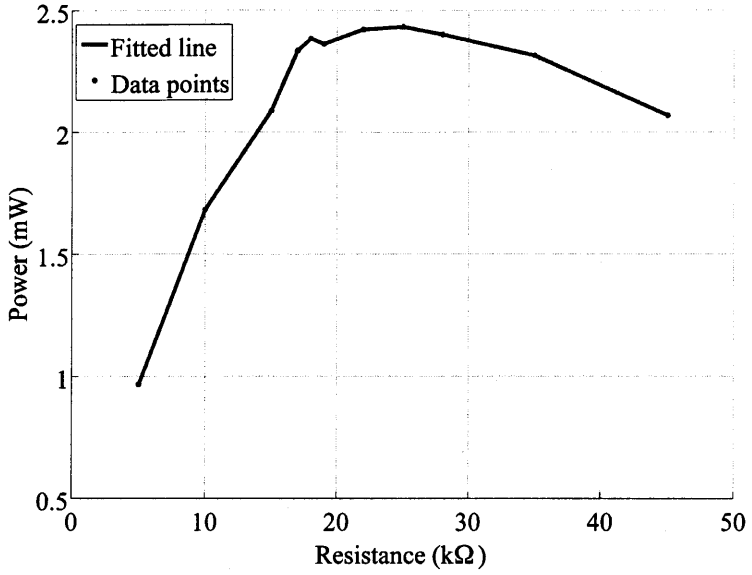

Figure 5-3 Output power versus load resistance.

The electromagnetic testing verifies that all the instruments work normally and can be employed for future measurements on new energy harvesters. The characterization of the test device demonstrated the limitation of linear resonator based piezoelectric energy harvesters.

Chapter 6 Summary

6.1 Thesis Summary

In addressing the high operating frequency and high-g excitation issues of the present energy harvesters, different design ideas such as coupled beams design, serpentine beam design and spiral beam design have been generated and investigated. It has been found that although these new design ideas have some merits, the optimization on part of the design parameters based on 3rd generation design is the best way to maintain the original features such as wide bandwidth while introducing new features of low operating frequency and low-g excitation.

The relationships between design parameters and design goals have been discovered, and elimination of irrelevant design parameters has been executed. A design framework was devised then to implement the accurate design of the low operating frequency, low-g energy harvesters. Constrained by physical conditions, residual stress balancing, beam composition design is implemented numerically by computer through a specially designed algorithm. The other design parameters such as beam length and proof mass can also be optimized in the similar way. Simulation results show that the new optimized design with the same geometry of our 3rd generation design has an operating frequency in the range of 200~300 Hz at 0.5g excitation level compared with the 1.3kHz operating frequency and 4g excitation of the 3rd generation design. Further optimization on beam length to decrease the operation frequency is possible.

Fabrication repeating the 3rd generation design process has been done for the preparation of future device prototyping. In the process, problems such as the cracking in ZrO_2 coating have been resolved, and corresponding recipes have been modified.

Electromechanical testing setup, including electromagnetic shaker, data acquisition and computer interface has been built up and tested for future intense device testing.

6.2 Future Work

The proposed design has been proved theoretically to have enhanced performance, including much lower operating frequency and excitation level compared with previous design. But to verify the true performance, fabrication of the prototype should be made, and related electromechanical testing is needed for characterization.

Although doubly clamped design is still the best option in terms of the balance between device bandwidth and operating frequency compared with other investigated designs, the nonlinearity is not easy to be triggered, and operating frequency of this design is bounded. New designs which have better nonlinearity, which means wider bandwidth, and even lower operating frequencies such as <100Hz are possible and should be explored.

This thesis work mainly focuses on the energy harvester design; however, electrical interface has been proven to have a tremendous impact on the generated power and power generation bandwidth. Synchronized switching harvesting on the inductor has been proposed for energy harvesting purpose in our previous research. Future work will be to explore the most effective circuitry for nonlinear resonator based energy harvesters and implement it.

Bibliography

[1] S. P. Beeby, M. J. Tudor, and N. M. White, "Energy harvesting vibration sources for microsystems applications," *Measurement Science and Technology*, vol. 17, 2006.

[2] S. Roundy, P. K. Wright, and J. Rabaey, "A study of low level vibrations as a power source for wireless sensor nodes," *Computer Communications*, vol. 26, no. 11, pp. 1131-1144, Jul. 2003.

[3] Roundy S and Zhang Y 2005 Toward self-tuning adaptive vibration based micro-generators Smart Materials, Nano- and Micro-Smart Systems (Sydney, Dec.).

[4] Beeby, S.; Tudor, M.; Torah, R.; Roberts, S.; O'Donnell, T. & Roy, S. (2007). Experimental comparison of macro and micro scale electromagnetic vibration powered generators, In: Microsystem Technologies, Vol.13, No.12-13, pp. 1647-1653.

[5] A. Hajati, "Ultra Wide-Bandwidth Micro Energy Harvester," PhD thesis in EECS, Massachusetts Institute of Technology, 2011.

[6] Jeon Y B, Sood R, Jeong J H and S.-G. Kim, "MEMS power generator with transverse mode thin film PZT", Sensors and Actuators, pp.16–22, 2005.

[7] Senturia S.D., Microsystem Design, Springer, 2001.

[8] Standards Committee of the IEEE Ultrasonics, Ferroelectrics, and Frequency Control Society. "An American National Standard IEEE Standard on Piezoelectricity," 1988.

[9] E. S. Leland, J. Baker, E. Reilly, B. Otis, J. M. Rabaey, and P. K. Wright, "Improving Power Output for Vibration-Based Energy Scavengers," 2005.

[10] Engel T G, Keawboonchuay C and Nunnally W C 2000 Energy conversion and high power pulse production using miniature piezoelectric compressors IEEE Trans. Plasma Sci. 28 1338–41188.

[11] S. Moss, A. Barry, I. Powlesland, S. Galea, and G.P. Carman, "A low profile vibro-impacting energy harvester with symmetrical stops," Applied Physics Letters, vol. 97, 2010, p. 234101.

[12] S. Moss, A. Barry, I. Powlesland, S. Galea, and G. P. Carman, "A broadband vibro-impacting power harvester with symmetrical piezoelectric," vol. 045013, 2011.

[13] From K. a Cook-Chennault, N. Thambi, and a M. Sastry, "Powering MEMS portable devices—a review of non-regenerative and regenerative power supply systems with special emphasis on piezoelectric energy harvesting systems," *Smart Materials and Structures*, vol. 17, no. 4, p. 043001, Aug. 2008.

[14] Myers R, VickersM, Kim H and Priya S 2007, "Small scale windmill", Appl. Phys. Lett. 90 3.

[15] Schmidt V H 1992 Piezoelectric energy conversion in windmills IEEE Ultrason. Symp. pp 897–904.

[16] Priya S 2005, "Modeling of electric energy harvesting using piezoelectric windmill", Appl. Phys. Lett. 87 184101.

[17] Allen J J and Smits A J, 2001 Energy harvesting eel, J. Fluids Struct. 15, pp. 629–40.

[18] Taylor GW, Burns J R, Kammann SM, PowersWB and Welsh T R 2001 "The energy harvesting eel: a small subsurface ocean/river power generator", IEEE J. Ocean. Eng. 26 539–47.

[19] H. D. Akaydin, N. Elvin, and Y. Andreopoulos, "Energy Harvesting from Highly Unsteady Fluid Flows using Piezoelectric Materials," *Journal of Intelligent Material Systems and Structures*, 2010.

[20] Pobering S and Schwesinger N 2004, "A novel hydropower harvesting device", Proc. 2004 Int. Conf. on MEMS, NANO and Smart Systems (Banff, AL, Aug.) pp. 480–5

[21] D. S. Clair, A. Bibo, V. R. Sennakesavababu, M. F. Daqaq, and G. Li, "A scalable concept for micropower generation using flow-induced self-excited oscillations," pp. 3-5, 2010.

[22] Platt S R, Farritor S, Garvin K and Haider H 2005, "The use of piezoelectric ceramics for electric power generation within orthopedic implants", IEEE–ASME Trans.Mechatron. 10 455–61.

[23] Niu P, Chapman P, Riemer R and Zhang X 2004, "Evaluation of motions and actuation methods for biomechanical energy harvesting", Proc. IEEE 35th Annual Power Electronics Specialists Conf. (Aachen) pp. 2100–6.

[24] Renaud M, Sterken T, Fiorini P, Puers R, Baert K and Van Hoof C 2005, "Scavenging energy from human body: design of a piezoelectric transducer", Proc. 13th Int. Conf. on Solid-State Sensors and Actuators and Microsystems (Seoul, June) pp 784–7.

[25] Gonz´alez J L, Rubio A and Moll F 2002, "Human powered piezoelectric batteries to supply power to wearable electronic devices", Int. J. Soc. Mater. Eng. Resources 10 34–40.

[26] Shenck N S and Paradiso J A 2001, "Energy scavenging with shoe-mounted piezoelectrics", IEEEMicro 21 30–42.

[27] Mateu L andMoll F 2005, "Optimum piezoelectric bending beam structures for energy harvesting using shoe inserts", J. Intell. Mater. Syst. Struct. 16 835–45.

[28] B. Yang and K.-S. Yun, "Piezoelectric shell structures as wearable energy harvesters for effective power generation at low-frequency movement," *Sensors and Actuators A: Physical*, Mar. 2012.

[29] Lee C S, Joo J, Han S and Koh S K 2004, "Multifunctional transducer using poly(vinylidene fluoride) active layer and highly conducting poly(3,4-ethylenedioxythiophene) electrode: actuator and generator", Appl. Phys. Lett. 85, pp 1841–3.

[30] Lee C S, Joo J, Han S, Lee J H and Koh S K 2005 "Poly(vinylidene fluoride) transducers with highly conducting".

[31] Mohammadi F, Khan A and Cass R B 2003, "Power generation from piezoelectric lead zirconate titanate fiber composites", Proc. Materials Research Symp. pp 736.

[32] Churchill D L, HamelMJ, Townsend C P and Arms SW2003, "Strain energy harvesting for wireless sensor networks", Proc. Smart Struct. and Mater. Conf.; Proc. SPIE 5055 319–27.

[33] Yang J, Zhou H, Hu Y and Jiang Q 2005, "Performance of a piezoelectric harvester in thickness-stretch mode of a plate", IEEE Trans. Ultrason. Ferroelectr. Freq. Control 52 1872–6.

[34] Cho J, Anderson M, Richards R, Bahr D and Richards C 2005a, "Optimization of electromechanical coupling for a thin-film PZT membrane: I. modeling", J. Micromech. Microeng. 15 1797–803.

[35] Richards C D, AndersonMJ, Bahr D F and Richards R F 2004, "Efficiency of energy conversion for devices containing a piezoelectric component", J. Micromech. Microeng. 14 pp 717–21.

[36] Ng T H and LiaoWH 2005, "Sensitivity analysis and energy harvesting for a self-powered piezoelectric sensor", J. Intell. Mater. Syst. Struct. 16 pp 785–97.

[37] Han J, Von Jouanne A, Le T, Mayaram K and Fiez T S 2004, "Novel power conditioning circuits for piezoelectric micro power generators", Proc. 19th Ann. IEEE Applied Power Electronics Conf. and Exposition Conf. pp 1541–6.

[38] Tayahi MB, Johnson B, HoltzmanMand Cadet G 2005, "Piezoelectric materials for powering remote sensors", Proc. IEEE 24th Int. Performance, Computing, and Communications Conf. (Phoenix, AZ, April) pp 383–6.

[39] Lefeuvre E, Badel A, Richard C and Guyomar D 2004, "High performance piezoelectric vibration energy reclamation", Proc. Smart Structures and Materials Conf.; Proc. SPIE 5390 379–87 Lefeuvre E, Badel A, Richard C and Guyomar D 2005b Piezoelectric.

[40] Badel A, Guyomar D, Lefeuvre E and Richard C 2005, "Efficiency enhancement of a piezoelectric energy harvesting device in pulsed operation by synchronous charge inversion", J. Intell. Mater. Syst. Struct. 16, pp 889–901.

[41] W. Al-ashtari, M. Hunstig, T. Hemsel, and W. Sextro, "Frequency tuning of piezoelectric energy harvesters by magnetic force," *Mechatronics*, vol. 35019, 2012.

[42] M. O. Mansour, M. H. Arafa, and S. M. Megahed, "Resonator with magnetically adjustable natural frequency for vibration energy harvesting," *Sensors & Actuators: A. Physical*, vol. 163, no. 1, pp. 297-303, 2010.

[43] Gieras J F, Oh J-H, HuzmezanMand Sane H S 2007, "Electromechanical energy harvesting system", Patent Publication Number: WO2007070022(A2), WO2007070022(A3).

[44] Wu X, Lin J, Kato S, Zhang K, Ren T and Liu L 2008, "A frequency adjustable vibration energy harvester", Proc. PowerMEMS 2008+ microEMS2008 (9–12 November 2008, Sendai, Japan) pp 245–8.

[45] D. Zhu, M. J. Tudor, and S. P. Beeby, "Strategies for increasing the operating frequency range of vibration energy harvesters : a review," vol. 21, 2010.

[46] Shahruz SM2006a, "Design of mechanical bandpass filters for energy scavenging", J. Sound Vib. 292 987–98.

[47] Shahruz SM2006b, "Limits of performance of mechanical band-pass filters used in energy scavenging", J. Sound Vib. 293, pp 449–61.

[48] B. P. Mann and N. D. Sims, "Energy harvesting from the nonlinear oscillations of magnetic levitation," *Journal of Sound and Vibration*, vol. 319, pp. 515-530, 2009.

[49] D. A. W. Barton, S. G. Burrow, and L. R. Clare, "Energy Harvesting From Vibrations With a Nonlinear Oscillator," *Journal of Vibration and Acoustics*, vol. 132, no. April, pp. 1-7, 2010.

[50] A. Erturk and D. J. Inman, "Broadband piezoelectric power generation on high-energy orbits of the bistable Duffing oscillator with electromechanical coupling," *Journal of Sound and Vibration*, vol. 330, no. 10, pp. 2339-2353, 2011.

[51] F. Cottone, L. Gammaitoni, H. Vocca, M. Ferrari, and V. Ferrari, "Piezoelectric buckled beams for random vibration energy harvesting," vol. 35021, 2012.

[52] D. S. Nguyen, E. Halvorsen, G. U. Jensen, and a Vogl, "Fabrication and characterization of a wideband MEMS energy harvester utilizing nonlinear springs," *Journal of Micromechanics and Microengineering*, vol. 20, no. 12, p. 125009, Dec. 2010.

[53] Rastegar J, Pereira C and Nguyen H L 2006, "Piezoelectric-based power sources for harvesting energy from platforms with low frequency vibration", Proc. Smart Structures and Materials Conf.; Proc. SPIE 6171 617101.

[54] T. V. Galchev, J. Mccullagh, R. L. Peterson, and K. Najafi, "Harvesting traffic-induced vibrations for structural health monitoring of bridges," vol. 21, 2011.

[55] T. Galchev, E. E. Aktakka, H. Kim, and K. Najafi, "A Piezoelectric Frequency-increased Power Generator for Scavenging Low-frequency Ambient Vibration," *Computer*, pp. 1203-1206, 2010.

[56] White NM, Glynne-Jones P and Beeby S P 2001, "A novel thick-film piezoelectric micro-generator", Smart Mater. Struct. 10 pp 850–2.

[57] Muralt P, MarzenckiM, Belgacem B, Calame F and Basrour S 2009, "Vibration energy harvesting with PZT micro device", Proc. Chem. 1 pp 1191–4.

[58] H. Liu, C. J. Tay, C. Quan, T. Kobayashi, C. Lee, and A. Abstract, "Piezoelectric MEMS Energy Harvester for Low-Frequency Vibrations With Wideband Operation Range and Steadily Increased Output Power," *October*, vol. 20, no. 5, pp. 1131-1142, 2011.

[59] A. Massaro et al., "Freestanding piezoelectric rings for high efficiency energy harvesting at low frequency," Applied Physics Letters, pp. 30-32, 2011.

[60] L. M. Miller, E. Halvorsen, T. Dong, and P. K. Wright, "Modeling and experimental verification of low-frequency MEMS energy harvesting," vol. 045029, 2011.

[61] N. Dutoit, B. Wardle, and S.-G. Kim, "Design Considerations for Mems-Scale Piezoelectric Mechanical Vibration Energy Harvesters," *Integrated Ferroelectrics*, vol. 71, no. 1, pp. 121-160, Jul. 2005.

[62] Timoshenko, Stephen P., Woinowsky-Krieger, S., Theory of Plates and Shells (2nd Edition), McGraw-Hill.

[63] Nayfeh, Ali Hasan. "4.1 System with cubic nonlinearities" in Nonlinear Oscillations, New York : Wiley, 1979, pp. 168 – 171.

[64] M. Brennan, I. Kovacic, a Carrella, and T. Waters, "On the jump-up and jump-down frequencies of the Duffing oscillator", Journal of Sound and Vibration, vol. 318, Dec. 2008, pp. 1250-1261.

Appendix Matlab Codes

Composite Beam Stiffness

```
% Stiffness of Composite Beams

clear all
clc

% Young's Modulus (Pa)
E_PZT = 63e9;
E_ZrO2 = 244e9;
E_SiO2_Thermal = 69e9;
E_SiO2_LF_PECVD = 69e9;
E_SiO2_HF_PECVD = 69e9;
E_LTO = 69e9;
E_SiNx = 313e9;
E_Si = 185e9;

% Input Parameters

n = 3; % Number of layers(from bottom to top, the index goes from 1 to n)

W = 5e-3; % Width of the beam
L = 10e-3; % Length of the beam
E = [185e9, 69e9, 313e9]; % Young's modulus for each material
nu = [0, 0, 0]; % Poisson's ratio
E_ = E ./ (1 - nu); % Biaxial modulus
T = [1e-6, 1e-6, 1e-6]; % Thickness of each layer
rho = [inf, 60, 78]; % Radius of curvature
S0(1) = 0; % % Residual stress before release, assume the bottom layer (i = 1) has zero residual stress

%%%%%%%%%%%%%%%%%%%%%%%%%%%%%%%%%%%%%%%%%%%%%%%%%%%%%%%%%%%%%%%%%%%%%%%%%%%%%%%%%%%%%%%%%%%%%%%%
% Neutral Axis (assume the neutral axis is below bottom of the beam and the
% distance from neutral axis to the bottom surface of the beam is h, so h will be
% negative, and abs(h) is the distance of neutral axis from bottom)

syms Eq h; % Eq denotes the equation of calculating the neutral axis

for i=2:n
```

```
    Eq = 0;
    for j = 1:i
        Eq = Eq + E(j) * (h + sum(T(1:j)) - 1/2*T(j)) * T(j);
    end
    H(i) = solve(Eq, h);
end

H = double(H); % Converting from sym to double for later calculation

clear Eq

%%%%%%%%%%%%%%%%%%%%%%%%%%%%%%%%%%%%%%%%%%%%%%%%%%%%%%%%%%%%%%%%%%%%%%%%%%%%%%%
% Find the residual stress in each layer before release and bending

syms sigma % Residual stress in ith layer
% epsilon(1) = 0, Assume the bottom layer (i = 1) has zero residual stress

for i = 2:n

    M = 0; % Moment
    E_I = 0; % Effective E_*I product

    epsilon(i) = sum ([S0(1:i-1), sigma] .* T(1:i)) / sum (E_(1:i) .* T(1:i)); % Total strain
of the beam due to residual stresses

    for j = 1:i % Find the residual stress in each layer after release
        if j < i
            S0_(j) = S0(j) - E_(j) * epsilon(i);
        else
            S0_(j) = sigma - E_(j) * epsilon(i);
        end
    end

    for j = 1:i
        E_I = E_I + E_(j) * 1/3 * ( (H(i) + sum(T(1:j)))^3 - (H(i) + sum(T(1:j-1)))^3); %
Already drop out width, since it will be canceled out by moment, which also has a "W"
        M = M + S0_(j) * 1/2 * ( (H(i) + sum(T(1:j)))^2 - (H(i) + sum(T(1:j-1)))^2);
    end

    Eq = M * rho(i) - E_I;
    S0(i) = solve(Eq, sigma);
end

S0 % Display the residual stress in each layer
```

```
%%%%%%%%%%%%%%%%%%%%%%%%%%%%%%%%%%%%%%%%%%%%
% The radius of curvature of the whole beam
E_I = 0;
M = 0;

for i = 1:n
   epsilon(i) = sum (S0(1:i) .* T(1:i)) / sum (E_(1:i) .* T(1:i));
   S0_(i) = S0(i) - E_(i) * epsilon(i);
   E_I = E_I + E_(i) * 1/3 * ( (H(i) + sum(T(1:i)))^3 - (H(i) + sum(T(1:i-1)))^3);
   M = M + S0_(i) * 1/2 * ( (H(i) + sum(T(1:i)))^2 - (H(i) + sum(T(1:i-1)))^2);
end

rho = E_I / M % Display the radius of curvuature of the whole beam

%%%%%%%%%%%%%%%%%%%%%%%%%%%%%%%%%%%%%%%%%%%%
% Find the stiffness of the composite beam

K_b = 0; % Bending stiffness
K_r = 0; % Stiffness due to residual stress
K_s = 0; % Stretching stiffness

for i = 1:n
   K_b  = K_b+ 2/3 * pi^4 * W * L^-3 * E(i)  * ( (H(n) + sum(T(1:i)))^3 - (H(n) +
sum(T(1:i-1)))^3);
   K_r  = K_r+ 1/2 * pi^2 * W * L^-1 * S0(i)  * ( sum(T(1:i)) - sum(T(1:i-1)));
   K_s  = K_s+ 1/8 * pi^4 * W * L^-3 * E(i)  * ( sum(T(1:i)) - sum(T(1:i-1)));
end

K_b
K_r
K_s
```

Residual Stress Extraction

```
% Residual Stress Calculation
% Input: Radius of Curvature
% Output: Residual Stress in Each Layer
% Assume the bottom layer (i = 1) has zero residual stress

clear all
clc

L = 10e-2;

% Input Parameters

n = 8; % Number of layers(from bottom to top, the index goes from 1 to n)

E = [185e9, 69e9, 313e9, 69e9, 244e9, 63e9, 69e9, 69e9]; % Young's modulus for each
material
nu = [0, 0, 0, 0, 0, 0, 0, 0]; % Poisson's ratio
E_ = E ./ (1 - nu); % Biaxial modulus
T = [550e-6, 970e-9, 1560e-9, 700e-9, 260e-9, 270e-9, 1000e-9, 805e-9]; % Thickness of
each layer
B = [-0, 27.4e-6, -39.5e-6, 2.6e-6, -8.7e-6, -15.2e-6, 34.8e-6, 20e-6];
rho = -(B.^2 + L ^ 2 / 4) / 2 ./ B; % Radius of curvature
S0(1) = 0; % Residual stress before release, assume the bottom layer (i = 1) has zero
residual stress

%%%%%%%%%%%%%%%%%%%%%%%%%%%%%%%%%%%%%%%%%%%%%%%%%%%%%%%%%%%%%%%%%%%%%%%%%%%%%%%
% Neutral Axis

syms Eq h; % Eq denotes the equation of calculating the neutral axis

for i=2:n
   Eq = 0;
   for j = 1:i
      Eq = Eq + E(j) * (h + sum(T(1:j)) - 1/2*T(j)) * T(j);
   end
   H(i) = solve(Eq, h);
end

clear Eq

%%%%%%%%%%%%%%%%%%%%%%%%%%%%%%%%%%%%%%%%%%%%%%%%%%%%%%%%%%%%%%%%%%%%%%%%%%%%%%%
% Find the residual stress in each layer before release and bending
```

```
syms sigma % Residual stress in ith layer
% epsilon(1) = 0, Assume the bottom layer (i = 1) has zero residual stress

for i = 2:n

   M = 0; % Moment
   E_I = 0; % Effective E_*I product

   epsilon(i) = sum ([S0(1:i-1), sigma] .* T(1:i)) / sum (E_(1:i) .* T(1:i)); % Total strain
of the beam due to residual stresses

   for j = 1:i % Find the residual stress in each layer after release
      if j < i
         S0_(j) = S0(j) - E_(j) * epsilon(i);
      else
         S0_(j) = sigma - E_(j) * epsilon(i);
      end
   end

   for j = 1:i
      E_I = E_I + E_(j) * 1/3 * ( (H(i) + sum(T(1:j)))^3 - (H(i) + sum(T(1:j-1)))^3); %
Already drop out width, since it will be canceled out by moment, which also has a "W"
      M = M + S0_(j) * 1/2 * ( (H(i) + sum(T(1:j)))^2 - (H(i) + sum(T(1:j-1)))^2);
   end

   Eq = M * rho(i) - E_I;
   S0(i) = solve(Eq, sigma);
end

S0 % Display the residual stress in each layer
```

Beam Thickness Design

```
% Beam Thickness Design
% Input: Composition, estameted residual stress in each layer
% Output: thickness of compensation layers
% Assume the bottom layer (i = 1) has zero residual stress
% The composition (from bottom to top) is: Thermal SiO2 t1 nm, LPCVD SiN 1000 nm,
ZrO2 250nm,
% PZT 500nm, PECVD SiN t2 nm, PECVD SiO2 t3 nm.

clear all
clc

% Input Parameters

L = 4e-3; % Length of the beam
W = 6e-3; % Width of the beam

n = 7; % Number of layers(from bottom to top, the index goes from 1 to n)
E = [180e9, 70e9, 300e9, 244e9, 63e9, 300e9, 70e9]; % Young's modulus for each
material
nu = [0.27, 0.17, 0.2, 0.27, 0.3, 0.2, 0.17]; % Poisson's ratio
E_ = E ./ (1 - nu); % Biaxial modulus
T = [1e-18, 0, 1000e-9, 250e-9, 500e-9, 0, 0]; % Thickness of each layer (first layer is
always silicon, it's dummy layer, leave blank for deciding later)
S0 = [0, -300e6, 275e6, 365e6, 695e6, -500e6, -380e6]; % % Residual stress before
release, assume the bottom layer (i = 1) has zero residual stress

%%%%%%%%%%%%%%%%%%%%%%%%%%%%%%%%%%%%%%%%%%%%%%%%%%%%%%%%%%%%%%%%%%%%%%%%%%%%%%%%
t1 = 20e-9:40e-9:1500e-9; % Design space (thickness of themal oxide layer)
t2 = 20e-9:20e-9:200e-9; % Design space (thickness of PECVD SiN layer)
t3 = 20e-9:40e-9:1500e-9; % Design space (thickness of PECVD SiO2 layer)

syms Eq h; % Eq denotes the equation of calculating the neutral axis
q = 1; % An index number for recording candidate combinations

% Search in the design space (t1, t2, t3), looking for combination of t1, t2 and t3 so that
the total equivalent
% residual stress < 10MPa and the moment is minimum

for i = 1:length(t1)
  for j = 1:length(t2)
      for k = 1:length(t3)
        T(2) = t1(i); T(6) = t2(j); T(7) = t3(k);% Update thickness of each design layer
```

```
% Calculating neutral axis
Eq = 0;
M = 0;
for p = 1:n
  Eq = Eq + E(p) * (h + sum(T(1:p)) - 1/2*T(p)) * T(p);
end
H = solve(Eq, h); % Calculated neutral axis
H = double(H); % Converting from sym to double for later calculation

epsilon = sum (S0 .* T) / sum (E_ .* T); % Total strain of the beam due to
residual stresses
S0_ = S0 - E_ * epsilon; % Residual stresses after release but before bending
S0_eq = sum(S0_ .* T) / sum(T); % Total equivalent residual stress in the beam

for p = 1:n
  M = M + S0_(p) * 1/2 * ( (H + sum(T(1:p)))^2 - (H + sum(T(1:p-1)))^2); %
Total moment generated by residual stress
end

% Tip deflection due to bending moment
E_I = 0;
for p = 1:n
  E_I = E_I + E_(p) * 1/3 * ( (H + sum(T(1:p)))^3 - (H + sum(T(1:p-1)))^3);
% Equivalent E*I
end
rho = E_I / M; % Radius of curvature of the beam
theta = L / rho; % Angle subtended by the arclength L
tip_height = rho*(1 - cos(theta));

if abs(S0_eq) <= 10e6 && abs(tip_height) <= 0.01*sum(T) % Look for designs
whose corresponding residual stress is below 10MPa and tip deflection smaller than 1%
total thickness
  design_t1(q) = t1(i); % Record candidate design
  design_t2(q) = t2(j); % Record candidate design
  design_t3(q) = t3(k); % Record candidate design
  design_S0(q) = S0_eq; % Record corresponding total equivalent residual
stress
  design_S0_(q,:) = S0_;  % Record residual stress after release but before
bending
  design_M(q) = M; % Record corresponding total moment generated by
residual stress
  design_tip(q) = abs(tip_height) / sum(T); % The ratio of the tip deflection to
the total thickness of the beam
  design_H(q) = H;
```

```
            q = q + 1;
        end
    end
  end
end


% Display the parameters of optimal design
[dm, I] = min(abs(design_M)); % Find the design that gives minimum moment
design_t1(I) % Display best t1
design_t2(I) % Display best t2
design_t3(I) % Display best t3
design_S0(I) % Display total equivalent residual stress
design_tip(I) % Display ratio of tip deflection to the total beam thickness
%design_S0_(I,:) % Display residual stress in each layer after release but before bending
%design_M(I)*W % Display moment corresponding to best design (note design_M and
M has no width in them)
```

Jump-Down Frequency of Nonlinear Energy Harvesters

```
clear all
close all
clc

fmin=0; fmax=1000; %Frequency Range
Pm=zeros(1,1+fmax-fmin);
QQ=logspace(0,2.5,350);

%Device Dimensions
w=2.646e-3;
l=7.559e-3;
t=2.2e-6;
Y=145e9;
S0=20e6;
rho=2330;
tp=400e-6;
wp=16e-3;
Lp=16e-3;

Qa=80;Qs=1000;Qe=1e6; %Damping Coefficients
Qm = 1 / (1 / Qa + 1 / Qs);

m=1/8*1.161e-3; %Proof Mass


kl=pi^2/2*t*w/l*S0+Y*pi^4/6*t^3*w/l^3; %Linear Stiffness (From Equ. 3.17)
kn=Y*pi^4/8*t*w/l^3; %Nonlinear Stiffness (From Equ. 3.17)

fneq = zeros(1,fmax-fmin+1);
A=4.9; %Excitation Amplitude

F = m * A;
x0 = F / kl
alpha = kn / kl * x0^2;
Q = 1 / (1 / Qa + 1 / Qs);
zeta = 1 / (2 * Q); % Damping ratio
omega_0 = sqrt(kl / m);
omega_d = 1 / sqrt(2) * sqrt(1 + sqrt(1 + 3 * alpha / 4 / zeta ^ 2));   % Electrically
unloaded jump down
omega_u = sqrt(1 + (3 / 2) ^ (4 / 3) * abs(alpha) ^ (1 / 3) );
f_u = omega_0 * omega_u / (2 * pi)
f_d = floor(omega_0 * omega_d / (2 * pi))
```

```
b_m = sqrt(kl * m) / Qm;
for i = 1:f_d
   omega(i) = (i * 2 * pi) / omega_0;
   zeta(i) = sqrt(3 * alpha / 4 / ( (2 * omega(i) ^ 2 - 1) ^ 2 - 1) );
   Q(i) = 1 / 2 / zeta(i);
   Qe(i) = Q(i) * Qm / ( Qm - Q(i) );
   b_e(i) = sqrt(kl * m) / Qe(i);
   b_ratio(i) = b_e(i) / b_m;
   Y(i) = sqrt(2 / 3 / alpha * (sqrt(1 + 3 * alpha / 4 / zeta(i) ^ 2) - 1) );
end

P = 1 / 2 * b_e .* (Y .^ 2) .* (2 * pi * (1:f_d)) .^2;

figure
plotyy(116:f_d, b_ratio(116:f_d),116:f_d,Y(116:f_d))
xlabel('Jump-Down Frequency (Hz)');ylabel('Ratio of maximum electrical damping to
mechanical damping')

figure
plot(zeta(116:f_d),116:f_d,'b')
xlabel('Total Damping Ratio');ylabel('Jump-Down Frequency (Hz)');

figure
plot(zeta(116:f_d),P(116:f_d),'b')
xlabel('Total Damping Ratio');ylabel('Maximum Extractable Power (\muW)');

figure
plot(116:f_d, P(116:f_d),'b')
xlabel('Jump-Down Frequency (Hz)');ylabel('Maximum Extractable Power (\muW)');

Q = 1 / (1 / Qa + 1 / Qs);
zeta = 1 / (2 * Q);
Qe = Qm;
b_e = sqrt(kl * m) / Qe;
b_ratio(i) = b_e(i) / b_m;

P = 1 / 2 * b_e .* (Y .^ 2) .* (2 * pi * (1:f_d)) .^2;

hold on
plot(116:f_d, P(116:f_d),'r')
xlabel('Excitation Frequency (Hz)');ylabel('Maximum Extractable Power (\muW)');
```